FUNDAMENTAL ION–SURFACE INTERACTIONS IN PLASMA THRUSTERS

Thesis by

Robert Kolasinski

In Partial Fulfillment of the Requirements

for the Degree of

Doctor of Philosophy

California Institute of Technology

Pasadena, California

2007

(Defended October 12, 2006)

Acknowledgements

During the past five years I have been at Caltech, I have always considered myself very fortunate in two respects. First, I have been able to work on projects that I found interesting and challenging. More importantly, however, I have also had the opportunity to work with and learn from many talented and creative people on a daily basis, and these interactions have made my graduate school career a rewarding experience.

First, I am grateful to Jay Polk, my research advisor in the Advanced Propulsion Group at JPL for all of his advice and mentorship. Jay's creativity and insight was of great benefit to my own work. I can only hope that I will be able to serve my future colleagues this well. Both Dan Goebel and Lee Johnson gave a great deal of their own time to me in helping me formulate many of the core ideas in my thesis. Their vast expertise and experience in electric propulsion was a tremendously valuable resource for me (and the rest of our group as well.) I am also thankful for Prof. Fred Culick for serving as my academic advisor at Caltech, and giving me the opportunity to pursue research projects with JPL. I would also like to acknowledge all of the assistance of my thesis committee members, David Goodwin, Paul Bellan, and Erik Antonssen.

A number of individuals were helpful with some of the more technical aspects of the work described in this thesis. In particular, Al Owens and Ray Swindlehurst provided me with a great deal of advice on the design and fabrication of the experimental hardware. Jim Kulleck provided the SEM imagery and the x-ray diffraction scans of the molybdenum coatings as well as helping with the polishing of the molybdenum cathode keepers used in the SLA work. Kenneth Oxorn (ANS Technologies) helped with the initial development of the SLA experiments, and performed the proton activations. I am grateful to Mark Anderson (JPL) for acquiring the AFM imagery and Elizabeth Miura (Caltech) for obtaining the Raman spectroscopy measurements of the graphite coatings. Jay Whitacre (JPL), Jeremey Hanna (UCSD), and Russ Doerner (UCSD) donated their time to deposit the thin films used during the sputtering yield measurements.

During my first three years at Caltech, my graduate work was supported though a National Science Foundation (NSF) fellowship. My later work was sponsored through the Nuclear Electric Xenon Ion System (NEXIS) and NASA Evolutionary Xenon Thruster (NEXT) programs. I am very appreciative to Dan Goebel, Ira Katz, and David Vaughan (all at JPL) for their help in securing funding during the completion of my degree.

I have been very fortunate to have made great friends since I have been at Caltech. For simplicity, I'll acknowledge those who contributed directly to the work in this report, in chronological order. Richie Wirz, a talented musician and fellow Caltech student, initially encouraged me to pursue research in advanced propulsion. Needless to say, my graduate career would have been much different and not nearly as rewarding without his advice and friendship. Dan Thunnissen, my roommate at Caltech for four years, was also my study partner for the qualifying exams. He was also a great friend, and shared with me a great deal of advice on paper writing and thesis preparation. John Ziemer (JPL), also one of my best friends, advised me on the use of UHV equipment throughout the design of the sputtering experiments. He, along with David Conroy and Lee Johnson (both from JPL) were invaluable in helping me get acquainted with the electric propulsion laboratory. In addition, my friendships with Matt Bradford and Adrian Downs (both JPL) were an integral part of my life outside of work.

I am grateful to my family in my hometown of Phillipsburg, NJ for all of their support throughout my life. This includes my brother, Michael, my grandmother, Dora, and especially my mother, Barbara, who initially fostered my interest in spaceflight and encouraged me to pursue a career in science from an early age.

Finally, I wish to thank my girlfriend, Moira for all of her love over the past few years. I'll always remember this as the time of my life when I met the love of my life.

Abstract

Ion thrusters offer the potential to enable many future interplanetary robotic missions presently under consideration by NASA. To realize the benefits offered by these low thrust devices, the sputtering mechanisms that are responsible for the degradation of thruster components over time must be well understood. Predictions of thruster life depend directly on the material removal rates from thruster electrodes such as the ion optics and hollow cathodes. To better understand the conditions encountered at these surfaces, this study includes an investigation of low energy sputtering at glancing incidence. Relevant ion–target combinations that were considered included Xe^+ incident on Mo, C, and Cu, as well as Ar^+ incident on W, C, and Cu.

To characterize the sputtering yield angular dependence experimentally, an ion beam was used to etch a coated quartz crystal microbalance. This required the development of techniques to accurately measure the incident low energy ion flux to the target and the use of surface diagnostics to investigate the properties of target materials. Measurements of C and Mo sputtering yields were obtained for Xe^+ incidence angles up to 80º from the surface normal and for energies ranging from 80 eV–1 keV. In addition, existing transport theory models were used to examine projectile scattering within the different target media. The models also indicate that the sputtering behavior as a function of angle of incidence is not a strong function of energy, a conclusion that is supported by the experimental results. The surface roughness of the targets was investigated using atomic force microscopy to obtain local incidence angle distributions.

A surface layer activation technique served as an alternate method of evaluating the sputtering rates of thruster components for situations where the ion bombardment conditions are not well known. In this study, a radioactive tracer was produced in the surfaces of a number of laboratory model ion thruster cathode assemblies by high energy proton bombardment. The cathodes were tested in a 30 cm diameter xenon ion thruster to provide insight into the relevant wear mechanisms at

different thruster operating points. Methods for combating cathode degradation are proposed based on the experimental results.

Table of Contents

List of Figures

List of Tables

Nomenclature

a	= reference count rate
a_I	= interatomic screening length
a_o	= Bohr radius (0.0529 nm)
a_{TF}	= Thomas-Fermi screening length
c_f	= QCM sensitivity function
E	= incident particle energy
h	= number of isotopes present in sample spectrum
h_E	= QCM electrode thickness
h_o	= QCM half-thickness
H_l	= Hermite polynomial of order l
I_{sp}	= specific impulse
J	= current
j	= current density
k	= Boltzmann's constant (8.6171×10^{-5} eV/K)
l	= grid separation gap
m	= spectrum scaling parameter
$\dot{m}_{cath}$	= cathode flow rate
$\dot{m}_{main}$	= main flow rate
$\dot{m}_{neut}$	= neutralizer flow rate
m_i	= ion mass
M_1	= atomic mass, incident particle
M_2	= atomic mass, recoil

$\vec{n}$ = local surface normal vector

$\vec{n}_b$ = vector aligned along direction of incident ion beam

N = target number density

P_l = Legendre polynomial of order l

q = elementary charge (1.6022×10^{-19} C)

R = QCM radius of curvature

R_p = projected range

S_n = nuclear stopping power

t = time

T = energy transferred to recoiling particle

T_e = electron temperature

T_w = cathode insert wall temperature

u = velocity

U_s = surface binding energy

V = voltage

W = weight factor array

Y = sputtering yield

y = sample count rate

z = total counts

Z_1 = atomic number, incident particle

Z_2 = atomic number, recoil

α = local angle of incidence

γ = reduced mass

ε_o = permittivity of free space (8.8542×10^{-12} $C^2/N\cdot m^2$)

η = total efficiency

θ = target angle of incidence with respect to normal

λ = wavelength

ν = frequency

ν_n = normalized spatial moment of order n

ρ = density

σ = cross section

τ = spectrum live time

τ_{meas} = measured thickness change

φ = potential

φ_e = effective work function

Φ = interatomic screening function

Acronyms

AES	Auger emission spectroscopy
AFM	atomic force microscope
BCA	binary collision approximation
C-C	carbon-carbon composite
CEX	charge exchange
CVD	chemical vapor deposition
DS1	Deep Space 1
ELT	Extended Life Test
EMT	engineering model thruster
FT	flight thruster
FWHM	full width at half maximum
HiPep	High Power Electric Thruster

HRL	Hughes Research Laboratories
JPL	Jet Propulsion Laboratory
LDT	Life Demonstration Test
LEED	low energy electron diffraction
MiXI	Miniature Xenon Ion Thruster
NASA	National Aeronautics and Space Administration
NEXIS	Nuclear Electric Xenon Ion System
NEXT	NASA Evolutionary Xenon Thruster
NSTAR	NASA Solar Electric Propulsion Technology Applications Readiness
QCM	quartz crystal microbalance
RGA	residual gas analyzer
SEM	scanning electron microscope
SEP	solar electric propulsion
SLA	surface layer activation
TRIM	Transport of Ions in Matter
UCSD	University of California, San Diego
UHV	ultra-high vacuum
XIPS	Xenon Ion Propulsion System

Chapter 1: Introduction and Motivation

Ion engines are characterized by their high specific impulse capability and superior overall efficiency when compared to their chemical thruster counterparts. This makes them uniquely suited for many specialized propulsion applications and an enabling technology for missions where high precision or large velocity change (ΔV) requirements preclude the use of more conventional propulsion devices. Because of their low thrust, long periods of operation (on the order of 2 to 10 years) are required to realize these benefits.

To generate thrust, most contemporary ion engine designs create a xenon plasma using a hollow cathode and a discharge chamber with a ring-cusp magnetic field. Xenon ions from the plasma are accelerated electrostatically through a set of grids. Both the cathode and grids are constantly exposed to energetic ions and are susceptible to sputtering, a process defined as the "removal of surface atoms due to energetic particle bombardment." [Berhisch, 1981] Over time, the material removed through sputtering causes significant modifications to the geometry of these components, resulting in changes that adversely affect performance and lead to thruster failure. Predicting the rate at which these changes occur is a key component of assuring adequate propellant throughput and service life capability.

Previously, long duration testing had been the primary method of evaluating the effects of sputtering in ion thrusters. However, as the demands for higher ΔV increase, this type of testing has become impractical for ensuring adequate lifetime over the entire engine throttle range. An alternative to this approach is to model the plasma conditions which are responsible for sputtering in ion thrusters and calculate corresponding material removal rates. The parameter which relates the erosion of solid surfaces to the incident particle flux is the *sputtering yield*, which is defined as the number of surface atoms removed per incident ion. Clearly, the accuracy of models which calculate the wear rates of thruster components depends directly on how well the sputtering yields of the

relevant materials are known. However, the lack of sputtering yield data for the materials and bombardment conditions that are relevant to ion thrusters has inhibited the development and implementation of such models.

In this thesis, the issues associated with these complex material removal processes are addressed through a combination of experiments and modeling. This chapter outlines the benefits of ion propulsion, which motivate this study, along with the basic principles of operation. A more detailed discussion of the role of sputtering in ion thrusters is also provided. A summary of objectives follows, and the chapter concludes with an overview of this thesis.

1.1 Ion Propulsion Overview

For many ambitious applications, the propulsion system requirements dictate the feasibility and overall difficulty of a given space mission [Frisbee, 1996]. Many low ΔV (hence, less propulsively demanding) applications such as inner planet landers and orbiters, robotic flybys of the outer planets, and low Earth orbit human missions, have already been successfully accomplished. Chemical thrusters using solid or liquid propellants were selected almost exclusively for these applications, with the reasoning that extensive development had already been devoted to their optimization. Given their heritage in flight applications, chemical rockets were generally considered "mature" technologies. These initial missions have paved the way for more ambitious applications (sample return, outer planet orbiters, multiple body rendezvous, and interstellar precursor) requiring capability for much higher ΔV [Polk, 2003]. For many of these missions, use of an electric propulsion system may have the practical benefit of significant savings in propellant mass (thereby increasing the deliverable payload) and trip time. More importantly, many new electric propulsion systems under development serve as *enabling* technologies, allowing for missions that would otherwise be impossible with more conventional chemical propulsion.

Ion engines are a subset of electric propulsion devices that generate thrust through the electrostatic acceleration of ionized propellant through a set of ion optics. The propellant exit

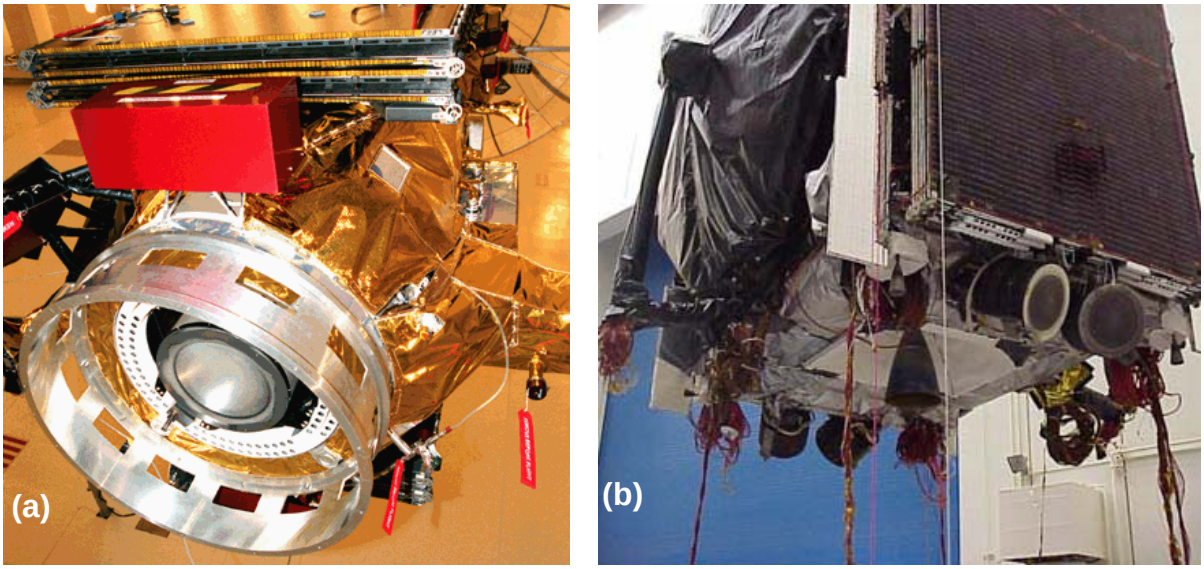

Figure 1.1: (a) The NSTAR thruster mounted on the Deep Space 1 spacecraft and (b) the Boeing XIPS-25 thrusters mounted on a 702 communications satellite.

velocity depends on the accelerating potential through which the ions pass, allowing high specific impulses to be achieved in this manner. The beam ion energy cost ε_B is an important metric for evaluating thruster performance; ε_B is defined as the discharge power devoted to creating each extracted beam ion:

$$\varepsilon_B = \frac{J_D V_D}{J_B} \qquad \textbf{1.1}$$

Note J_D and V_D are the discharge current and voltage, respectively, and J_B is the total beam current. Another important metric is the propellant utilization efficiency η_u, which is defined as the fraction of the propellant that is eventually accelerated to form the beam:

$$\eta_u = \frac{J_B}{\dot{m}_T}\frac{m_i}{q} \qquad \textbf{1.2}$$

In the above expression, m_i refers to ion mass, q is the electronic charge, and $\dot{m}_T$ is the total propellant mass flow rate. For modern thruster designs, ε_B = 180 eV/ion and η_u = 90%. The efficient use of propellant and power is an important aspect of realizing the advantages of operating at high I_{sp}. However, the need for an external power system represents a limitation on the thrust capability of these devices. With the power density of state of the art solar arrays at approximately 30 kg per 1

kWe, there is no presently developed space-based power system capable of competing with the energy liberated through the combustion of propellants in large chemical rockets. Despite thrust limitations, better overall efficiency and higher specific impulse compared to chemical thrusters has allowed ion thrusters to be advantageous for missions where increased trip time may be traded for increased payload mass or decreased spacecraft mass (so a smaller launch vehicle may be used.) In addition, the time of flight for many longer duration deep space missions may be shortened with electric propulsion.

The first electron bombardment ion thruster was constructed and tested at the NASA Lewis Research Center by H. Kaufman (1959). Subsequent decades of research and technology development focused on enhancing the performance of these devices, scaling discharge chamber sizes, and thruster endurance issues. A series of flight demonstration tests was flown during this time period, most notably including the Space Electric Rocket Tests (SERT) in 1964 [Cybulski, 1965] and 1970 [Kerslake, 1993], and the NASA Deep Space 1 (DS1) mission [Polk, 2001], launched in 1998. The 30 cm diameter thruster flown on DS1 operated in excess of 16000 hours during the probe's encounters with comet Borrelly and asteroid Braille and marked the first use of ion propulsion on an interplanetary mission. With the efforts of scientists primarily within the NASA Glenn Research Center (GRC), NASA Jet Propulsion Laboratory (JPL), and Hughes Research Labs (now L-3 Communications), ion propulsion has recently gained acceptance both in government and the commercial satellite industry within the United States. In addition, by assuming much of the risk associated with bringing the thruster technology to a level of maturity required for flight applications, the success of Deep Space 1 has opened up the use of these thrusters as primary propulsion for NASA asteroid and comet encounters. The next such mission will be Dawn, a cost-capped Discovery class mission slated for launch in 2007 [Brophy, 2004]. These thrusters have also been used for orbit raising (ARTEMIS, 2001) [Killinger, 2003], and station-keeping (Boeing 702 communications satellites, 1999) [Goebel, 2002]. Images of the Deep Space 1 and Boeing 25 cm Xenon Ion

Propulsion System (XIPS) thrusters are displayed mounted to their respective spacecraft in Figure 1.1.

In parallel with these efforts in the United States, significant ion thruster development has also occurred within the international community. Research of radio-frequency (RF) ionization of gases at Germany's University of Gieβen during the 1960's provided the initial motivation for ion thruster development in Europe [Bassner, 1994]. With an RF design, energy for ionization is created using a high frequency generator coil positioned around a quartz discharge chamber. This is in contrast to designs used in the United States which utilize a hollow cathode-anode configuration. During the 1970's, industrial development of 10 cm ion thrusters proceeded to bring the technological maturity of these devices to a level suitable for flight applications. The first flight test of an RF ion thruster by the European Space Agency (ESA) occurred as part of the EURECA mission, launched in 1992 aboard the space shuttle [Bassner, 1994]. The maximum thrust of the ion engines on this mission was 10 mN at an input power of 400 W, with an I_{sp} of 4700 s. The thrusters successfully operated for a total of 240 hours, and were later retrieved with the space shuttle during STS-57 in 1993.

The European Space Agency (ESA) mission ARTEMIS (Advanced Relay and TEchnology MISsion) represented Europe's second flight of ion thrusters in Earth orbit [Killinger, 2003]. Launched in 2001, this mission included a set of four ion thrusters for north-south station keeping. Designed to test advanced telecommunications technologies, another major objective of ARTEMIS was to demonstrate the viability of ion propulsion for this application. On this mission, two RF thruster designs were flown on the spacecraft, as well as two hollow cathode discharge thrusters [Killinger, 2000]. During ascent, the Ariane 5 launch vehicle upper stage failed and placed the ARTEMIS spacecraft in a useless, highly elliptical orbit. To salvage the mission, the ion thrusters were used in conjunction with the bi-propellant chemical thruster system to boost the spacecraft into geosynchronous orbit. The desired orbit was finally achieved in early 2003, approximately 600 days after the initial launch of the spacecraft [Killinger, 2003].

Table 1.1: Electron-bombardment ion thruster development history.

Thruster	Year	Prop.	I_{sp} (s)	Beam Dia. (cm)	Max. Thrust (mN)	V_D	ε_B (eV/ion)	Comments
Kaufman Thruster #1	1959	Hg	4500 to 5500	10	6	50	1200	First laboratory demonstration of a broad beam, electron bombardment ion thruster.
SERT I	1964	Hg	5000	10	28	46	700	First flight test of ion thruster, (suborbital.) Demonstrated neutralization of beam in space.
SERT II	1970	Hg	4200	15	28	37	220	Orbital flight demonstration. Equipped with two thrusters, both of which operated over 2000 hrs in space.
HRL[a] J-Series	1982	Hg	3000	28.5	128	32	220	Engineering model thruster developed for solar electric propulsion applications.
RITA-10	1992	Xe	4700	8.7	15	-	-	First launch of European ion thruster. Used RF discharge.
XIPS-13	1997	Xe	2565	13	63	25 to 28		Operational flight thruster.
NSTAR (DS1)	1998	Xe	3000	28.5	92	24.5	190	Launched as part of technology demonstration mission. Ground testing of flight spare thruster to over 30000 hrs. Planned use on Dawn mission in 2007.
XIPS-25	2002	Xe	3800	25	165	25 to 28	115	Operational flight thruster, in use aboard Boeing 702 communications satellites.
JAXA 35-cm	2002	Xe	3500	35	150	30	150	Developed by the Japan Aerospace Exploration Agency. Includes graphite cathode, grids.
MiXI	2003	Xe	1700 to 3200	3	3	25	400 to 500	Development model thruster constructed for precision formation flying applications.
NEXT[b]	2003	Xe	4110	35	230	23.7	130	
NEXIS	2005	Xe	7050	57	473	26.5	180	Designed for nuclear electric propulsion missions to the outer planets. Used advanced technologies such as carbon-carbon grids and reservoir cathodes.
HiPep[c]	2005	Xe	7640	-	428	28	220	Rectangular discharge chamber, pyrolytic graphite grids.

[a]Hughes Research Laboratories
[b]NASA's Evolutionary Xenon Ion Thruster
[c]High Power Electric Thruster

Recent work by the Japan Aerospace Exploration Agency (JAXA) has involved the development of 35 cm diameter ion thrusters [Hayakawa, 2002]. These thrusters generate a plasma discharge with a hollow cathode and use xenon propellant. With a maximum thrust of 150 mN at a power level of 3.4 kW, the performance of these thrusters is comparable to most state of the art designs currently in

use within the United States [Hayakawa, 2004]. Recently, the emphasis within Japan's research program has been on understanding and enhancing thruster life. In particular, graphite hollow cathodes and grids have been incorporated into thruster designs. Laboratories in Japan have also initiated several endurance testing programs aimed at identifying new thruster failure modes [Hayakawa, 2002; 2004].

An abbreviated summary of electron bombardment ion engines is given in Table 1.1. From this information, the recent technology development trend focusing on the scaling of the thruster discharge chamber size for different applications can be clearly seen. At the extremes of these efforts are the 3 cm Minature Xenon Ion (MiXI) thruster (designed for precision formation flying missions) [Wirz, 2004] and the 65 cm Nuclear Electric Xenon Ion System (NEXIS) thruster (for high power nuclear electric propulsion.) [Polk, 2003] Efforts to improve thruster service life represent another important long term development trend. Newer thruster designs have emphasized the use of sputter resistant materials, such as carbon composites. Also visible from Table 1.1 is the long term trend of decreasing the voltages of components that are exposed to the discharge plasma, a technique that has been used to decrease wear of thruster components. Note that the data in Table 1.1 indicate typical values of each design near its maximum throttle level.

1.2 Principles of Operation

As previously mentioned, ion engines ionize propellant and generate thrust through electrostatic acceleration. To prevent a negative charge from building up on the spacecraft, the thruster must also neutralize the beam. The NSTAR ion thruster configuration is shown in Figure 1.2 as an example of modern ion thrusters. The major components of the thruster include two hollow cathodes, a discharge chamber, and a set of grids (often referred to as the *ion optics*.) The discharge chamber forms the body of the thruster and consists of both a conical and cylindrical segment. Propellant gas is admitted to the chamber interior through the hollow cathode and a ring-shaped tube near the grids. In modern designs, xenon is used as a propellant, although in the past both mercury and cesium have been

employed. While Hg does offer some minor performance advantages over Xe, these are easily negated by the additional equipment mass needed to vaporize the propellant and the additional safety concerns associated with ground testing.

The hollow cathode serves as the electron source and is composed of a thoriated tungsten orifice plate electron beam welded to a molybdenum-rhenium tube. The sizes of the cathode and the orifice geometries generally depend on a number of factors, including the discharge current requirements of the thruster. As an example, the 0.635 cm (0.25 in) diameter hollow cathode used in 30 cm diameter ion thrusters has an orifice diameter of 1 mm and is capable of delivering a discharge current of approximately 14 A [Polk, 1999]. A porous tungsten tube impregnated with barium calcium aluminate (known as the *insert*) serves as the emitter material [Polk, 2004]. The work function of the insert is lowered by the presence of Ba and BaO on the surface, allowing emission to occur at temperatures of 1200 °C or less. An external heater is initially required to raise the insert up to its emission temperature until a plasma discharge is ignited. Once a discharge has been established, there is generally sufficient plasma bombardment on the interior of the cathode insert for self-heating. The walls of the discharge chamber are electrically isolated from the cathode and are biased to a higher potential of about 25 V. The electrons emitted by the cathode attain energies of 12-20 eV. During the electrons travel from the cathode to the anode potential surfaces, collisions with neutral propellant atoms occur, thereby stripping the atoms of an electron. To increase the probability of ionization, magnet rings are installed at different positions along the outside of the discharge chamber to increase the electron path length. A "ring-cusp" magnetic circuit is employed, and samarium-cobalt (Co_2Sm_{17}) magnet rings are located around the hollow cathode, at the intersection of the conical and cylindrical portions of the discharge chamber, and at the upstream end of the thruster near the grids. Additional magnet rings have been included on larger diameter thrusters; recent designs for 40 cm and 65 cm diameter thrusters have used four and six magnet rings, respectively. [Patterson, 2002; Polk, 2003]

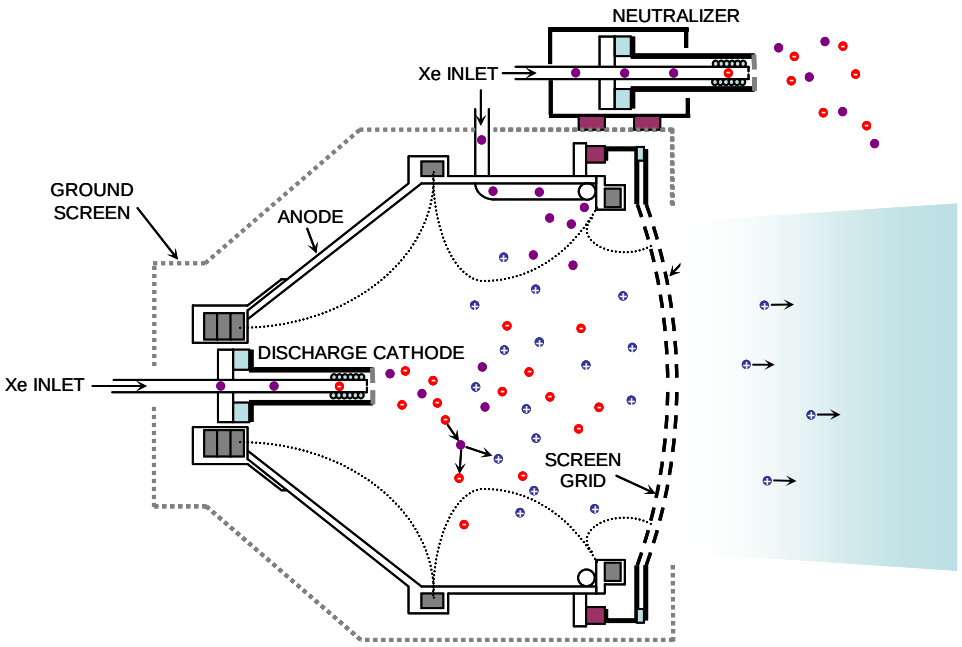

Figure 1.2: Schematic of a typical ion thruster configuration.

The ion thruster electrical schematic shown in Figure 1.3 displays the power supplies needed to ionize the propellant and extract a beam. The screen supply raises the thruster body along with the discharge plasma within it to a high voltage with respect to spacecraft ground (1100 V for a typical 30 cm thruster.) Ions within the discharge chamber drift toward the screen grid apertures and are accelerated out of the thruster by the force imparted by moving through this voltage difference. This is the mechanism by which thrust is generated. Because the entire thruster has been biased to a high positive voltage, a negatively biased accelerator grid is positioned just downstream of the screen grid to prevent electrons from backstreaming into the discharge chamber.

Table 1.2 is provided to give the reader a feel for the magnitudes of the controllable voltage and current parameters and the mass flow rates for the maximum throttle level of several modern ion thruster designs. It should be noted that the beam current is not directly controlled by the screen power supply, but indirectly through adjustments in the discharge current.

Table 1.2: Ion thruster operating parameters.

	NSTAR[a,b]	NEXT[a]	NEXIS[b]
Beam Diameter (cm)	28.5	35	57
Thrust, T (mN)	92	230	473
Input Power (kWe)	2.3	6.9	23.1
Specific Impulse I_{sp} (sec)	3100	4110	7590
Beam Current, J_b (A)	1.76	3.52	4.00
Beam Voltage, V_b (V)	1100	1800	5528
Accelerator Grid Current, J_a (mA)	5.0	12.5	38.0
Accelerator Grid Voltage, V_a (V)	-180	-250	-504
Discharge Current, J_d (A)	13.3	19.5	25.9
Discharge Voltage, V_d (V)	25.2	23.7	26.3
Neutralizer Keeper Current, J_{nk} (A)	2	3	3
Neutralizer Keeper Voltage, V_{nk} (V)	14.5	10.8	14.5
Cathode Mass Flow Rate, $\dot{m}_{cath}$ (sccm)	3.7	4.87	5.8
Main Mass Flow Rate, $\dot{m}_{main}$ (sccm)	23.4	49.6	54.1
Neutralizer Mass Flow Rate, $\dot{m}_{neut}$ (sccm)	3.60	5.16	4.6

[a]Developed by NASA Glenn Research Center
[b]Developed by NASA Jet Propulsion Laboratory

To prevent the spacecraft from accumulating a large negative charge, an additional hollow cathode is positioned outside the thruster to emit electrons. This cathode is aptly named the *neutralizer*. A keeper electrode surrounding the cathode maintains a discharge. The potential of the neutralizer cathode typically floats lower than the space plasma potential to allow electrons to be drawn into the ion beam for the purpose of neutralization.

1.3 Damage Accumulation Caused by Sputtering

Ion thrusters provide much lower thrust compared to chemical thrusters, given that the power generated by the combustion of propellants cannot be matched by any practical electrical power technology presently available. Because of this, ion thrusters must perform reliably over long periods of time. For lower ΔV solar electric propulsion (SEP) missions, the time of flight may be on the order of 3 to 5 years. For higher powered missions, over 10 years of continuous operation may be needed.

A common issue associated with plasma devices is the effect of sputtering, where energetic particles remove atoms from solid surfaces. The mechanism by which materials are eroded is by kinetic energy transfer from the incident particle to the target medium. If an atom near the surface

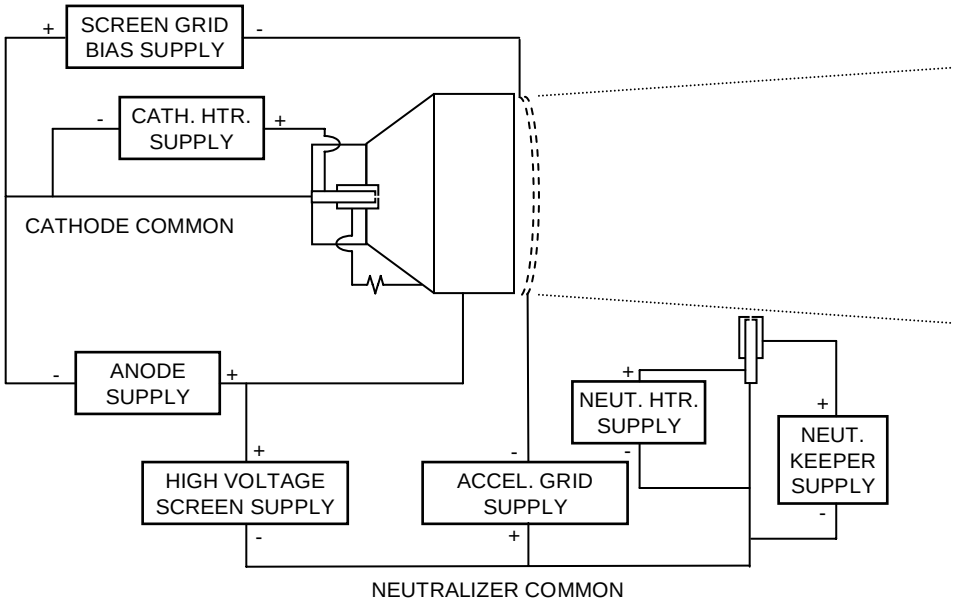

Figure 1.3: Ion thruster electrical diagram.

attains an energy greater than that binding it to its nearest neighbors, it will be ejected. The accelerator grid is especially susceptible to damage in this manner from bombardment by charge exchange ions created in between the grids. In addition, the surfaces of the discharge cathode and screen grid are constantly exposed to the discharge plasma and are therefore subjected to wear processes. In each of these cases, sputtering changes the geometry of these components to the extent that they are no longer able to fulfill their intended function, resulting in thruster failure. Understanding these processes and being able to predict wear rates are necessary for assessing propellant throughput capability at different throttle levels, and is essential information to systems engineers from the earliest stages of mission design.

Assuring that sufficient ion thruster life can be achieved is a difficult process. In the past, the technique of choice for accomplishing this objective had been long duration testing. Although there are many benefits to this, it is an unrealistic method for establishing useful thruster lifetimes when the required burn times are in excess of 3 to 5 years. Reliance on life testing alone also inhibits new

thruster development, as it is impractical to optimize designs based on the construction and testing of prototypes. This indicates the need for sophisticated design tools and models that are capable of optimizing the ion engine for a combination of both performance and service life. This requires accurate knowledge of both the ion bombardment conditions at the different thruster surfaces as well as the sputtering yields of electrode materials under these conditions.

Despite the great deal of research that has been conducted in the field of sputtering [Smentkowski, 2000], significant gaps in experimental data exist for conditions that are of interest to ion propulsion applications. Most studies have previously focused on yield measurements at normal incidence; the dependence of yield on angle of incidence has been investigated far less extensively [Berhisch, 1981]. Most of the data from these studies have been obtained for high energy (10-100 keV) light ions. However, for the wear conditions of interest to ion propulsion, low energy (<1 keV) heavy ion bombardment at varying angles of incidence is required. Existing theoretical and computational models applied to this sputtering regime do not provide the level of accuracy required for life assessment.

1.4 Thesis Objective

Determining the erosion rates of thruster components for the purposes of life assessment and validation requires an understanding of both the plasma bombardment conditions at the relevant surfaces as well as the fundamental physics of sputtering. This thesis addresses the sputtering physics portion of this problem for both ion thruster grid and cathode wear. An enhanced understanding of low energy, heavy ion sputtering at varying angles of incidence is a major result from this work, as well as high accuracy sputtering yield measurements for these conditions. The influence of ion-target atom mass ratio on the dimensions of a typical collision cascade with in a solid during ion bombardment is also investigated in detail. For cases where the plasma bombardment conditions are not well defined, diagnostics to measure the wear rates directly are required, and were developed as part of this study.

While these objectives are tailored to addressing problems specific to electric propulsion, it is expected that the results obtained in this study will have much broader applications. Ion beam etching of surfaces has become an important fabrication technique for a wide range of industrial processes, and the ability to create surface structures smaller than 1 μm in width has been applied by the electronics industry to the fabrication of integrated circuits [Lee, 1979] and hard disk drive heads [Hsiao, 1999]. Sputtering has also become ubiquitous throughout surface science, and is used for ion depth profiling and surface cleaning [Oura, 2003]. In addition, sputtering has been found to have a negative impact as a contamination mechanism in fusion plasmas [Behrisch, 1981].

1.5 Research Approach and Thesis Overview

This thesis is subdivided into three parts, beginning with a review of ion thruster sputtering processes. Chapter 2 begins with a detailed discussion of the physics of sputtering. The collision processes by which energy is transferred from incident particles to a solid medium are discussed. Also, the plasma bombardment conditions that are of interest to grid and cathode sputtering are established based on a review of prior thruster experimental and modeling work, including the results of long duration wear tests. Chapter 3 provides a literature review of existing sputtering models which are relevant to ion thruster sputtering. A review of previously published sputtering yield measurements at glancing incidence is provided at the end of this chapter, along with a comparison between the predictions of the models and the prior experimental data.

The second portion of this thesis is an experimental investigation which addresses the basic sputtering physics responsible for ion thruster grid wear. Sputtering yields for metallic targets at varying angles of incidence are measured using a sensitive experimental technique employing a quartz crystal microbalance (QCM). Details regarding the design and validation of the experimental setup, which represents the first application of the QCM technique to this type of measurement, may be found in Chapter 4. Also included in this chapter is a discussion of a unique method of determining the neutral atom content of the beam using electrostatic filtering. Sputtering yields at

normal incidence are presented as a validation of the experimental method, along with the first measurements of grazing incidence molybdenum measurements. The QCM technique was then modified to allow for carbon sputtering yield measurements, as discussed in Chapter 5. Because the change in mass of the target is measured *in-situ*, implantation of Xe in the C surface is observed. Experimental measurements of C sputtering yields at grazing incidence are presented, the first such results for this material under Xe bombardment. The experimental results are modeled in Chapter 6 using existing transport theory approaches. A detailed characterization of the surface topography is undertaken in this chapter as well to characterize its influence on the yield measurements.

The final part of the thesis includes an experimental examination of cathode sputtering in ion thrusters. In the cathode region of the discharge chamber, the plasma bombardment conditions are not well known, making the sputtering data obtained previously of limited use for this region. In this case, a technique known as surface layer activation (SLA) is used to measure wear rates directly by using components activated with a high energy ion beam to create a radioactive tracer in the near surface region. This technique is discussed in detail in Chapter 7. The dependence of cathode wear rate is determined as a function of throttle level. Techniques to combat erosion, such as biasing the cathode keeper electrode, are also discussed.

This thesis concludes with a summary of major contributions, which appears in Chapter 8. Directions for future work are identified, which included a proposed list of other ion-target combinations which may be examined. The chapter includes summary of how the sputtering data obtained in this thesis is to be implemented a computational model used to predict ion thruster grid wear. The chapter concludes with a discussion of the potential impacts of the improved sputtering data on thruster life calculations.

Chapter 2: Relevant Experimental Data and Models for Ion Thruster Sputtering

Sputtering processes are responsible for the accumulation of damage to the ion thruster grids and cathodes over time. Since both the cathode and grid assemblies are critical for long duration operation, thruster life is directly related to the amount of damage sustained by these components through sputtering. This chapter begins with an overview of the physics of sputtering by energetic particle bombardment to provide the framework needed to understand thruster wear processes. The mechanisms for energy transfer between incident ions and the target medium are discussed as well as the ejection process for surface atoms.

Specific wear mechanisms associated with the ion thruster grids and cathodes are addressed in the second portion of this chapter, along with an analysis of previous endurance testing. These tests establish the wear problems that will be addressed by the experimental investigation discussed in the rest of this thesis and are used to provide insight into the fundamental physics of ion thruster sputtering. An analysis of recent experimental and computation studies on the plasma conditions near the grids and discharge cathode is also provided in order to establish the bombardment conditions that are of interest. The chapter concludes with a discussion of the material properties that influence sputtering yields.

2.1 Overview of Sputtering Physics

As mentioned in the previous chapter, sputtering is generally defined as the removal of atoms from a solid surface by bombardment with energetic particles [Smentkowski, 2000]. Sputtering was first recognized in plasma discharges by Grove (1852; 1853) and Gassiot (1858) as the process responsible for material loss from cathode surfaces.

It is useful to define a *sputtering yield*, which is the number of target atoms removed per incident ion. Expressed in the form of an equation, the sputtering yield is [Smentkowski, 2000]:

$$Y = \frac{N_t}{N_i} \qquad \textbf{2.1}$$

Note that in the above expression, N_t is the number of target atoms removed and N_i is the number of incident ions. The earliest attempts at measuring sputtering yields were performed Kingdon and Langmuir (1923) using plasma discharges. The yield, as defined by Equation 2.1, is particularly useful for calculating the erosion rates of materials under different ion bombardment conditions because it allows the material removed by sputtering to be related directly to the incident ion flux. However, it is important to recognize that the sputtering yield, Y, summarizes a great deal of information into a single parameter. In fact, Y depends on the incident ion mass and energy, target medium atomic mass, surface roughness, angle of incidence, and numerous other parameters. Because of this, a challenge of analyzing the sputtering behavior of different materials experimentally is isolating the key processes which are of interest [Anderson and Bay, 1981].

In sputtering processes, surface atoms may be removed through a number of fundamentally different mechanisms. The first of these processes, known as *physical sputtering*, is the transfer of kinetic energy from the incident particle to the atoms of the target medium through collisions [Berhisch, 1981]. The atoms which receive kinetic energy from the incident particle are referred to as *recoils*. In such a case, the incident particle impacts the surface and undergoes a number of collision steps, losing energy in the process. If a sufficient amount of energy is transferred to atoms near the surface, these atoms may attain enough kinetic energy to overcome the surface binding energy of the solid, U_s. The surface binding energy is generally treated as the potential barrier which must be overcome for a surface atom to break its bonds with all of its nearest neighbor atoms.

Physical sputtering processes are the dominant mechanism of surface atom ejection when the incident ions do not chemically react with the target medium. This is generally the case for most

electric propulsion applications, where inert gases are used in plasma discharges. However, for cases where the incident particles chemically react with the target surface, *chemical sputtering* may have a much more significant impact on target erosion [Berhisch, 1981]. In this instance, incident ions which become implanted within the target medium form chemical bonds with the surrounding atoms. If the concentration of imbedded ions is sufficiently large, the binding energy of the surface may be significantly altered.

2.2 Ion Thruster Endurance Test Overview

Endurance testing has played an important role in ion thruster technology development. In many cases, this was the only means of validating the propellant throughput capability of a particular engine design. For obvious reasons, such information is vital from a systems engineering standpoint at the earliest design stages for a given spacecraft. The need for adequate life and long duration testing was recognized in the earliest ion thruster work [Kaufman, 1961]. During the 1970's, Hughes Research Laboratories devoted a great deal of effort to testing its J-series 30 cm diameter mercury thruster designs [Maloy, 1981]. A great deal of the present understanding of cathode sputtering is derived from a series of endurance tests as part of the NASA Solar Electric Propulsion Technology Applications Readiness (NSTAR) program. Spanning most of the 1990's, this program developed the 30 cm xenon ion thruster used on the DS1 spacecraft and included four long duration tests on engineering model (EMT) and flight (FT) engines. The testing chronology is presented in Table 2.1.

The National Aerospace Laboratory of Japan (now part of the Japanese Aerospace Exploration Agency) has also recently conducted extensive wear tests of 35-cm diameter xenon ion thrusters [Hayakawa, 2001]. During a 5000 hour endurance test, significant wear of the tantalum discharge cathode was observed, and subsequent design iterations used graphite components [Hayakawa, 2004]. Back-sputtered metallic material from the chamber interior also coated many of the isolators during this test, causing electrical shorts between thruster components. The metallic coatings also produced

Table 2.1: NSTAR life test history.

Year	Location	Hours	Test Article	Erosion
1995	NASA Glenn Research Center	2150	EMT 1	Test operated at maximum throttle setting. Severe cathode wear observed. Significant flakes deposited on discharge chamber interior, severe screen grid erosion [Patterson, 1995].
1995	NASA JPL	1024	EMT 1b	Test operated at maximum throttle setting. Keeper electrode introduced, change reduced cathode wear significantly. Discharge flake retention mesh included. Minimal observed screen wear [Polk, 1996].
1996[a]	NASA JPL	8192	EMT 2	Test operated at maximum throttle setting. Posttest analysis showed keeper orifice plate reduced in thickness by 33%. Deposits observed on upstream surface [Polk 1999].
1998 – 2003[b]	NASA JPL	30352	FT 2	First 4937 hrs of test operated at maximum throttle setting. Higher than expected keeper wear observed after thruster throttled down to an intermediate power level. Keeper completely destroyed by end of test, significant cathode chamfering found during posttest analysis. After 30000 hrs of operation, complete wear-through between accelerator grid apertures observed [Sengupta, 2003].

[a]Also referred to as the Life Demonstration Test (LDT)
[b]Also referred to as the Extended Life Test (ELT)

flakes which became lodged in the grid apertures, resulting in aberrant erosion in these regions. Despite these difficulties however, it was estimated that all components of the thruster assembly would withstand over 4100 hours of operation [Hayakawa, 2001].

In support of the European Space Agency's (ESA) ARTEMIS mission, a successful 15000 hour life test of a 10 cm diameter radiofrequency thruster system (RITA) was conducted under the leadership of Astrium [Killinger, 2001]. The purpose of this endurance test was to validate the ion propulsion system for north-south station keeping functions. The RF power required to maintain a constant beam current was observed to increase as a result of erosion to the grid apertures [Killinger, 2000]. During this test, a total impulse of over 700,000 N·s was attained, with a projected thruster life at its maximum throttle level well in excess of the 15000 hour test duration [Killinger, 2001].

Long duration testing is valuable from a technology development standpoint because it allows for the identification of thruster failure modes and provides guidance for future design improvements. Such was the case during the NSTAR program, when an initial 2000 hr wear test of a 30 cm

engineering model thruster revealed higher than expected wear of the cathode and screen grid [Patterson, 1995]. A number of engineering solutions incorporated into the thruster design mitigated these problems, as verified in later testing [Polk, 1996].

A literature review by Brophy (1996) examined over 60 thruster wear tests conducted between 1962 and 1995, in which 18 different failure modes were identified. This review summarizes findings from tests conducted both within the United States and abroad. An important observation from Brophy's review is that the sputtering phenomena of interest occur very slowly, and it is therefore impractical to accumulate wear data for the entire throttle range of a given thruster or to iterate over different design options efficiently. For missions requiring relatively large ΔVs, thruster operating times in excess of 80000 hours may prohibit testing to the full lifetime of the thruster prior to launch. For these purposes, being able to accurately predict material removal rates from thruster electrodes using computational modeling or shorter duration wear tests is essential.

2.3 Sputtering of the Ion Extraction Grids by CEX Ions

The process by which ions are extracted though the grids was understood well before the construction of the first ion thruster in 1959, based on prior theoretical and experimental work by Child (1911) and Langmuir (1913). In these studies, the maximum current density that can be extracted through a set of parallel planes is given by

$$j = \frac{4\varepsilon_o}{9}\left(\frac{2q}{m_i}\right)^{1/2}\frac{\phi^{3/2}}{l^2} \qquad \textbf{2.2}$$

This is the well-known Child-Langmuir law, which gives the space charge limited current density j for planes separated by a distance l, with a potential difference φ. The ion charge and mass are given by q and m_i, respectively. Based on this equation, it is clear that the maximum thrust density for a given design depends on electrode geometry and potential.

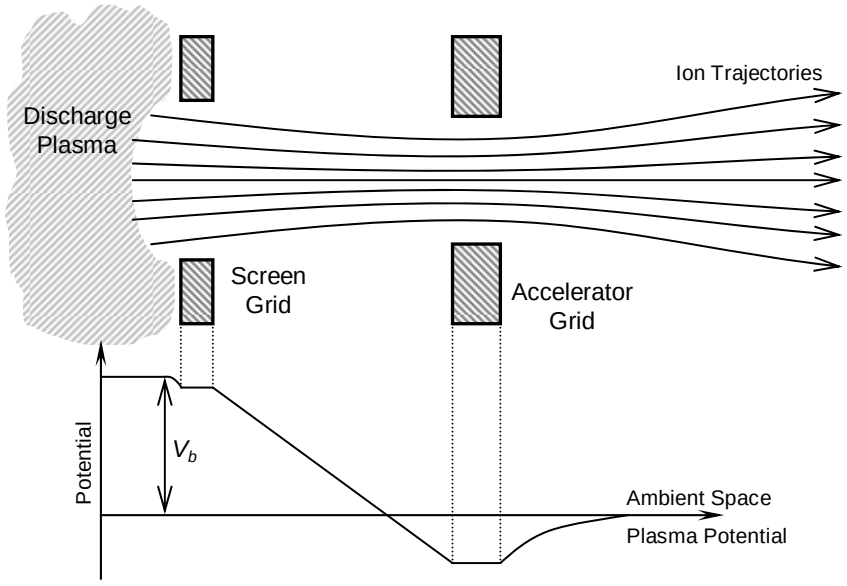

Figure 2.1: Cross section of a single ion thruster grid beamlet.

A cut-away view of a single ion thruster beamlet is shown in Figure 2.1, along with the potential along the grid aperture centerline. The ions within the discharge plasma are at a potential V_b (known as the *net beam voltage*) above the space plasma potential. With the screen grid tied electrically to the cathode, the potential difference between the plasma and screen is equal to the discharge voltage V_d. The ion acceleration is not strictly a 1-D process, and the ion trajectories are influenced greatly by the shape of the plasma sheath that forms at the edges of the screen apertures. These ions enter the sheath with the Bohm velocity, which depends on electron temperature, T_e [Chen, 1965]:

$$u_{bohm} = \sqrt{\frac{qT_e}{m_i}} \qquad \textbf{2.3}$$

As ions move through the screen grid apertures, they experience a large potential drop through which they are accelerated to their exit velocity. Electrons are reflected away from the screen grid, and the electron density in the inter-grid region is usually negligible for most practical calculations [Anderson, 2004]. For well-designed optics operating with the intended potentials and plasma

densities, the sheath takes on a concave shape, focusing the ions through the apertures in a well-collimated beamlet. This configuration is depicted in Figure 2.1. Excessive plasma density for a given total accelerating voltage may cause a convex sheath, resulting in divergent beamlets and poor focusing. In particularly severe cases, direct impingement of ions on the accelerator grid and the formation of rouge holes may result.

The accelerator grid does not actually play a role in the ion acceleration process. Its primary function is to prevent electrons from backstreaming into the discharge chamber, which is biased positive with respect to the ambient space plasma potential. Downstream of the accelerator grid, the individual beamlets combine to form a single broad beam. Electrons from the neutralizer eventually enter the plume and neutralize the beam farther downstream of the thruster.

Un-ionized propellant atoms, unaffected by the potential gradients within the thruster, also drift through the ion optics apertures through the process of free molecular flow. The loss of neutrals from the discharge chamber in this manner adversely affects thruster performance, and small hole accelerator grid (SHAG) optics have been used to mitigate this effect. Such an approach is used in all modern ion thruster designs to improve propellant utilization efficiency. The presence of neutrals in the inter-grid region also introduces the possibility of collisions with high energy ions. Such collisions involve strong interactions between the electron shells of the two particles and commonly result in the transfer of an electron from the neutral atom to the ion. This is referred to as a *charge exchange* (CEX) *collision*, shown schematically in Figure 2.2. This type of CEX collision results in the creation of a fast-moving neutral atom and a much less energetic ion.

The ions created from CEX collisions may at first seem fairly benign because of their low energy. However, these ions are not subjected to the full acceleration process because they are created at an intermediate point between the grids. Because of this, they may not be focused properly and can eventually collide with the accelerator grid (or other spacecraft components), resulting in sputtering damage. Two damage accumulation failure modes specifically associated with this process include:

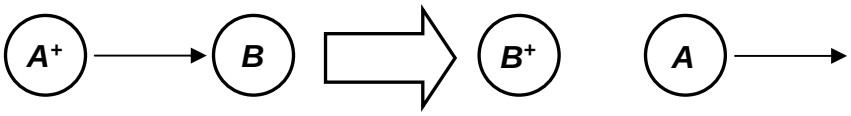

Figure 2.2: Charge exchange collision schematic, as in [Jahn, 1969].

(a) accelerator grid structural failure from the complete wear through between the apertures and (b) electron backstreaming from excessive widening of the accel. grid apertures. These are significant because the required accelerator grid negative bias in order to prevent neutralizer electrons from backstreaming into the discharge chamber increases as the apertures grow in size. When the hole diameter enlarges to the point that the voltage required to prevent backstreaming exceeds the power supply capability of the PPU, the thruster will no longer be able to maintain this given operating point. The presence of wear-through pits also contributes to this failure mechanism. Sputtering processes also indirectly introduce an additional failure mode by producing flakes, which become lodged between the grids. Such flakes may reduce the voltage standoff capability of the optics, eventually creating a hard short between them. The process of clearing these flakes is discussed in detail in Section 2.3.3.

2.3.1 Observations from Life Tests

Sputtering from CEX ions has been observed during numerous long duration ground-based ion engine tests. Figure 2.3a depicts the downstream surface of the accelerator grid from a 30 cm ion thruster after an 8200 hr endurance test [Polk, 1999]. This grid was manufactured from molybdenum, with an initial hole diameter of 1.14 mm. The apertures enlarged to 1.4 mm after the completion of the test. Note that the grid apertures are arranged in a hexagonal pattern and the regions of wear occur on the grid webbing between the holes. At these locations, a *groove* has been etched between each of the holes and regions of maximum wear are manifested as *pits* occurring at the vertices of the

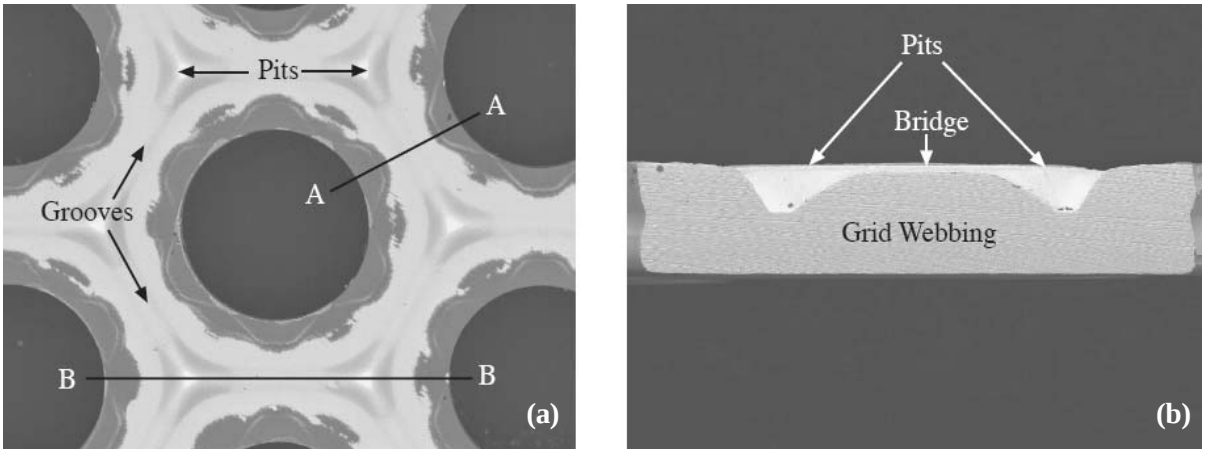

Figure 2.3: (a) Downstream surface of an accelerator grid after 8200 hours of operation and (b) cross section B-B showing pits and grooves erosion profile [Polk, 1999].

hexagonal pattern. This type of erosion is seen on most ion thruster designs after long periods of operation and is typically referred to as a *pits and grooves* wear pattern. A cross section along one of the grooves is shown in Figure 2.3b, displaying the geometry described above in greater detail. With continued operation, the sputtering damage will continue until the pits have worn completely through the grid webbing. A particularly severe case of this is shown in Figure 2.4. Note that the darkened regions on both of these images correspond to areas where the carbon material from the inside of the test chamber has been deposited on the grid surface. The sputtering yield of carbon is lower than that of the molybdenum, and its presence here suggests the ion flux to these regions is not sufficient to maintain a dynamically clean surface. Care must be taken when interpreting endurance test results as the carbon deposits will protect the grid webbing, leading to an underestimation of projected wear.

A set of optics was tested to failure by Brophy (1993) under conditions that were known to accelerate the erosion process. To artificially increase the rate of CEX ion production, the test was conducted with a higher than nominal facility background pressure. An increased negative bias on the accelerator grid also served to enhance the erosion rate. The grid design was similar to that used during the 8200 hour endurance test described above and on the DS1 ion thruster. Under the enhanced erosion conditions, the optics were unable to withstand the desired operating voltages after

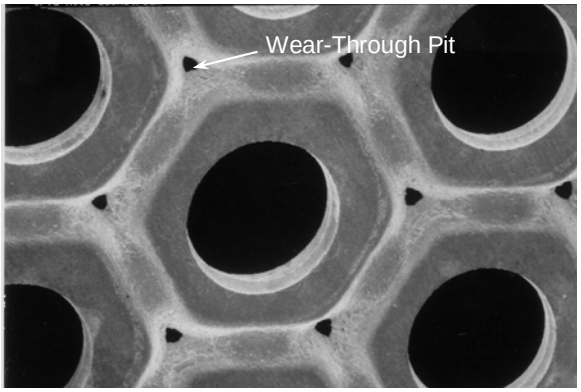

Figure 2.4: Accelerator grid downstream surface showing severe sputter damage, with wear-through pits between the holes [Brophy, 1993].

only 633 hours of operation. The cause of failure was flaking between the grids, resulting from severe erosion near the periphery. Severe pits and grooves erosion had also nearly caused structural failure near the center of the accelerator grid.

2.3.2 Modeling Approaches

Recent efforts have been successful in modeling charge exchange ion production and predicting sputtering rates of grid components [Arakawa, 1996; Brophy, 2002]. State of the art computational models provide significant insight into the factors that affect the locations where CEX ions are generated as well as their energies. Because of the cylindrical geometry, many of these features can be accurately calculated using a 2-D domain, as in a recent JPL study using a computational grid model known as CEX2D [Brophy, 2002]. This code is frequently used as a design tool for ion optics as well. The prediction of complex phenomena such as the pits and grooves erosion pattern requires a more sophisticated 3-D treatment. Such an approach is described by Anderson (2004).

The CEX2D code has been validated extensively against experimental data and is emphasized in this discussion. However, a number of other computational codes have been developed using similar techniques. Inputs for the code include the grid geometry and potentials, as well as the upstream plasma density. The general approach for modeling ion optics involves first solving for the stationary

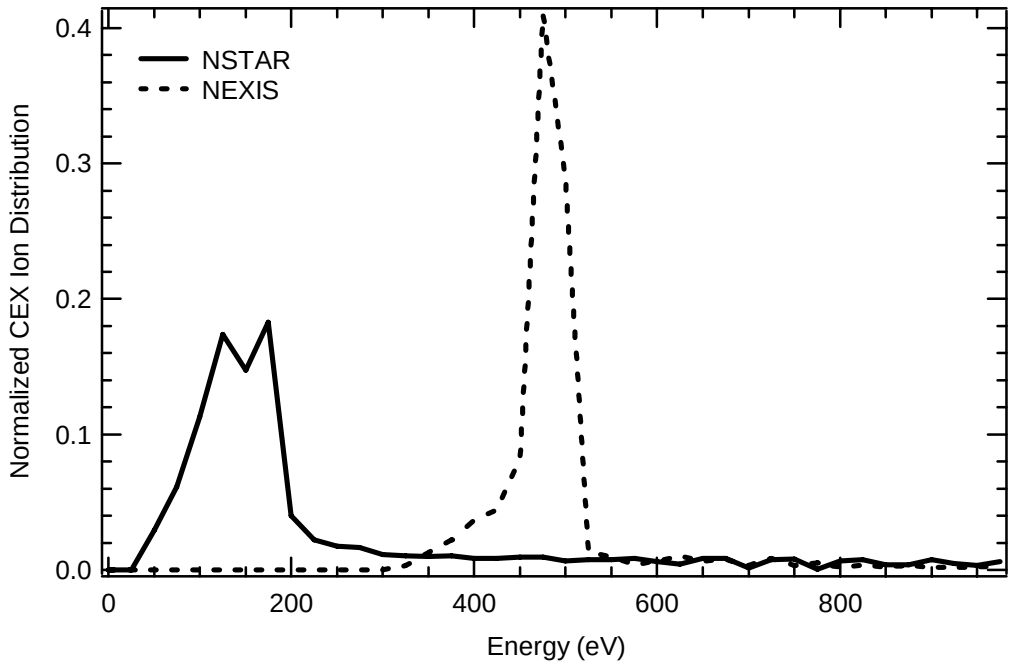

Figure 2.5: CEX ion energy distribution for ions striking accelerator grid hole walls in NSTAR and NEXIS configuration thrusters.

electric field using Poisson's equation. Ions enter the plasma sheath attached to the screen apertures with the Bohm velocity, and their trajectories are calculated based on the previously determined potential distribution. The upstream and downstream electron populations are assumed to follow Boltzmann distributions (at different reference potentials). Charge exchange collisions are simulated using a Monte Carlo approach. The locations where CEX ions are generated are tracked, along with their trajectories. For cases where an ion strikes the accelerator grid, the impact angle and energy are recorded [Brophy, 2002]. A sufficient number of events can be accumulated to obtain distributions of ions over ranges of these parameters.

To identify the bombardment conditions of interest for the work described in this thesis, the author used the CEX2D code to calculate the ion bombardment conditions for two relevant ion thruster configurations. These results are shown in Figure 2.5, which displays a histogram of CEX ion energy for those ions that hit the accelerator grid aperture walls in the NSTAR thruster design.

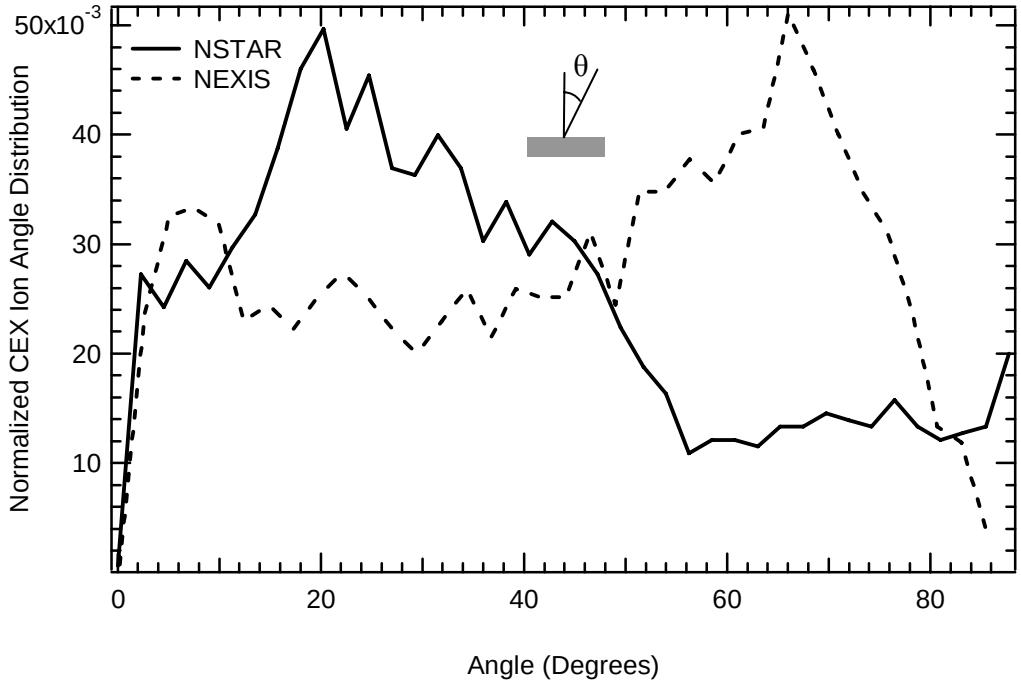

Figure 2.6: CEX ion impact angle distribution for the NSTAR and NEXIS configuration ion thrusters, calculated for this study using the CEX2D code.

The operating condition for this particular case was the 2.3 kW input power setting, corresponding to the maximum throttle point for this engine. Detailed operating parameters for the NSTAR engines are discussed in a prior publication [Anderson, 2001]. It is interesting to note that a majority of these ions have energies of approximately 150-200 eV. However, the higher energy ions in the range of 400 eV to 1 keV could also be responsible for much of the erosion, given that the sputtering yield at these energies is up to 2 orders of magnitude higher. The 65 cm diameter Nuclear Electric Xenon Ion System thruster CEX ion energy distribution is much more sharply peaked, with the majority of the ions ranging between 400 and 550 eV. Calculations from the code also indicated a small number of energetic ions in the 1 keV to 3 keV range. For both the NSTAR and NEXIS CEX distributions, the area under each curve has been normalized to facilitate a direct comparison.

In Figure 2.6, the impact angle distribution for ions striking the accelerator grid hole walls is given for both NSTAR and NEXIS thrusters. These calculations were again performed for this study

using the previously developed CEX2D code. As shown in the figure, the incidence angle θ will be defined with respect to the surface normal, in keeping with the convention used in most surface physics publications. Unlike the energies, which are strongly peaked at specific values, the angle distribution is much more uniform. For the 30 cm diameter NSTAR thruster, smaller angle collisions are preferred whereas in the larger 65 cm diameter NEXIS thruster ion impact occurs at higher angles.

2.3.3 Other Grid Failure Modes

During thruster operation, the upstream surface of the screen grid is constantly exposed to the discharge plasma environment. Because the screen is electrically tied to the cathode, it will have a lower potential than the plasma and will be subjected to ion bombardment. While single ions from the discharge will likely be of too low energy to do appreciable damage, doubly charged ions are twice as energetic and have been detected in significant quantities in 30 cm ion thrusters [Kolasinski, 2004]. Since the entire grid surface is exposed to this effect, the general result of this type of process is an overall thinning of the screen electrode. A particularly severe case of this occurred during a 2000 hr test of a 30 cm diameter engineering model thruster, where nearly 27% of the original material was removed from the grid centerline [Patterson, 1995]. A clear solution to this problem is reducing the discharge voltage, an approach that worked successfully in subsequent testing [Polk, 1996].

As previously mentioned, an unclearable grid short is another failure mechanism and occurs when a piece of conducting material becomes lodged in the small gap between the screen and accelerator grids. Such flakes may also originate from sputter deposited materials on the interior surface of the discharge chamber, or from debris in the launch vehicle fairing. This problem was initially encountered on the SERT II mission after its launch in 1970, when both thrusters experienced periods of high voltage recycling after 2000 hours of operation [Anderson, 2005]. To clear faults on the Deep Space 1 mission (launched in 1998), a high voltage grid clearing circuit was incorporated into the

power system to vaporize any flakes [Goodfellow, 1999]. An instance of continuous high voltage recycling was encountered during the mission after less than 5 minutes of beam extraction. The thruster restarted normally after a 2 week period of thermal cycling [Anderson, 2005].

2.3.4 Summary

Predictions of electron backstreaming voltage, screen grid transparency, and impingement current from codes such as CEX2D compare favorably with experiments, indicating that the present understanding of the underlying physics has reached a level of maturity needed for the quantitative analysis of most ion extraction systems. Determining the distributions of energy and impact angle for the CEX ions establishes the bombardment conditions necessary to calculate wear rates of the accelerator grid.

For the 30 cm NSTAR thruster design, the distribution of energies for the CEX ions that impact the accelerator grid apertures peaks at approximately 150 eV-200 eV. The ion angle of incidence distribution is much more uniform, although there appears to be a slight preference for smaller impact angles (closer to normal incidence). Because its sputtering yield is lower than most metals, carbon was used in the ion optics of the larger 65 cm diameter NEXIS thruster. From the CEX2D analysis, the incident ion energy distribution peaks at 450-500 eV, and glancing impact is preferred. From this analysis, Xe^+ sputtering yield data for Mo and C at these energies and incidence angles is needed for wear calculations. Previously published sputtering data for these materials under the bombarding conditions of interest are sparse. The existing experimental database will be examined in detail in Chapter 3, and sputter-resistant grid materials will be discussed in Chapter 5.

2.4 Hollow Cathode Sputtering Processes

A wide variety of plasma devices use hollow cathodes as an electron source. This type of cathode was initially incorporated into ion thruster designs in the mid-1960s [Rawlin, 1968] as a robust alternative to tungsten filaments. Because electron emission from the cathode is required to establish

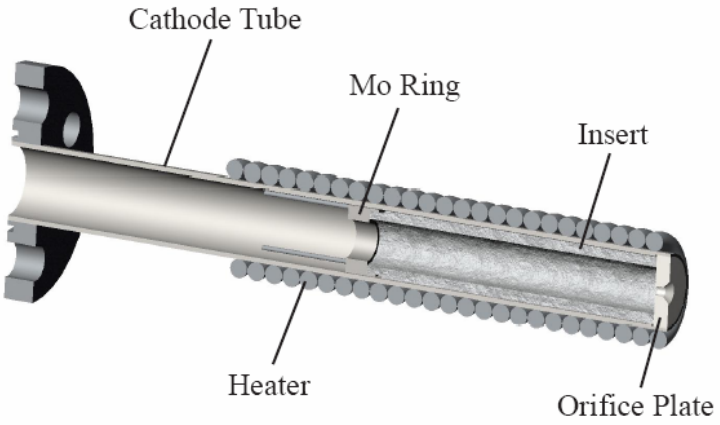

Figure 2.7: Cut-away view of a typical hollow cathode, from [Polk, 2004].

a plasma discharge, the failure of this component represents a thruster life limiting scenario. While hollow cathodes are capable of lengthy periods of operation, as demonstrated by a 30352 hr endurance test [Sengupta, 2003], extending their use to more taxing applications demands that the associated failure mechanisms be well understood.

2.4.1 Sputtering Mechanisms

An ion thruster hollow cathode cut-away view is shown in Figure 2.7. The major components include a hollow tube serving as the cathode body, an orifice plate, a heater coil, and a porous insert where electron emission takes place. The cathode body and orifice plate are generally fabricated from sputter-resistant refractory metals with low coefficients of thermal expansion, such as tungsten or molybdenum-rhenium alloys. In most modern designs, a small cylindrical electrode (referred to as the *keeper*) encloses the assembly depicted in Figure 2.7. Because the keeper is electrically connected to the anode through a 1 kΩ resistor, it floats at a potential approximately 5 V positive of the cathode, depending on the discharge conditions. The keeper shields the hollow cathode from sputtering damage while serving as a secondary anode, which allows a discharge to be initiated at lower starting voltages.

The emitted electron current that can be extracted with long life depends on numerous parameters including the cathode geometry, mass flow rates, and orifice diameter and aspect ratio [Domonkos, 1999]. Cathodes 0.635 cm (0.25 in.) in diameter have been used predominantly in ion engines because they provide suitable currents and acceptable life for thruster sizes between 15 cm and 40 cm. These cathodes typically operate at a propellant mass flow rate of 0.36 mg/s, with internal gas pressures of approximately 1300 Pa (10 torr) and are capable of emitting currents of 13 A or more. The electron current density emitted from the insert is dictated by the Richardson-Dushmann equation [Dushmann, 1930]:

$$j_{th} = FT_w^2 \exp\left(\frac{-q\phi_e}{kT_w}\right) \qquad \textbf{2.4}$$

In the above expression, T_w is the inner wall temperature of the insert, φ_e is the effective work function (corrected for field enhancement), and F=1.2×10^6 A/(mK)^2. From Equation 2.4, it is evident that the emission may be enhanced by both decreasing the work function and increasing the insert temperature. The insert is typically impregnated with barium calcium aluminate, and the presence of Ba adsorbed on a monolayer of oxygen on the emitter surface decreases φ_e. The transport of these compounds to the insert interior surface is a fairly complex chemical process that is still under investigation by a number of authors [Polk, 2004; Doerner, 2004]. The decrease in the work function allows emission to occur at temperatures of 1200 ºC or less. The heat input required to attain this temperature is provided by the external coaxial heater coil prior to startup, and by internal plasma bombardment once a discharge has been established.

Because the hollow cathode is constantly exposed to the discharge plasma, it is not surprising that many of its failure mechanisms are associated with sputtering processes. Failure modes specifically associated with the sputtering of the discharge cathode include: (a) erosion of the cathode orifice plate, (b) erosion of the keeper orifice plate, and (c) failure of the cathode heater due to thermal

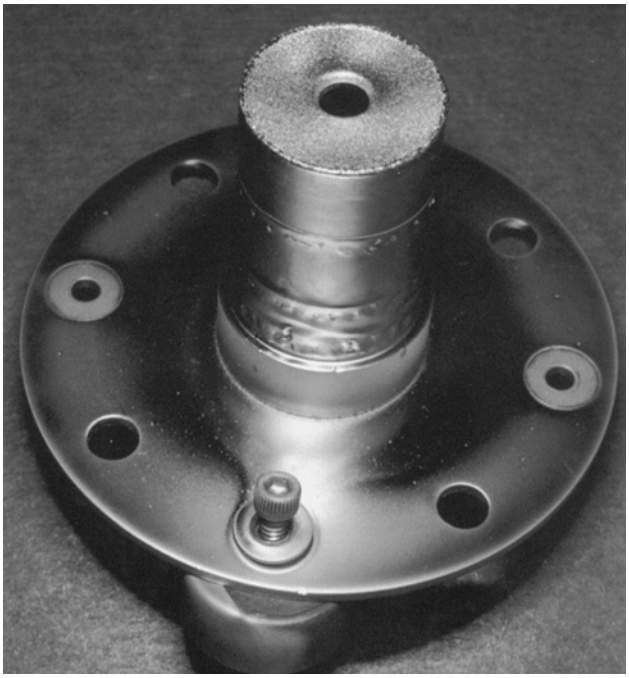

Figure 2.8: Photograph of the EMT2 keeper at the conclusion of the 8200 hr LDT.

cycling or erosion. Depletion of the low work function material in the cathode insert is also an important failure mechanism and will be addressed at the end of this section.

Erosion of the cathode orifice plate is a significant wear process due to the sensitivity of hollow cathode performance to orifice geometry. If the orifice widens due to erosion, operation at the desired electron emission currents and flow rates will eventually become impossible. Furthermore, structural failure will occur if the electron beam weld that joins the orifice plate to the cathode tube is damaged. While keeper erosion does not necessarily lead directly to cathode failure, significant wear of this component can leave the hollow cathode vulnerable to bombardment by high energy ions, eventually leading to orifice plate and heater failure. Reliability of the heater coil has been established to a high degree through space station plasma contactor endurance tests. During a study by Sarver-Verhey (1994) where one such cathode was operated over 28000 hours (equivalent to over 3 years of continuous operation), an engineering model contactor assembly underwent 3598 successful ignitions. If the heater is subjected to erosion processes, however, the inner and outer

conductors may become coated with metallic deposits and become shorted together, resulting in failure.

2.4.2 Observations from Long Duration Tests

At the conclusion of the initial 2000 hr test of the NSTAR thruster design, the cathode orifice plate was found to be badly damaged from sputtering. A subsequent 1000 hr endurance test incorporated an enclosed keeper design to mitigate this wear, and posttest analysis indicated that this objective had been effectively accomplished. Profilometry indicated an erosion rate of approximately 0.070 μm/hr on the keeper orifice plate [Domonkos, 2001], and negligible cathode wear. With this and a number of other endurance issues mitigated through design modifications, testing to the full 8000 hr design life of the thruster was initiated (known as the Life Demonstration Test, or LDT.) Posttest analysis from the LDT revealed that approximately 30% of the keeper orifice plate thickness had been worn away, and significant chamfering of the orifice itself had also occurred [Polk, 1999]. Figure 2.8 displays the keeper as it appeared at the conclusion of the LDT. Sectioning of the keeper orifice plate revealed the radial erosion profile, with a peak wear rate of 0.064 μm/hr averaged over 8192 hrs. A summary of these results is also provided in Table 2.1.

After Deep Space 1 was launched in 1998, an Extended Life Test (ELT) of the flight spare thruster (FT2) was initiated to evaluate the ultimate propellant throughput capability of the NSTAR thruster design. The previous three tests had been operated at the 2.3 kW throttle setting for the duration of the test. This point represents the maximum power level for this type of thruster, and was expected to yield the most severe erosion. The long duration of the ELT provided the engine designers with the opportunity to investigate other intermediate throttle levels as well. In addition, the ELT vacuum facility was equipped with improved diagnostics, including a platform with a camera capable of photographing the cathode assembly through the grids of the thruster. The camera provided sufficiently high resolution to allow for reasonably accurate measurements of the keeper

orifice area as a function of time. Camera images were taken approximately every 3000 hours to characterize the surface evolution of the different thruster components [Anderson, 2001].

The ELT would ultimately run for 30352 hours over a 5 year period, after which it was voluntarily terminated [Sengupta, 2003]. Figure 2.9 displays images of the cathode keeper orifice plate at different stages during the ELT. The photos suggest a much higher than anticipated wear rate in the ELT based on previous experience with the LDT and the 1000 hr test. The reasons for this increase are not yet well understood, although some insight may be gained by correlating the photographs with changes in thruster operating conditions. To given an indication of the erosion rate, the keeper orifice inner area is plotted against thruster operating time in Figure 2.10. The throttle levels indicated in this plot correspond to the set points given in Table 2.2. Note that at 4937 hours, the throttle level of the engine was changed from TH 15 to TH 8. After approximately 5935 hours of operation, the keeper shorted to cathode. This condition persisted until approximately 7604 hours, and intermittent shorting continued for approximately 1300 hours afterwards [Domonkos, 2001]. Photographs of the keeper taken after 4693 and 6408 hours indicate a significant change in the erosion pattern. A comparison of the photograph taken at 4693 hours and Figure 2.8 suggest an erosion profile similar to that seen after the 8200 hour test. The photograph taken after 6408 hours of operation displays substantial chamfering of the orifice plate. Rapid widening of the keeper orifice occurred afterwards and continued even after the thruster was throttled up to TH 15 at 10451 hours. This increase in erosion was surprising because the input power for TH 8 was approximately 2/3 of that for TH 15. Note that by the end of the life test, the keeper had worn away completely, exposing the cathode itself to plasma bombardment. Posttest analysis of the cathode assembly revealed substantial chamfering of the cathode and damage to the heater coil, similar to observations from the 2000 hr test.

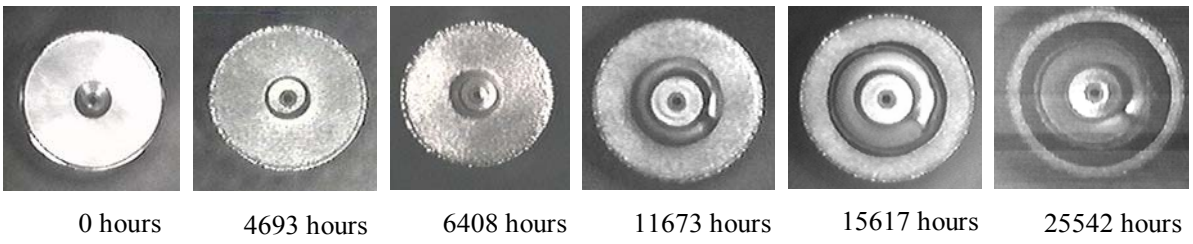

Figure 2.9: Evolution of the cathode keeper surface during the ELT.

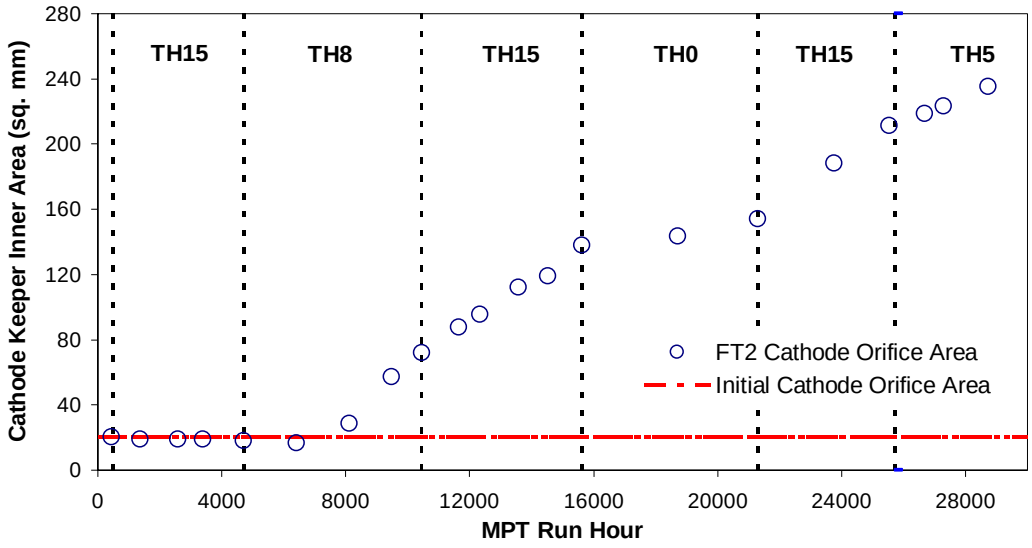

Figure 2.10: ELT cathode keeper orifice area as a function of time [Sengupta, 2003].

Table 2.2: Throttle level set points for the Extended Life Test (ELT).

TH Level	P_{TOT} (W)	$\dot{m}_{cath}$ (sccm)	$\dot{m}_{neut}$ (sccm)	$\dot{m}_{main}$ (sccm)	V_B (V)	J_B (A)	V_A (V)	J_{NK} (A)
0	0.52	2.47	2.40	5.98	650	0.51	-150	2.0
5	1.12	2.47	2.40	9.82	1100	0.81	-150	2.0
8	1.46	2.47	2.40	14.41	1100	1.10	-180	1.5
12	1.96	2.89	2.81	19.86	1100	1.49	-180	1.5
15	2.33	3.70	3.60	23.42	1100	1.76	-180	1.5

Severe keeper wear has also been observed in other long duration tests. In a study conducted at the National Aerospace Laboratory of Japan, a 3800 hour test of a 14 cm ion thruster with carbon-carbon grids revealed substantial wear of the keeper orifice plate [Hayakawa, 2002]. By the conclusion of the test, the orifice had opened up, exposing the cathode and its heater wire.

2.4.3 Bombardment Conditions

Computational models accurately predict the ion bombardment conditions for ion thruster grids, and the underlying physics of this process are well understood. This, however, is not yet the case for the discharge cathode, although recent experimental and modeling efforts provide significant insight into the relevant sputtering mechanisms. Given the low energy of most of the ions in the plasma discharge, the rapid sputtering damage observed during endurance tests suggests that mechanisms for higher energy (and perhaps multiply charged) ion production exist in this region of the thruster. To better understand these processes, Goebel (2005) initiated an experimental investigation to obtain plasma potential and electron temperature measurements using ultra-fast miniature scanning probes for different cathode operating conditions. To minimize disturbances to the plasma environment within the cathode and in the plume, the probes were pneumatically actuated at speeds of 2 m/s, and dimensions of the probe ceramics and electrodes were made as small as feasible. The actuation mechanism also allowed for precise positioning, with an achievable spatial resolution of 0.05 cm. This level of precision enabled repeatable characterization of the plasma along the centerline of the hollow cathode, and even in the small diameter orifice region. Probes also scanned radially within the cathode plume. In this study, Goebel found that plasma potentials were sensitive to the geometry of the anode and cathode, as well as to gas flow rate and discharge current. These factors were expected to have a significant effect on the ion bombardment conditions for the cathode surfaces [Goebel, 2005]. Goebel also noted a luminous plasma ball, which appeared to change position as a function of flow rate, as shown in Figure 2.11. In a later study by Jameson (2005), a retarding

potential analyzer (RPA) was placed near the exit of the cathode, both on-axis and at a small distance radially from the centerline. The RPA allows the energies of ions in the cathode plume to be characterized. The energy distribution of ions detected along the cathode centerline peaked at the discharge voltage (25 eV). On the other hand, ions that were detected at a small radial distance away from the centerline had an energy distribution that peaked at approximately 30 eV. In addition, the tail of the distribution contained a much larger population of higher energy ions (40 eV-90 eV). Predictions from a 2-D axisymmetric theoretical model developed by Mikellides (2005) compare well with many of the experimental observations. This model also provides considerable insight into processes that limit emitter life.

2.4.4 Other Cathode Failure Modes

Recall that the presence of Ba and O on the emitter surface lowers the work function of the insert, allowing operation at lower temperatures. However, over time, the concentration of these compounds at the surface may be reduced through a number of mechanisms. This may be due to depletion of the impregnate material, or to other processes that block the production of Ba compounds and their transport to the surface. These chemical processes are fairly complex and still not understood well enough to allow for a reliable predictive capability regarding their lifetime. Currently, ways to circumvent these problems, such as the development of reservoir cathodes [Polk, 2003] and investigations into the relationship between insert temperature and lifetime are being pursued [Polk, 2004].

2.5 Concluding Remarks

An analysis of the long duration testing database, coupled with computational modeling reveals that the ion bombardment conditions for grid surfaces in ion thrusters can be established with accuracy. For 30 cm diameter thrusters, the Xe^+ ions collide with the Mo surfaces with an energy distribution that is peaked at 150 eV-200 eV. Near-perpendicular incidence collisions are preferred in

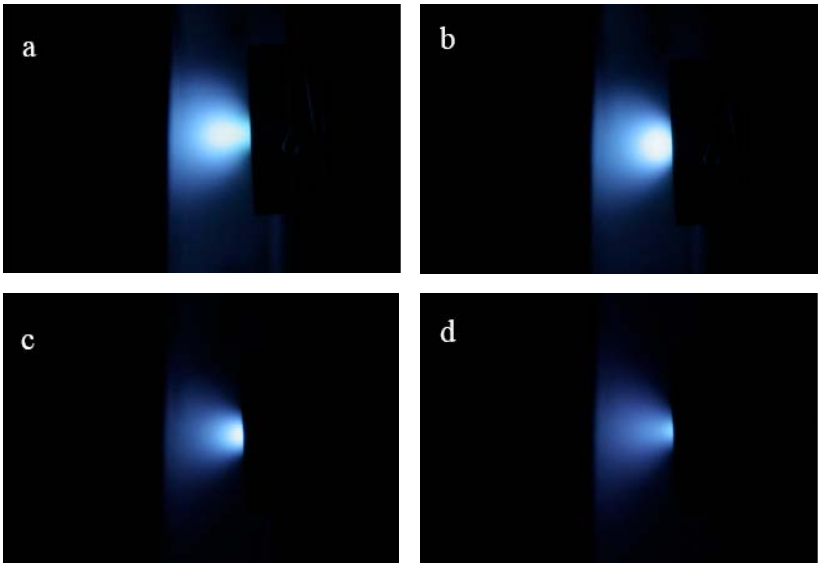

Figure 2.11: Photographs indicating cathode spot position for a 0.64 cm (0.25 in.) cathode operating at (a) TH 15 (b) TH 12 (c) TH 8 (d) TH 4 [from Jameson, 2005].

this configuration. For larger 65 cm diameter thrusters (which use carbon optics), the energy distribution peaks between 450 eV-500 eV, and glancing incidence collisions are favored. A better understanding of fundamental sputtering physics at low energies and glancing angles of incidence is needed for the bombardment conditions to be translated to accurate electrode mass loss calculations. A comprehensive review of previous sputtering literature relevant to grid wear will be provided in Chapter 3.

Ions in the cathode region of the thruster have been measured to have energy distributions that peak at 25-30 eV, although significant quantities of higher energy ions (40-90 eV) are also present. Because the ion fluxes to the cathode surfaces are not nearly as well defined for this region of the discharge chamber, diagnostics to rapidly measure cathode wear directly would be of greater benefit at this stage. A technique to accomplish this will be developed in greater detail in Chapter 7.

This page has been intentionally left blank.

Chapter 3: Sputtering Models and Experimental Results for Glancing Incidence

The plasma bombardment conditions and target properties have been established in Chapter 2 based on previous ion thruster experimental and modeling results. In the present chapter, the emphasis now shifts to determining the corresponding material removal rates, where sputtering models relevant to the wear of the ion optics and cathode are reviewed. Recall that ions created from charge exchange processes strike the thruster grid apertures at grazing incidence with fairly low energy (< 1 keV). Insight into the fundamental physics of sputtering at glancing incidence may be obtained by examining how a particle is scattered once it impacts a surface. The amount of energy that is transferred to the target atoms in the near surface region heavily influences the sputtering yield. It is useful to know how this energy is distributed within the solid, as well as the projectile ranges and the average dimensions of the collision cascades.

A number of theoretical and computational models are capable of simulating these processes. The most common approaches are transport theory and Monte Carlo codes, both of which use the binary collision approximation (BCA). The implications of this assumption are reviewed in the first segment of this chapter. Most sputtering studies rely heavily on the accuracy of collision cross sections as an input parameter, and a discussion of several relevant treatments follows. Analytical solutions to the Boltzmann transport equation are examined to determine the parameters that influence sputtering at different angles of incidence. A discussion of Monte Carlo models follows, along with their implementation for sputtering calculations.

As mentioned in previous chapters, published experimental sputtering data are sparse for the materials and bombardment conditions that are relevant to ion propulsion. An analysis of the requirements for accurate sputtering measurements is provided in the second half of this chapter, along with a detailed review of existing experimental results. A comparison of the experimental data

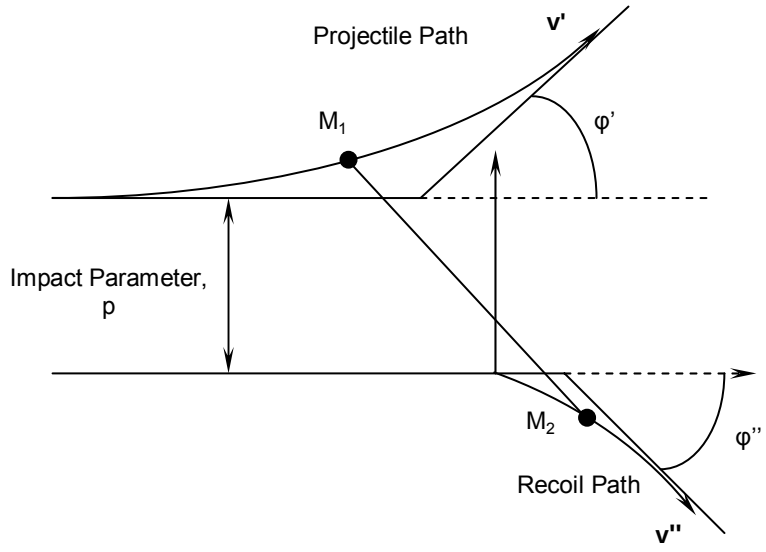

Figure 3.1: Binary collision geometry.

with the model predictions is used to identify the problems that motivate the specific topics of research in this thesis.

3.1 The Binary Collision Approximation

A key simplifying assumption used in many of the modeling approaches discussed herein is the binary collision approximation (BCA). This approximation treats all collisions as only involving two particles at a time, neglecting any multi-body interactions. This approximation is a necessary simplification that arises from the difficulty of defining cross sections for multi-particle collisions [Sigmund, 1969]. Both transport theory sputtering models and Monte Carlo codes such as TRIM [Ziegler, 1985] model collisions in this manner.

While it has been suggested that as a general guideline, the BCA will break down for projectile energies less than 100 eV [Ziegler, 1985], it is worthwhile to pursue a more quantitative analysis of the associated limitations. The geometry of a typical collision is displayed in Figure 3.1. As a projectile approaches a target particle, its direction and velocity change over a small distance. In the BCA, the collision is assumed to be instantaneous, and only the asymptotic behavior of the particles

after the collision is considered. This approximation is valid as long as the distance over which the velocity and direction change occurs is small compared with the interatomic spacing within the target. If this distance is comparable or larger, then the projectile and recoil atoms will have the opportunity to interact with multiple target atoms during the collision before they achieve the asymptotic behavior from the previous collision [Robinson, 1974].

Clearly the boundaries for where the BCA will be valid are not distinct, and the approximation fails gradually as the incident particle energy decreases [Eckstein, 1991]. A number of possible criteria may be used to determine its limitations. As an initial estimate, Robinson (1974) suggests comparing a collision time constant with the longitudinal wave speed in the material. A more precise treatment by Eckstein (1991) considers the worst case for the BCA, specifically large scattering angle, nearly head-on collisions. Under these circumstances, the projectile and recoil show the largest divergence from their asymptotic trajectories. For Mo→Mo and C→C collisions, this deviation becomes on the order of the interatomic spacing between the target atoms below energies of 23.6 eV and 26.4 eV, respectively [Eckstein, 1991]. In most cases, the initial projectile and recoil atom energies will be substantially higher than the limiting energies obtained from the above analysis. However, as energy is dissipated throughout the collision cascade, many subsequent recoil atoms will have energies that are less than this, bringing into question the BCA for these collisions.

Recall that large angle scattering of the incident particle is the worst case for the validity of the binary collision approximation, as this represents the largest deviation from the asymptotic trajectories [Eckstein, 1991]. For grazing incidence collisions, much smaller deflections of the projectile and recoil particles are expected. However, once the incident particle is deflected off of its original trajectory, subsequent collisions with other target atoms may occur at any angle. As a result, the validity of the BCA is not expected to depend on the angle of incidence of the projectile, and will remain valid at grazing incidence.

3.2 Collisions and Cross Sections

As an ion collides with a solid, it transfers a fraction of its kinetic energy elastically to target atoms and loses energy inelastically through interactions with electrons within the solid. Lindhard, Scharff, and Schiott (1963) consolidated many of these complex processes into a single model with simplified expressions for collision cross sections that could be readily incorporated into range calculations of ions and other particles in solids. These cross sections are of particular interest to the present study as they are used extensively in analytical sputtering models [Sigmund, 1969]. Using Lindhard's theoretical framework, Ziegler (1985) undertook a more detailed analysis of collisions to improve the accuracy of such cross sections for computational applications. These cross sections were incorporated into a Monte Carlo code TRIM (TRansport of Ions in Matter) that has been used throughout the field of surface science for the analysis of ion-surface interactions. A complete overview of collisions and cross sections may be found in published work by Ziegler (1985) and Duchemin (2001).

The deflection of the projectile and recoil atoms during a collision is governed by Coulomb repulsion between nuclei. However, the charge of the respective nuclei is shielded somewhat by the surrounding electrons. This effect can be best described by a screening function, given by [Ziegler, 1985]:

$$\Phi = \frac{V(r)}{Z_1 Z_2 q^2 / r} \qquad \textbf{3.1}$$

In the above expression, $V(r)$ is the interatomic potential at a radius r, and the denominator represents the potential due to the bare nuclei only. Note that Z_1 and Z_2 indicate the atomic numbers of the incident and recoiling particles, respectively. Based on the definition for the screening function, the expected behavior is for Φ to tend to 1 as $r \rightarrow 0$, and $\Phi \rightarrow 0$ for large r.

The difficulty here lies in determining $V(r)$, as it depends on the charge distribution due to the surrounding electrons. For the purposes of an analytical approach, a common solution is to use an

expression that depends only on atomic number (Z) and ignores any details of the electron shell structure. The Thomas-Fermi model for the potential distribution is particularly convenient for this purpose and is used in Lindhard's (1968) treatment of collision cross sections. Normalizing the spatial dependence by a screening length a_{TF} eliminates the dependence of Φ on Z [Lindhard, 1968]:

$$a_{TF} = \frac{1}{4}\left(\frac{9\pi^2}{2}\right)^{1/3} a_o \frac{1}{Z^{1/3}} = \frac{0.8853 a_o}{Z^{1/3}} \qquad \textbf{3.2}$$

Note that a_o is the Bohr radius (0.0529 nm.) The above expression is suitable only for an isolated atom and must be adjusted to apply to interatomic potentials. Lindhard suggests the following modification to the Thomas-Fermi screening length:

$$a_I = \frac{0.8853 a_o}{(Z_1^{2/3} + Z_2^{2/3})^{1/2}} \qquad \textbf{3.3}$$

Using the modified Thomas-Fermi model, the screening functions for all ion-target combinations collapse onto a single curve. Using this, Lindhard derived an expression for the differential cross section for screened Coulomb collisions. The Lindhard cross section is remarkable in that it may be reduced to a function of a single parameter t as shown below:

$$d\sigma = \pi a_I^{\,2} \frac{dt}{2t^{2/3}} f(t^{1/2}) \qquad \textbf{3.4}$$

In the above expression, the parameter t has been formulated so that its energy dependence is $t \sim T \cdot E$, where T is the energy transferred to the recoiling particle. The function $f(t^{1/2})$ is referred to as the *universal scattering function* and is evaluated numerically. However, a power approximation for f provides an analytical expression that may be used over limited energy ranges:

$$f(t^{1/2}) = \lambda_m t^{1/2-m} \qquad \textbf{3.5}$$

The value of m depends on the energy range, and is an indication of how heavily the nuclei are screened. Generally, m ranges between 0 and 1, and for the low energies of interest in this study, the approximation m=1/3 is appropriate [Winterbon, 1970]. Values of the dimensionless constant λ_m are

tabulated by Winterbon (1970) and Sigmund (1981). With the power approximation, the differential cross section may be expressed in terms of E and T as [Lindhard, 1968]:

$$d\sigma(E,T) \cong C_m E^{-m} T^{-1-m} dT \qquad \textbf{3.6}$$

The constant C_m is defined by

$$C_m = \frac{\pi}{2} \lambda_m a^2 \left(\frac{M_1}{M_2} \right)^m \left(\frac{2Z_1 Z_2 q^2}{a_I} \right)^{2m} \qquad \textbf{3.7}$$

The nuclear stopping cross section S_n is a convenient alternative to $d\sigma$ because it is directly related to the specific energy loss dE/dR given by

$$S_n(E) = -\frac{1}{N}\frac{dE}{dR} = \int_0^{\gamma E} T d\sigma \qquad \textbf{3.8}$$

where $\gamma = 4M_1M_2/(M_1+M_2)$ is the *reduced mass*. The results from Lindhard's cross section derivation are remarkable given their accuracy over a wide energy range. As previously mentioned, the Thomas-Fermi atomic model neglects some of the details of the surrounding charge distribution. In addition, approximations made in the derivation of $d\sigma$ for collisions where the projectile is deflected over a large angle lead to inaccuracies at low energies [Lindhard, 1968].

To address these shortcomings, Ziegler (1985) used computational methods in a more sophisticated treatment of collisions. Since the ultimate objective of this work was to apply these results to Monte Carlo simulations of ion stopping in solids, a computationally efficient approach was necessary from a practical standpoint. Sophisticated Hartree-Fock-Slater charge distributions provide a much more realistic model of the electron shells than does the Thomas-Fermi model. A comparison of the two charge distributions for the case of molybdenum is shown in Figure 3.2. Such charge distributions are unique to each atom and were too complex to be efficiently incorporated into repeated Monte Carlo calculations. To avoid this problem, Ziegler instead calculated interatomic screening functions for 522 randomly selected atomic pairs (out of roughly 8×10^3.) A subsequent

statistical analysis revealed that the screening functions Φ were roughly independent of Z when normalized according to a *universal* screening length:

$$a_U = \frac{0.8853 a_o}{Z_1^{0.23} + Z_2^{0.23}} \qquad \textbf{3.9}$$

Using this modified coordinate system, Ziegler applies a curve fit to the 522 individual screening functions to obtain a single universal $\Phi_U(r/a_U)$. The details of this fit are discussed in Ziegler's reference volume (1985).

As an incident ion penetrates a target medium, it transfers some of its energy to the electrons within the solid, resulting in excitation or ionization processes. Because this does not result in a change in the kinetic energy of the target atom, such interactions are often referred to as *inelastic* energy losses. The general governing expression proposed by Lindhard (1963) for such interactions is

$$S_e = KE^{1/2} \qquad \textbf{3.10}$$

The constant K depends on ion and target masses. From the above expression, the electronic stopping cross section is proportional to incident ion velocity. The importance of electronic stopping decreases relative to nuclear stopping at low energies and, for the conditions of interest in this study, it is generally permissible to ignore the effects of electronic stopping.

3.3 Transport Theory Models

The most influential study to apply transport theory to the problem of sputtering was conducted by Sigmund (1969). The results of Sigmund's study, which is based on previous models of high energy particle transport in solids, have been used throughout the field of surface science [Smentkowski, 2000]. The model takes into account most of the fundamental aspects of sputtering from first principles and is used to calculate normal incidence sputtering yields as well as range and damage distributions within the solid. The calculated yields generally show remarkably good agreement with published experimental studies at normal incidence (typically within a factor of 2 and

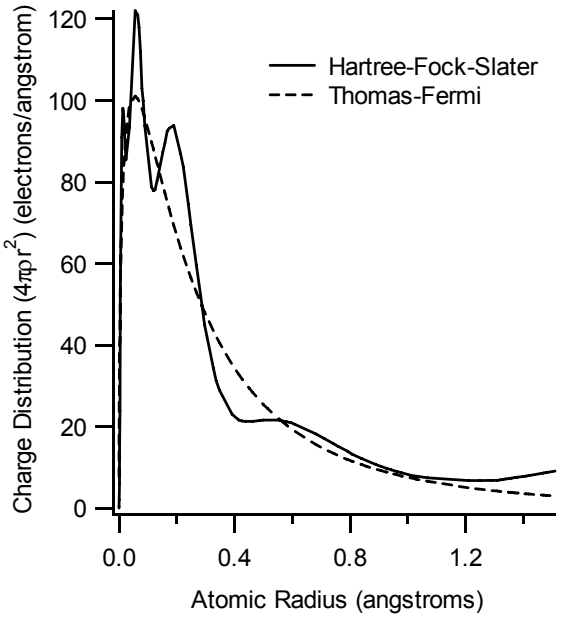

Figure 3.2: Comparison of Thomas-Fermi and Hartree-Fock-Slater charge distributions for molybdenum.

in some cases, within 40%). The portions of the work directly applicable to the angular dependence of sputtering yields are emphasized here.

3.3.1 Underlying Assumptions

In the transport theory approach, the target material is assumed amorphous and crystal structure is typically neglected. This may initially appear to be a gross simplification, given experimental evidence showing a strong dependence of sputtering yields on lattice structure and orientation with respect to the beam. However, for polycrystalline metals, the grains are randomly oriented with dimensions that are typically much smaller than the irradiation area. With this factor in mind, the assumption of an amorphous target appears to be a fair approximation for most polycrystalline metals and at the energy levels of interest in this study. In the case of carbon composite materials, the assumption of an amorphous target is potentially more questionable due to the anisotropic bonding structure of graphite. The effect of crystal structure on graphite materials is discussed in further detail in Chapter 5.

The assumption that is likely to have the most significant influence on sputtering at varying angles of incidence is the treatment of the free surface. Sigmund assumes that the target is infinite in extent and the surface is taken to be an imaginary plane in an infinite medium. This approximation models collisions near the surface inaccurately. Furthermore, the target surface is also taken to be atomically flat. Whether or not this is an important consideration depends on the dimensions of the collision cascades and the relative size of the surface features. Most "real" surfaces have an RMS roughness that is larger than the penetration range of most ions in solids, causing local angle of incidence effects to be of importance. Both of these effects are discussed in greater detail in Chapter 6.

3.3.2 General Formulation

The transport theory approach differs from both Monte Carlo and molecular dynamics simulation approaches because it does not consider the details of individual particle trajectories. Instead, the number of particles with a given velocity and position is classified by a distribution function $G(\boldsymbol{r},\boldsymbol{v})$. As a result, the transport theory approach provides less detailed information than alternate methods where individual collision cascades are simulated. The function $G(\boldsymbol{r},\boldsymbol{v})$ may be interpreted to represent the distribution of projectiles and recoils within the solid averaged over many collision cascades [Winterbon, 1970]. In many cases, this information is much more useful than the exact details of each collision, and can be obtained directly from the solution of the Boltzmann equation, rather than through a statistical analysis of thousands of Monte Carlo simulations.

The distribution function discussed above satisfies the following integral equation:

$$-\frac{1}{v}\frac{\partial}{\partial t}G(x,\vec{v}_o,\vec{v},t)-\frac{\vec{v}}{v}\frac{\partial}{\partial \vec{r}}G(x,\vec{v}_o,\vec{v},t)=N\int d\sigma[G(x,\vec{v}_o,\vec{v},t)-G(x,\vec{v}_o,\vec{v}',t)-G(x,\vec{v}_o,\vec{v}'',t)] \qquad \textbf{3.11}$$

The variables *v'* and *v''* refer to the velocity of the recoiling target atom and projectile, respectively (as noted in Figure 3.1.) Equation 3.11 is a modified version of the Boltzmann equation with several important simplifications. First, acceleration due to external magnetic or electric fields has been

neglected. Collisions are assumed to occur over such a short period of time that any change in velocity of the particles may be considered instantaneous and treated with the collision operator on the right side of Eqn. 3.11. This collision integral also assumes dilute cascades, where only a small fraction of the particles in the target is moving at a given time. The form shown above (known as the "backward" Boltzmann equation) is slightly different from the more common forms of this equation. The equivalence of Eqn. 3.11 with the more common form has been previously demonstrated [Sigmund, 1981].

Eqn. 3.11 allows the damage distribution to be calculated because scattered recoil atoms are included in the collision integral within the $G(\boldsymbol{r},\boldsymbol{v_o},\boldsymbol{v''},t)$ term. If one is interested in only the range distribution, this equation may be simplified to [Sigmund, 1969]:

$$-\frac{1}{v}\frac{\partial}{\partial t}G(x,\vec{v}_o,\vec{v},t)-\frac{\vec{v}}{v}\frac{\partial}{\partial \vec{r}}G(x,\vec{v}_o,\vec{v},t)=N\int d\sigma[G(x,\vec{v}_o,\vec{v},t)-G(x,\vec{v}_o,\vec{v}',t)] \qquad \textbf{3.12}$$

Both Eqns. 3.11 and 3.12 hold only if the incident and recoiling particles are composed of the same atoms. For the case of two different species, an additional distribution function must be specified for the target material.

3.3.3 Solution Method

The general solution procedure for Eqns. 3.1 and 3.2 is discussed in detail by Sigmund (1969), Sanders (1968), and Winterbon (1970), and only the main features are highlighted here. The transport equations contain eight variables, including a spatial coordinate x, two velocities with components in three dimensions, and a time t. Integration over time and velocity allows the distribution function G to be expressed as a function of only three parameters, including a spatial coordinate x, the incident ion energy E, and the direction of the incident particle $\eta=\cos(\theta)$. The transformed distribution function is expressed as $F(x, E, \eta)$.

For the purposes of this analysis, the solution objective is to obtain expressions which allow F to be reconstructed. A common approach is to expand the η dependence of the distribution function F as a sum of Legendre polynomials, $P_l(\eta)$:

$$F(x,E,\eta)=\sum_{l=0}^{\infty}(2l+1)F_l(x,E)P_l(\eta) \qquad \textbf{3.13}$$

After incorporating this expansion into Eqn. 3.1 or 3.2, spatial moments of the distribution function are calculated:

$$\int_{-\infty}^{\infty}F(x,E,\eta)x^n dx=\sum_{l=0}^{\infty}(2l+1)F_l^n(E)P_l(\eta)$$
$$F_l^n(E)=\int_{-\infty}^{\infty}F_l(E)x^n dx \qquad \textbf{3.14}$$

This yields a system of integral equations that may be used to solve for individual $F_l^n(E)$. These are incorporated into an Edgeworth expansion to reconstruct the original distribution $F(x, E, \eta)$ [Winterbon, 1970]. This process is discussed in greater detail in Chapter 6.

3.3.4 Major Results

The transport theory approach outlined by Sigmund is effective for predicting sputtering trends for angles of incidence up to 50° from normal. In many cases, the existing experimental yield data agree with Sigmund's predictions to within a factor of 2. Of particular interest for the present review is Sigmund's result for heavy ion sputtering at normal incidence in the low keV energy range:

$$Y(E)=0.0420\alpha\frac{S_n(E)}{U_s} \qquad \textbf{3.15}$$

The constant α is evaluated in Sigmund's original work (1969); it depends on mass ratio (M_1/M_2) and weakly on incident ion energy. It is interesting to note that the above expression predicts that Y follows the same energy dependence as the nuclear stopping cross section, S_n. For low energies (E<1

keV) where the Lindhard (1968) cross sections are expected to be of limited accuracy, Sigmund suggests the following relationship for Y

$$Y(E) = \frac{3}{4\pi^2}\alpha\frac{\gamma E}{U_s} \qquad \textbf{3.16}$$

The transport theory solution is also effective for predicting the variation of sputtering yield as a function of angle of incidence for small θ with respect to the surface normal. Under these conditions, this variation is given by

$$\frac{Y(E,\theta)}{Y(E,0)} = (\cos\theta)^{-f} \qquad \textbf{3.17}$$

The exponent f depends weakly on mass ratio, M_1/M_2, and f=5/3 is a reliable approximation under most circumstances. For many of the experimental studies for which data are available, the sputtering yield increases monotonically and follows the $(\cos\theta)^{-f}$ until θ=50º. The rate of increase slows at this point, achieves a maximum for 50º≤θ≤80º and decreases rapidly thereafter. Specific experimental results will be discussed in Section 3.5.

3.4 Monte Carlo Methods

While analytical models such as the one proposed by Sigmund are useful in identifying trends and determining the dependence of sputtering yields on parameters such as ion mass, etc., often the simplifications required to make the mathematics tractable decrease their accuracy. Monte Carlo simulations are capable of treating complex physical phenomena in a more direct manner.

3.4.1 General Approach

The accurate collision cross sections developed by Ziegler are incorporated in a widely used Monte Carlo program, TRIM (TRansport of Ions in Matter), introduced in 1985. In addition to the previously mentioned BCA approximation, the program assumes an amorphous target, ignoring any crystal structure effects. Unlike the transport theory treatment, this model tracks the detailed

trajectories of individual particles. This approach allows greater flexibility with the target geometry, and TRIM is not constrained by the infinite medium assumption required to make the transport theory solution tractable. The ability to model the target as a half-space allows for a much more accurate modeling of collisions near the surface. A major disadvantage of Monte Carlo codes is that a large number of simulations is required in order to obtain statistically meaningful results. Such an approach can obscure the insights into sputtering physics that are otherwise clearer with analytical approaches.

3.4.2 Implementation for Sputtering Calculations

As previously mentioned, in TRIM collisions are treated using the sophisticated Hartree-Fock-Slater charge densities. The initial position of the projectile ion is varied randomly over an atomic diameter [Eckstien, 1991]. Beginning with a given energy, position, and direction, the trajectories of a large number of incident ions are calculated based on the scattering angle after a collision:

$$\Theta = \pi - 2\int_{-\infty}^{\infty} \frac{p\,dr}{r^2\left[1 - \frac{V(r)}{E_c} - \frac{p^2}{r^2}\right]^{1/2}} \qquad \textbf{3.18}$$

Note that p is the impact parameter shown in Figure 3.1, and E_c is the center of mass kinetic energy. Nuclear interactions are treated as distinct events that cause the incident particle to change direction. The ion travels in a straight line between collisions and loses energy continuously due to electronic stopping. Further interactions between the target and incident particles are tracked until the ion energy falls below a preset value.

The recoils that could potentially contribute to sputtering are also tracked, typically for as long as their energy remains above the surface binding energy of the solid and their position is in close proximity to the target surface. Once a recoil reaches the surface, its energy is calculated based on its velocity component normal to the surface. If found to be higher than the binding energy, U_s, the

particle is sputtered; otherwise, it is reflected back into the solid where it undergoes additional collisions.

The treatment of sputtering in TRIM captures the behavior of the yields as a function θ much more accurately than transport theory at glancing incidence. Simulated sputtering yield curves using this program appear to be in accord with experimental light ion sputtering data [Biersack, 1987].

3.5 Experimental Measurements

By defining sputtering yields for a particular ion-target combination, one is able to summarize the processes discussed in the previous section with a single statistical variable. While this allows for a direct correlation between material removed and incident ion flux, it is clear that the yield has a complex dependence on the target crystal structure, surface roughness, incident ion energy, and numerous other factors. This contributes to the difficulty associated with obtaining experimental sputtering yields, and the noticeable lack of reproducibility between yields measured in different laboratories can be partly attributed to an inadequate characterization of the experimental conditions [Anderson and Bay, 1981].

It is worthwhile to investigate the measures that will ensure that the true sputtering behavior is not masked by any of the secondary effects mentioned above. Such an analysis not only provides guidance for designing an experimental sputtering study, but also allows existing measurements that are potentially suspect to be identified. A review of experimental techniques was conducted by Anderson and Bay (1981), Smentowski (2000), and Duchemin (2001) and the topics of interest to this study are highlighted here. Parameters that affect the sputtering behavior can be subdivided into four categories comprising the ion beam, the mass loss measurement technique, the target crystal structure and topography, and the vacuum chamber background gas composition [Anderson and Bay, 1981]. Because the sputtering yield depends directly on the accuracy of the measurements of the incident ion flux and mass loss, these aspects of the experiment are considered to be of prime importance.

The incident ion flux must be accurately characterized. Generally plasma discharges include impurities, making their properties difficult to determine. In this configuration, the target is used as the anode surface, and the energy of the incident ions is controlled by applying a bias voltage. However, the electrons present in the discharge cause the formation of a sheath. A potential field is created such that ions entering the sheath are turned so that they strike the target at normal incidence, regardless of its orientation. As a result, this configuration cannot be used to investigate the angular dependence of sputtering yields.

For these reasons, a more sophisticated approach has been used in the past to measure incidence angle effects. Typically, a plasma discharge is initiated, and ions are extracted into a beam. To ensure that the beam is well defined in terms of species and contains no undesirable charge states, a series of magnetic and electrostatic filters is employed to separate unwanted impurities. Differential pumping of the acceleration region prevents significant charge exchange and reduces the fraction of energetic neutrals in the beam. The ion current to the target is measured with a Faraday cup to prevent the effects of secondary electron emission from coming into play. This configuration is shown in Figure 3.3.

The simplest means of determining the material removal rate is to measure the mass loss gravimetrically before and after ion bombardment using a mechanical balance. This method has the advantage of providing an unambiguous, direct measurement of the material removed. However, it is also a low sensitivity technique and requires stable ion beam operation for periods of several days (for most current densities). Thickness change measurements have also been used in numerous instances [Blandino, 2000] and generally involve masking a polished surface with a sputter-resistant material. The exposed area will erode, creating a step once the mask is removed. The step height may be assessed by stylus profilometery and correlated to the amount of mass removed. Because ion etching introduces surface features, the exposed surface is generally very rough. This may introduce difficulty in estimating the eroded volume, and several scans may be required to fully determine the three-dimensional shape of the crater. Techniques that rely on piezoelectric quartz crystal

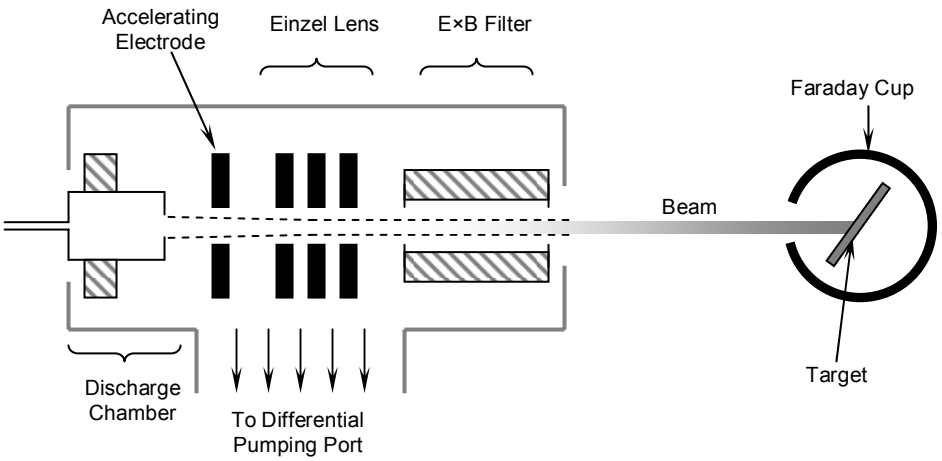

Figure 3.3: Typical experimental setup for sputtering measurements.

microbalances (QCMs) have also been used as a means of determining the mass loss of thin films during ion bombardment [Anderson and Bay, 1972; Duchemin, 2001]. The material removed from the coating by etching may be correlated to a shift in the resonance frequency of the QCM. The high mass sensitivity of the QCM makes it especially attractive for the low energy measurements of the present work, and further details regarding this technique may be found in Chapter 4. Spectroscopy has also been used to measure the efflux of particles from a surface during bombardment. Doerner has used this approach for very low energy (<100 eV) sputtering measurements (2003) at the University of California, San Diego.

These general guidelines are discussed in more detail in the following chapter, as they are applied to the design of a practical experimental setup to measure sputtering yields. A summary of prior experimental sputtering work related to the angular dependence of sputtering yields is given in Table 3.1.

An initial study on the angular dependence of sputtering yields was conducted by Wehner in 1959. His method involved immersing a set of polycrystalline spheres in an ion beam until a change in shape could be measured (typically on the order of several weeks). The sputtering yields were determined by examining a micrograph of the eroded sphere shape and determining the approximate

thickness change as a function of angle. While Wehner's initial data demonstrated many of the trends observed in previous experiments in terms of the overall behavior, there was a significant amount of scatter in the results, as the spheres did not appear to erode uniformly. In addition, contamination from the vacuum pumps was observed to have created sputter resistant layers on the targets, systematically biasing the measured yields.

An early study by Molchanov (1961) included measurements of Cu sputtering yields as a function of angle of incidence. For small θ, a $(\cos\theta)^{-1}$ dependence of $Y(\theta)/Y(0)$ was observed. At higher angles of incidence, the sputtering yields decreased after achieving a maximum between 75° to 80°. This study was the first to recognize a cosine dependence of the sputtering yield curve at low angles of incidence (a fact that would later be demonstrated from a theoretical standpoint by Sigmund).

Oechsner's study (1973) was one of the few to systematically investigate the effects of varying the projectile energy and mass. The maximum yield angle, θ_{max}, decreased as ion mass was increased, while the value of $Y(\theta_{max})/Y(0)$ increased for heavier ions. A less clear dependence of $Y(\theta_{max})$ on ion energy, E, was observed, however. Oechsner's measured sputtering yields at normal incidence appear to be systematically higher when compared with those of other studies. Changes in the target surface topography were not characterized as part of this study.

More recently, the effect of surface roughness on argon-bombarded Cu targets was investigated recently by Stepanova (2002). The Ar^+ angle of incidence was found to significantly alter the surface topography of the Cu target, and the roughness conditions affected the magnitude of the total sputtering yields. From Table 3.1, most of the experimental studies were performed with weight loss techniques. A high ion flux to the target is required to obtain a mass change that is within the sensitivity of most mechanical balances within a reasonable amount of time (as shown by j_b), which would aggravate this effect.

Table 3.1: Heavy ion sputtering experimental results.

Reference	*	Ion	Energy (keV)	Target	j_b	P (torr)	θ	Comments
Wehner (1959)	T	Hg	0.125-0.8	Fe, Ta, Mo, Au, Ag, Pt	1 mA/cm^2	Not Specified.	0°-70°	Spheres immersed in plasma environment, Y determined from thickness change as a function of angle.
Rol (1960)	W	Ar, Tl	20	Cu	~100 μA/cm^2	Not Specified.	0°-50°	
Molchanov (1961)	W	Ar	27	Cu	1-2 mA/cm^2	1-2×10^{-7}	0°-84°	First recognized a decrease in Y at large θ. Found $(\cos\theta)^{-1}$ dependence for θ<70°.
Rosenberg (1962)	W	Xe	0.1-0.6	Mo	2-8 mA/cm^2	10^{-7}-10^{-6}	0°	Low energy normal incidence experiments. Thirty different targets studied, only Mo expts. considered here.
Cheney (1965)	W	Ar	37	Cu	50-100 μA	10^{-7}-10^{-6}	0°-89°	Effects of surface roughness investigated for Cu targets.
		Xe	30	Cu	10-30 μA			
		Xe	30	Mo	10-30 μA			
		Xe	9.5	Mo	10-30 μA			
		Xe	30	W	10-30 μA			
		Xe	9.5	W	10-30 μA			
Oechsner (1973)		Ar	1.05	Al, Ti, Ni, Cu, Zr, Pd, Ag, W, Au	2-7 mA/cm^2	3×10^{-7}	0°-85°	Performed systematic investigation of the effects of ion mass and energy on $Y(\theta)$.
		Kr	1.05	Cu				
		Xe	1.05	Cu				
Blandino (2000)	T	Xe	0.15-0.75	Mo	0.6-4.6 mA/cm^2	2.1×10^{-4} (Test press.) 1.1×10^{-9} (Typ. base press.)	9°-15°	Investigated the effects of crystal structure on sputtering yield. Angular dependence not investigated in this case; angles represent angle of incidence considering beam divergence of source.
		Xe	0.15-0.75	C-C	0.6-4.6 mA/cm^2			
		Xe	0.15-0.75	CVD Diamond	0.6-4.6 mA/cm^2			
		Xe	0.15-0.75	Single Crystal Diamond	0.6-4.4 mA/cm^2			
Stepanova (2002)	T	Xe	0.4-0.8	Cu	0.11- 0.23 mA/cm^2	1-2×10^{-6} (Typ. base press.)	0º-75º	Investigated the effects of surface roughness on sputtering yields. SEM and x-ray diffraction analysis of the surface.

*Indicates the diagnostic technique used, W=weight loss, T= thickness change measurement

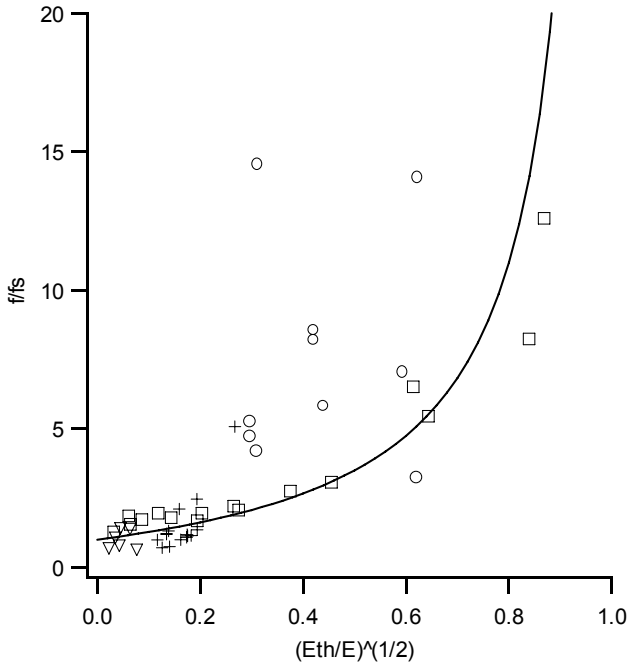

Figure 3.5: Yamamura curve fit comparison with experimental data.

3.6 Empirical Models

Yamamura (1984) proposed an empirical model designed to predict the behavior of $Y(\theta)/Y(0)$ over a large range of incidence angles. The fitting function contains a $(\cos\theta)^{-f}$ dependence similar to the predictions of Sigmund's theoretical model in addition to an exponential decay term that becomes significant as θ approaches 90°. The curve fit resulting from the combination of these two effects appears to match the general behavior displayed by most experimental data:

$$\frac{Y(\theta)}{Y(0)} = \frac{\exp[-\Sigma((\cos\theta)^{-1}-1)]}{(\cos\theta)^{f}}$$

The adjustable parameters, f and Σ, are based on fits to the experimental results of Wehner (1959), Cheney (1965), and Oechsner (1973).

The fit equation for f is given by

$$\frac{f}{f_s} = 1 + 2.5\frac{(E_{th}/E)^{1/2}}{1-(E_{th}/E)^{1/2}}$$

Expressions for the threshold energy (E_{th}) are given in Yamamura's original publication (1984). The symbol f_s refers to the exponent f predicted by the Sigmund theory. The use of a modified $(\cos\theta)^{-f}$ dependence appears to be a reasonable approach for an empirical model, although the fit parameters do not appear to match well with existing experimental data, as shown in Figure 3.5, especially for large values of E_{th}/E. Much of the existing data from this range is derived from Wehner's experiments as well as computational work performed by Yamamura. At the time the model was published, reliable data for heavy ion sputtering were (and still are) relatively sparse. Because of this, the author admits difficulty in formulating an empirical model for heavy ion sputtering.

3.7 Comparison of Experimental Data with Existing Models

To evaluate the predictive capability of the models discussed in the previous sections, each is applied to heavy ion sputtering for $Xe^+ \rightarrow Cu$, and $Xe^+ \rightarrow Mo$ combinations and plotted in Figure 3.6. For the Sigmund and Yamamura formulas, the normal incidence sputtering yield was calculated by means of an empirical formula developed by Matsunami (1984). TRIM calculations are particularly sensitive to input parameters such as the surface binding energy, U_s. For the calculations shown in Figure 3.6, the binding energy was adjusted so that the calculated normal incidence sputtering yield agreed with the empirical model prediction.

Agreement between the models and the experimental data does not appear to be sufficient for accurate predictions of thruster service life, especially for $\theta > 45°$. Sigmund clearly indicates that his theory is not applicable to glancing incidence, and for this reason the lack of agreement between his theory and the experimental data is not unexpected. The most impressive results appear to be the TRIM simulations where the general trends exhibited by the experimental data appear to have been reproduced accurately by a fairly fundamental modeling approach. The empirical Yamamura fit, while displaying the correct general behavior, does not appear to predict the peak sputtering yield, $Y(\theta_{max})$, well.

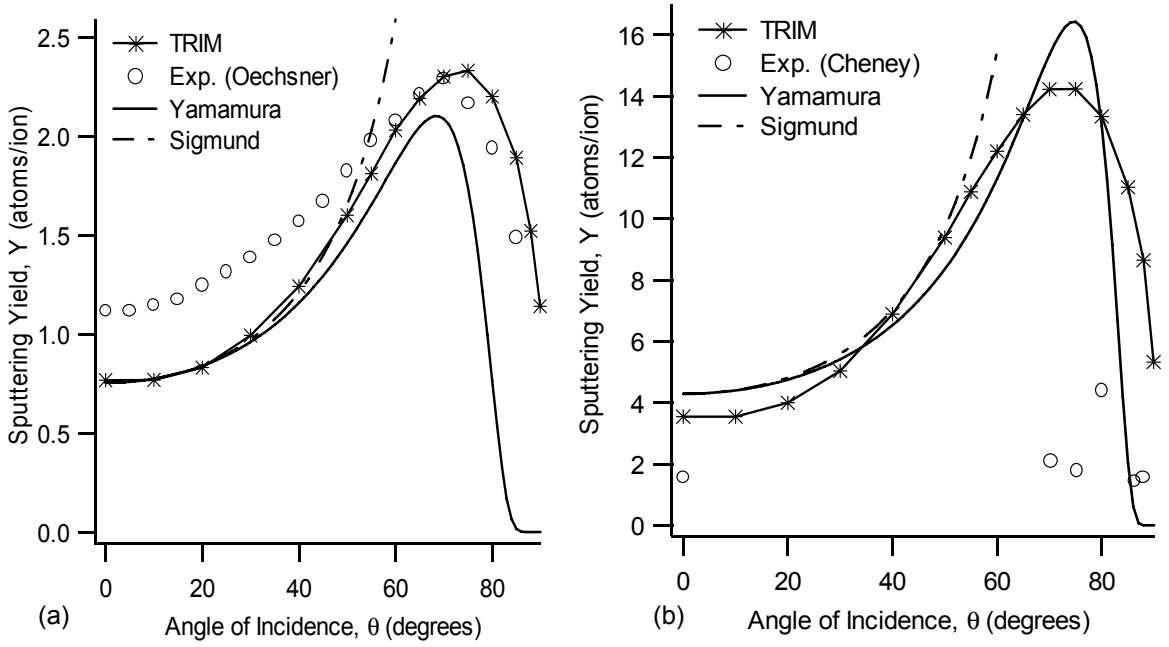

Figure 3.6: Variation of sputtering yield with angle of incidence for (a) Xe+ bombardment of a Cu target at 1.05 keV and (b) variation of sputtering yield with angle of incidence for Xe+ bombardment of a Mo target at 9.5 keV.

The disparity between the theory and experiments cannot be attributed to the inadequacy of the models alone, however. Given the difficulties associated with obtaining sputtering measurements, the experimental errors likely contribute significantly to the uncertainties mentioned above as well.

3.8 Concluding Remarks

The models that currently exist for sputtering do not address the effects of ion angle of incidence with a sufficient level of accuracy for reliable estimates of ion thruster grid life. The Sigmund model is not valid at low energies and at oblique angles of incidence. The Yamamura empirical formula shows good agreement with experiments for light ion bombardment; however, the lack of quality experimental data for heavy ions has impeded the development of a model for these conditions. TRIM simulations have also been applied with reasonable success to light ion sputtering at varying angles of incidence. Although it appears to predict reasonable trends for heavy ion sputtering,

additional experimental data at low energies and at glancing angles would be valuable in verifying the program's predictive capability for the specialized application.

The need for more reliable experimental results at grazing incidence is clear. New experimental studies should include a detailed analysis of the target material that characterizes surface roughness and crystal structure. A systematic investigation of the dependence of the yields on energy, target material, and angle of incidence would be invaluable for service life modeling of ion thruster grids.

Chapter 4: Sputtering Yield Measurements at Glancing Incidence Using a Quartz Crystal Microbalance

Proper modeling of ion optics endurance requires that the angular dependence of low energy heavy ion sputtering be well understood. As discussed in Chapter 3, the present experimental database is insufficient for this purpose and should be supplemented with data for conditions more relevant to thruster wear. To accomplish this task, an experimental facility equipped with a low energy ion source was developed to simulate the bombardment conditions on the grid apertures and downstream surface. The diagnostic for measuring the mass loss was a piezoelectric quartz crystal microbalance (QCM) coated with thin films of thruster materials of interest. The QCM target was etched with the ion beam, and a mass loss rate was determined from a resonance frequency shift due to changes in the mass loading conditions of the crystal. The high sensitivity of this technique, which is capable of detecting changes in mass loading of 5×10^{-9} g, makes it suitable for the low etch rates encountered in electric propulsion applications.

This chapter focuses primarily on the development of the experimental technique and hardware used to measure sputtering yields, beginning with a discussion of the ultra-high vacuum (UHV) facility and diagnostics. Emphasis is placed on the experimental requirements for achieving accurate grazing incidence measurements. A detailed discussion of the techniques used to filter and characterize the ion beam follows. Surface diagnostics used to ensure that the thin coatings on the QCMs accurately mimic the properties of the bulk material are described. The experimental procedure is discussed, along with the data and error analysis. The chapter concludes with sputtering results at varying incidence for several metallic targets.

4.1 Experimental Hardware

As discussed in the previous chapter, numerous methods for measuring sputtering yields have been used in the past, including weight loss, spectroscopy, and profilometry. The QCM technique used in the present study has the advantage of being an *in situ* technique as well as offering a direct measurement of mass loss. As an ion beam bombards the thin film, atoms are ejected from the surface and the resonance frequency of the QCM changes. For a given change in areal mass density σ, the shift in frequency, υ, will be given by $\Delta\sigma/\sigma_o=\Delta\upsilon/\upsilon_o$. This expression is valid only for small mass changes, but its useful range can be extended significantly by using more sophisticated relationships between frequency change and mass loss [Lu, 1974]. A disadvantage associated with this technique is that the physical properties and sputtering behavior of thin films deposited on the QCM surface may not resemble the bulk material. To address this concern, a detailed characterization of the thin films was undertaken using a number of surface analysis techniques. Attention has been given to an accurate characterization of the ion flux to the target as well as a detailed analysis of potential error sources. These efforts are discussed in detail in the following sections.

4.1.1 Vacuum Facility

Minimizing the arrival rate of reactive gas components to the target surface necessitated the use of an ultra-high vacuum (UHV) facility. In this case, the vacuum chamber used was capable of reaching a base pressure of approximately 1.1×10^{-7} Pa (8.0×10^{-10} torr). A schematic of the sputtering facility is shown in Figure 4.1. The stainless steel chamber measured approximately 0.6 m in length with a 0.3 m diameter, and the interior surfaces were electropolished to eliminate virtual leaks, which increase pump-down time. Two small turbo pumps initially evacuated the main chamber and differential pumping port to a pressure of 0.1 Pa (10^{-3} torr), and a 20 cm (8 in.) cryogenic pump subsequently reduced the pressure to 6.7×10^{-6} Pa (5×10^{-8} torr). The cryogenic pump also had the advantage of a large xenon pumping speed (approximately 1000 l/s), allowing a low working pressure

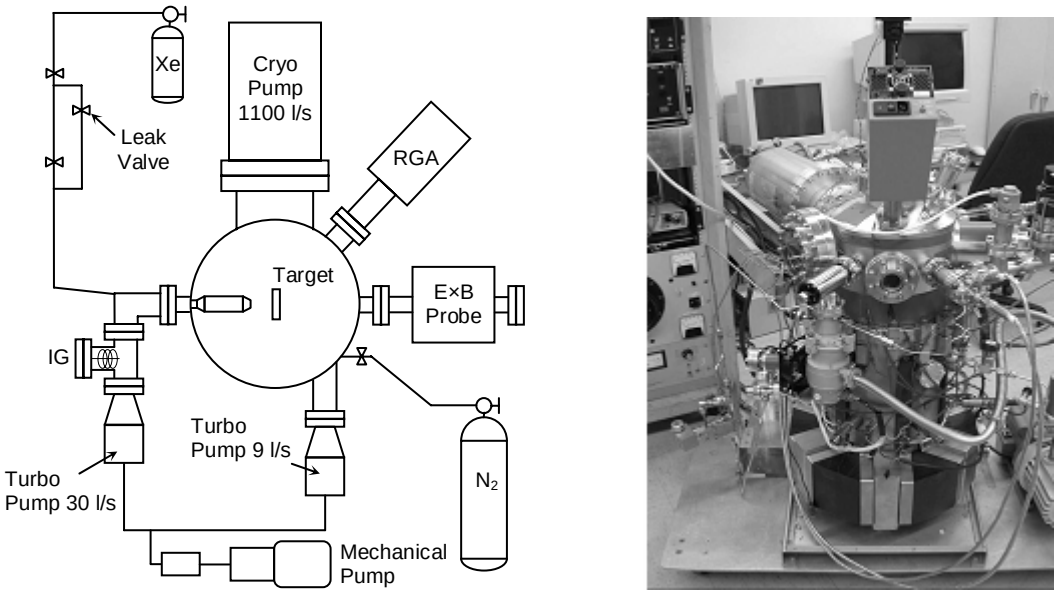

Figure 4.1: Sputtering facility schematic and photograph.

to be established during ion gun operation. An ion pump provided an additional 300 l/s of pumping speed. After a bake-out at 200 ºC for 12 hours, the final base pressure was achieved. To reduce contamination of the system, the chamber was pressurized with nitrogen gas after each set of experiments was completed.

Two ionization gauges were used to measure the pressures in the main chamber and differential pumping port. A Stanford Research residual gas analyzer (RGA) with a mass range of 200 amu characterized the background gas composition. The RGA included a channel electron multiplier, which allowed residual gas components to be detected at partial pressures as low as 1.3×10^{-9} Pa (10^{-12} torr). The most common residual gas components included CO at a partial pressure of 4×10^{-8} Pa (3×10^{-10} torr), and H_2O at 1.3×10^{-8} Pa (1×10^{-10} torr).

At a base pressure of 1.1×10^{-7} Pa, approximately 1 hour will be required for an atomic monolayer of nitrogen to form on an initially clean surface at room temperature assuming a sticking probability of 1 [Oura, 2003]. The ion source used in this study was capable of delivering a current to the target such that the ratio of ion to background gas flux was on the order of 30:1. This indicates that the

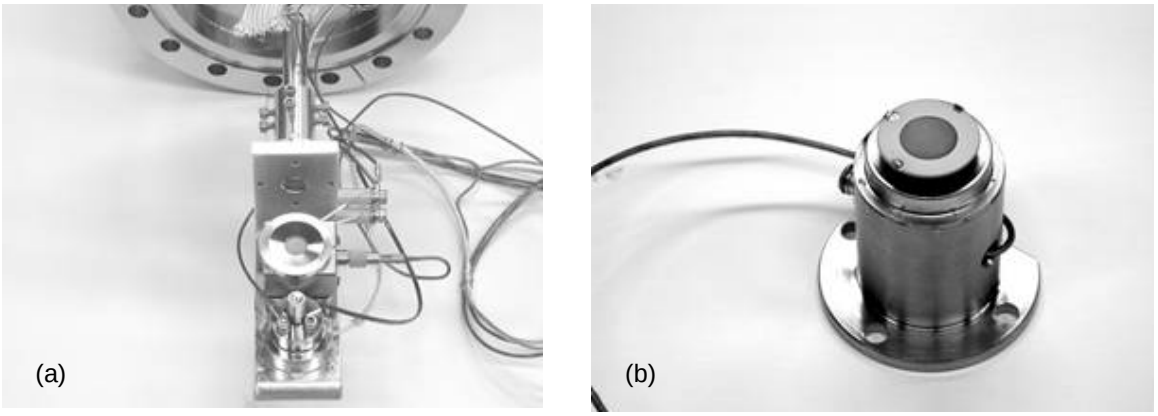

Figure 4.2: QCM holders used for (a) normal incidence and (b) glancing incidence.

vacuum conditions and ion beam strength were sufficient to not only maintain a dynamically clean surface during bombardment, but also to ensure that the target could be initially sputter cleaned for tests at lower energies.

4.1.2 QCM

Commercially available AT-cut QCMs were used throughout this investigation. When unloaded, the crystals have a resonance frequency of 6 MHz. The crystals were unpolished and were coated with a thin gold layer. Depending on the range of incidence angles being investigated, two different QCM mounting schemes were used. For θ<50º, a conventional crystal holder with a graphite shield was used with a thermoelectric cooler attached to the base, as shown in Figure 4.2a. In this configuration, the QCM could be cooled or warmed to within 0.25 ºC of the desired set point temperature using a computer controlled loop. In addition, use of the cooler allowed for rotation of the target *in situ*, which would not have been possible with liquid cooling lines.

For angles of incidence greater than 50º, the front shield of the holder began to shadow the face of the QCM. This resulted in an underestimation of the etch rate, thereby biasing the measurement of Y lower. To circumvent this problem, an alternate mounting scheme was employed for glancing incidence, as shown in Figure 4.2b. In this configuration, the crystal was bonded to three supports using a UHV rated conducting silver epoxy. The low profile of the supports allowed the beam to be

aligned almost parallel to the QCM surface. The total current to the target from the beam could be measured directly in this configuration. Since there was no way to attach a Peltier cooler to this assembly, the temperature of the sample could not be directly controlled.

4.1.3 Ion Source

An accurate determination of the bombardment conditions at the target is often a complicated process in practice. In general, the ion beam must be well defined in terms of ion energy and species, a condition often achieved by mass separating the beam [Pullins, 2000]. This involves using a series of filters to remove unwanted charge states and energies from the beam upstream of the target. For the experiments reported here, an alternate approach allows for implementation in a smaller vacuum facility. This arrangement is shown in Figure 4.3. Neutral Xe or Ar gas is admitted through a leak valve to the differential pumping port of a Kimball Physics ILG-2C low energy ion gun. The gas is ionized with a filament cathode, extracted, and focused through a series of electrostatic lenses. Near the exit aperture, a set of deflection plates rasters the beam to more evenly distribute the ion dose to the QCM target mounted approximately 40 mm downstream. This is the nominal test configuration and is indicated by case A in Figure 4.3. The incident ion current is measured with a Faraday cup mounted a fixed distance below the target. A profile of beam current density is generated by scanning the QCM/Faraday probe assembly across the beam by means of a linear translation stage. While the vacuum facility base pressure is typically 6.7×10^{-4} Pa (5×10^{-6} torr) during ion source operation, higher pressures inside the gun cause a large amount of charge exchange (CEX) ions to be generated upstream of the exit aperture. These ions are created in the same manner previously discussed for the thruster grids. The Faraday probe traces allow only the total *charge* incident on the target to be measured; additional techniques are necessary to account for high energy neutrals formed in CEX reactions. A second set of deflection plates just downstream of the gun exit is used to deflect ions away from the QCM, as shown in case B. CEX neutrals are unaffected by this process, and the QCM is used to measure the erosion from this species *in situ*. The QCM and Faraday cup can be

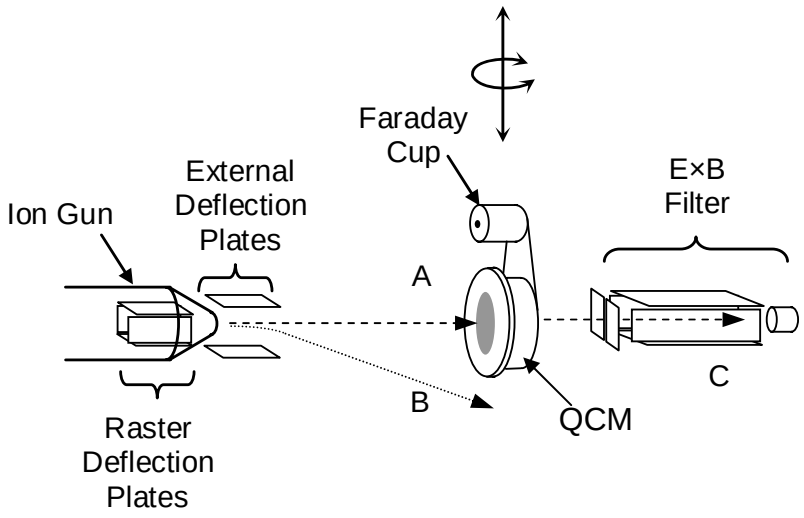

Figure 4.3: Ion beam diagnostics.

retracted completely to allow the beam to pass into an E×B probe. Located just downstream of the target, this instrument characterizes the double ion content of the beam. Because double ions cannot be separated upstream of the target, the discharge parameters of the gun are adjusted to minimize the quantity of Xe^{2+} and Ar^{2+} present.

Cross sections for Xe^{+}-Xe charge exchange collisions have recently been measured using two techniques [Pullins, 2000] and are shown in Figure 4.4. Data from both time of flight (TOF) and

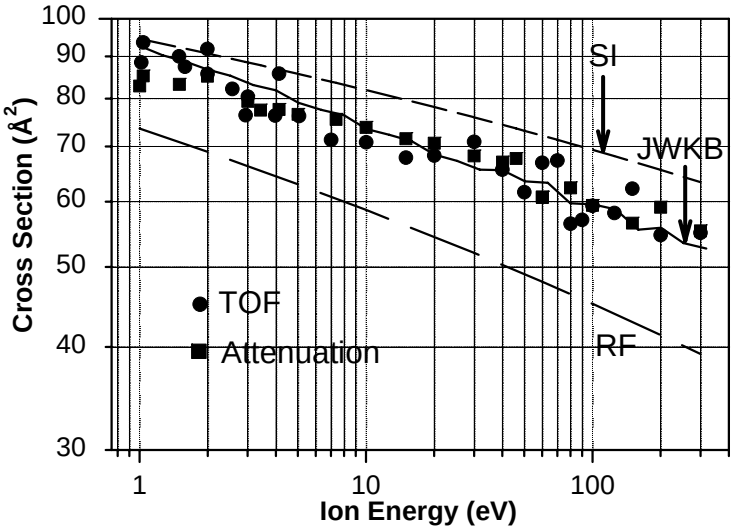

Figure 4.4: Cross sections for Xe^{+}-Xe collisions [Pullins (2000)].

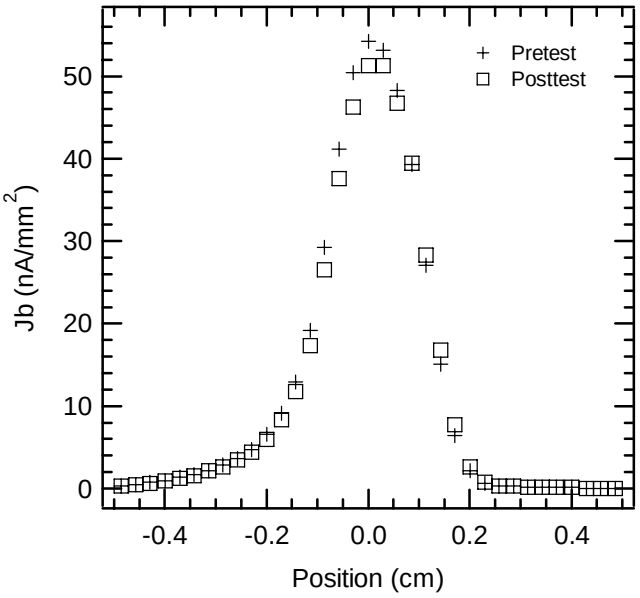

Figure 4.5: Pretest and posttest beam current density profiles for 300 eV Xe^+ ions.

attenuation measurements are compared with existing cross section calculations in this reference. Based on these data, one would expect the fraction of the beam composed of CEX neutrals to be larger at lower energies, given the larger cross sections. In addition, the CEX ion production rate would be expected to increase at higher pressures and current densities because more collision opportunities exist under these conditions. Figure 4.4 depicts predictions from cross section models developed by Rapp and Francis (1962, denoted RF) and Sakabe and Izawa (1991, denoted SI).

An impinging high energy ion beam causes the ejection of secondary electrons from a surface, which makes ion beam current measurements problematic. Emitted secondary electron current cannot be distinguished from arriving ion current. The Faraday probe used in this study was designed to minimize this effect. The current collecting cup was fabricated from molybdenum, which has a low secondary electron emission coefficient. To prevent the escape of secondary electrons, a high aspect ratio geometry for the collector cup was used (approximately 4:1). The collector was housed within a 6.35 mm (0.25 in) diameter stainless steel shield. The shield was biased 18 V below ground potential to repel electrons created by other instruments in the vacuum facility and to provide an additional potential barrier for the escape of emitted secondary electrons within the probe.

Table 4.1: Ion beam current density and FWHM for the operating conditions of this work.

Ion Energy, eV	Maximum j_b, nA/mm^2	FWHM, mm
1000	41.03	2.74
700	40.56	3.39
600	46.21	3.47
500	33.27	3.97
400	27.61	3.69
300	52.61	2.10
250	92.58	1.47
200	76.13	1.92
150	47.79	2.00
100	34.22	2.52
80	23.80	3.21

The small diameter of the ion beam (5-6 mm) introduced a number of challenges for accurate current measurement and probe alignment. The size of the Faraday probe shield's knife edge aperture was chosen to be 0.9 mm based on the need to balance signal strength with resolution. The narrow beam width also demanded precise probe and target positioning. Using welded bellows segments in the alignment fixture allowed the sample to be rotated and translated along one axis and small adjustments to be made along the other two axes. A micrometer gimbal was attached to the lower bellows while the upper bellows was attached to a linear translation stage equipped with a stepper motor.

The ion source operating parameters were selected to maximize the ion current to the target while minimizing the double ion fraction and maintaining an axisymmetric beam. A typical beam current density profile is shown in Figure 4.5. Measurements taken approximately 1 hour apart are overlaid to illustrate the beam current drift experienced during a typical test run. Table 4.1 gives specific beam current density profile characteristics, including the maximum j_b as well as the full width at half maximum (FWHM).

Although a series of electrostatic lenses within the ion source allowed some control over the focusing of the beam, rastering was used as a means of creating a more uniform dose over the target

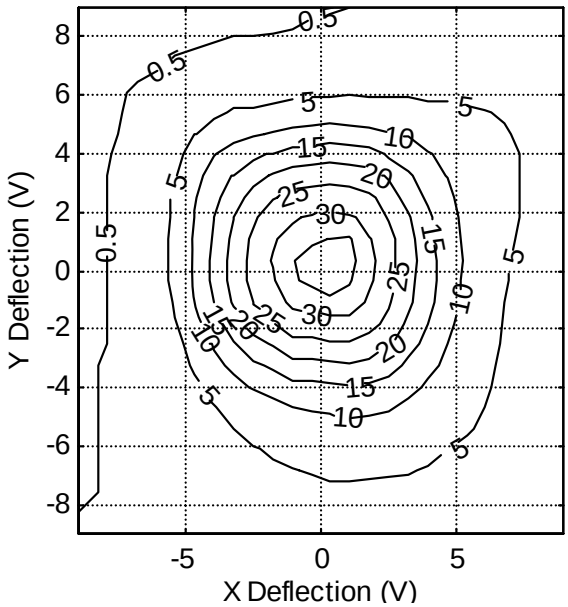

Figure 4.6: Constant current lines (nA) for a 300 eV Xe^+ ion beam mapped as a function of deflection voltage.

surface. This was accomplished by applying a saw-tooth voltage function to a set of deflection plates near the exit of the ion source using a function generator. A high frequency voltage signal allowed the ion beam to be swept rapidly in the x-direction, while a lower frequency was used to more gradually sweep the beam in the y-direction. This created a rectangular pattern over the target surface that changed with time (the periods of the x and y scans were not synchronized.) The sweep frequencies were much larger than the response of the picoammeter used to measure the current signal picked up by the probe. As is evident from Table 4.1, for the ion energies used in this study, the peak beam current density ranged from 23-92 nA/mm^2. With rastering, the beam diameter based on the full width at half maximum (FWHM) could be varied between 1.4-4 mm.

In this study, the ion beam was assumed to be axisymmetric and the j_b profiles measured with the Faraday probe along one axis were used for calculations of the sputtering yields. To verify beam axisymmetry, the probe was centered on the beam at the point of maximum current density and then the beam was deflected in a grid-like pattern over the probe using the raster deflection plates, effectively creating a 2-D map. At high voltages the deflection distorts the profile (making it

inadequate for use as a quantitative measurement). However, qualitative information on beam axisymmetry is obtained from this method and may be used to determine how representative the j_b profile is of the overall beam. The beam map displayed in Figure 4.6 was taken during the same test as the j_b profiles displayed by Figure 4.5.

An E×B probe accounted for double ions and other impurities in the beam. The same probe originally constructed for a previous study by Duchemin (1999) was also employed here. A sample probe trace for the 1 keV ion beam used in this investigation is shown in Figure 4.7. Note that 2 peaks are present at different collection plate voltages, corresponding to different charge states of the xenon ion species. The Xe^+ peak is the larger peak, (a smaller deflection voltage is required to bend the singly charged ions into the collector cup.) The ratio of the peak heights gives the ratio of Xe^{2+} to Xe^+ current, J^{2+}/J^+. As shown in Figure 4.7, the double ion fraction in the beam could be minimized to negligible levels by lowering the ion source discharge voltage as much as possible. Probe measurements verified that for the 40 V discharge used in the present work, the ratio of Xe^{2+} to Xe^+ was less than 4×10^{-4}, as indicated in Table 4.2.

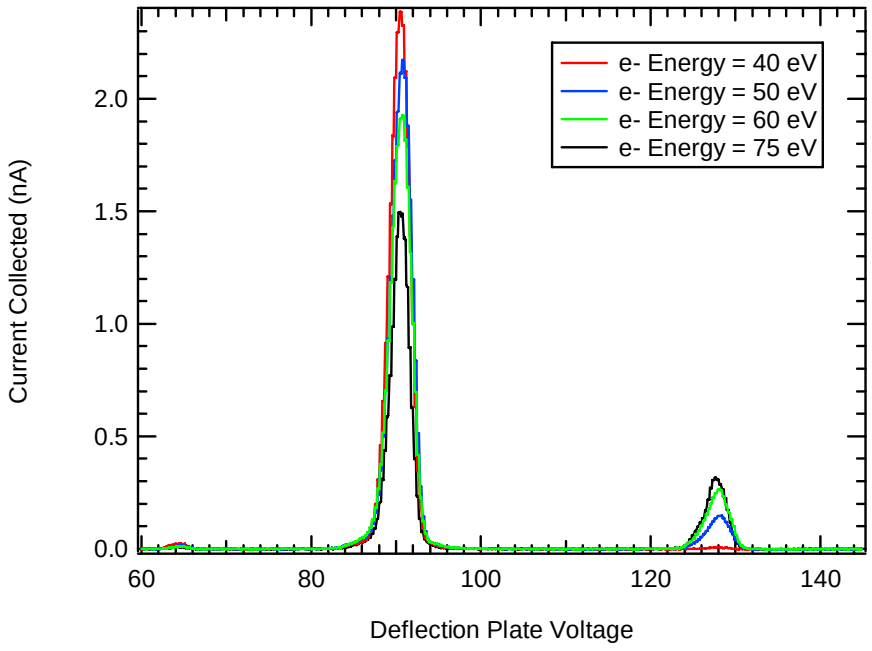

Figure 4.7: E×B probe traces for varying discharge voltages.

Table 4.2: Double ion content as a function of discharge voltage.

Discharge voltage, V	J^{2+}/J^{+}	n^{++}/n^{+}
75	0.225	0.080
60	0.137	0.049
50	0.070	0.025
40	0.001	0.0004

4.2 Target Characterization

Initially, three metallic target materials (Mo, Cu, and W) were investigated and deposited on QCMs in the form of thin films. The molybdenum coatings were deposited using a magnetron sputtering process developed by Duchemin (1999). The thicknesses of these coatings were determined through profilometry and found to be 3.5 μm. The copper and tungsten films were also generated by magnetron sputtering and were coated to thicknesses of 9.0 μm and 5.0 μm, respectively. The parameters for these depositions are given in Table 4.3.

Table 4.3: Cu and W film deposition parameters.

Deposition rate:	110 Å/min
Working gas:	Argon
Pressure:	1.3 Pa
Bias voltage:	0 V

In practical applications, bulk materials are the sputtering targets, so the physical properties of the coatings used in this experiment should be representative of the bulk material. Two techniques have been employed to examine the film properties in detail, including scanning electron microscope (SEM) imagery and x-ray diffraction. Because of its use in electric propulsion for sputter-resistant components, the Mo films were of primary interest here, and the Cu and W coatings were not characterized as extensively. The SEM and x-ray diffraction analysis results are presented for the Mo films only.

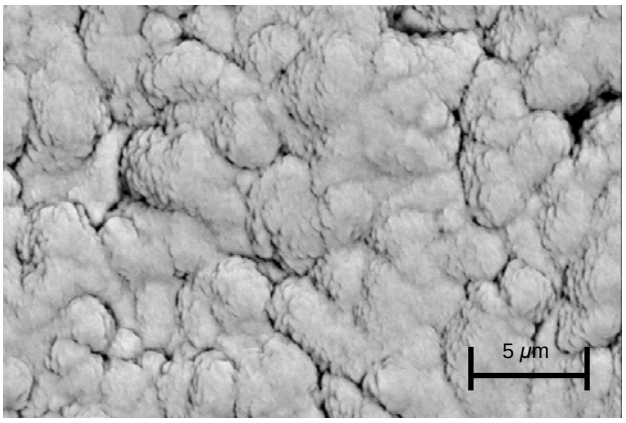

Figure 4.8: SEM image revealing the surface topography of a Mo film.

4.2.1 SEM

A scanning electron microscope provided insight into the surface topography and chemical composition of the deposited films. Figure 4.8 displays the surface, whereas Figure 4.9 shows a cross section of a crystal broken in liquid nitrogen. In both cases, the film was imaged using electrons backscattered from the sample. The images reveal that the surface is significantly textured with visible clusters of crystals between 3 and 5 microns in length. The 3.5 μm thick layer of molybdenum can be seen deposited on the gold coated quartz crystal in the cross section image. (The gold layer is approximately 200 nm thick.) The grain structure appears to be roughly columnar and discontinuities in the film appear to coincide with surface irregularities in the quartz substrate. To generate smoother surface textures, several microns of a substrate material (such as aluminum) could be deposited on the quartz surface and polished with 1 μm diamond paste.

The SEM analysis also allowed impurities in the coating surface to be detected. While not the most precise means of accomplishing this, the SEM does allow qualitative verification that impurity levels are in fact small. For the coatings discussed here, no traces of substances other than Mo were detected. Images from the SEM also did not reveal any large concentrations of impurities, suggesting that any impurities were scattered diffusely throughout the coating and were not present in quantities above the detection threshold of the SEM.

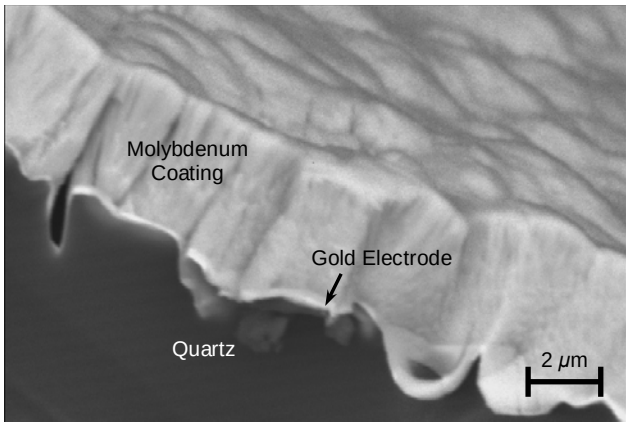

Figure 4.9: SEM image of a cross section of a crystal fractured in liquid nitrogen.

4.2.2 X-Ray Diffraction

The crystal structure of the target has been shown to influence the measured sputtering yields. The effect of angle of incidence on single crystal structures is particularly dramatic, as certain angles allow significant channeling into the surface, thereby reducing the sputtering yield [Roosendaal, 1981]. Given the potential influence of crystal structure, the lattice parameters and the density of the deposited thin films were calculated using x-ray diffractometer measurements.

The general technique involves placing a sample (in the form of a flat plate) in a fixture at an angle γ with respect to a collimated x-ray source. The x-rays are scattered off the target and pass through a set of slits into a scintillation detector located at an angle 2γ. The fringe pattern created by reflections from different planes in the crystal structure of the material is determined by the following expression:

$$\frac{\sin^2 \gamma}{(h^2 + k^2 + l^2)} = \frac{\lambda^2}{4a^2} \qquad \textbf{4.1}$$

The value of $\lambda^2/4a^2$ is constant for any pattern, and, as a result, the size of the unit cell determines the angular position of the diffraction lines according to the above relationship. The integers *h, k,* and *l* are the Miller indices of a particular crystal plane within the material. For a specific crystal structure,

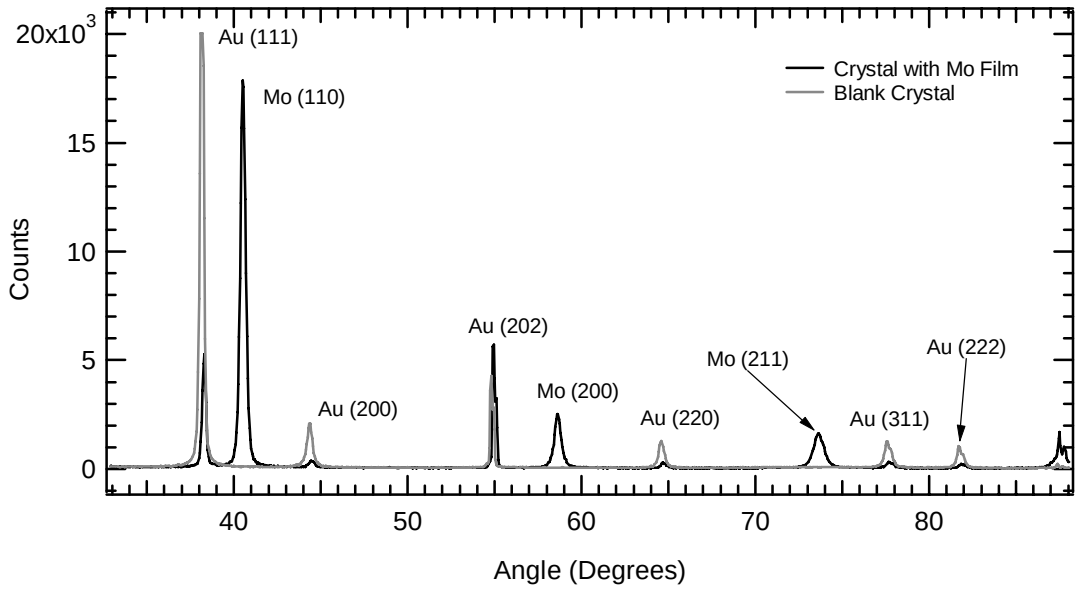

Figure 4.10: X-ray diffraction scans of Mo-coated and blank QCMs.

only certain combinations of these integers will result in a diffraction peak in the resulting spectrum [Cullity, 1959].

Interpretation of the diffraction data reported here is complicated by the presence of peaks from both the Au electrode and the Mo film. Scans of both a blank and a molybdenum-coated QCM were taken and are displayed in Figure 4.10. In the scan of the crystal blank, only the Au peaks are visible and display a pattern characteristic of a face centered cubic (FCC) crystal structure. In the scan of the coated crystal, three additional peaks corresponding to the Mo layer appear. Their spacing indicates a body centered cubic (BCC) structure, the same as bulk molybdenum. The peaks corresponding to each element are labeled in Figure 4.10 along with the Miller indices of the crystal plane responsible for each reflection.

The atomic spacing may be calculated directly from the diffraction scan. The copper electrode x-ray tube used in this study had a characteristic radiation wavelength of $\lambda = 1.54178$ Å. Based on this wavelength and the location of the peaks, the atomic spacing in the film was calculated to be 3.149 Å,

less than 0.08% larger than the bulk material. This would correspond to a coating density of ρ_E = 10.20 g/cm^3, less than 0.3% lower than the bulk value.

4.2.3 Summary

The observations from the SEM and x-ray diffraction analysis support the conclusion that the thin films are a reasonable approximation to the bulk materials. The coatings have the same crystal structure as the bulk material, and the interatomic spacing indicated by the x-ray diffraction measurements indicates a comparable film density. The SEM analysis shows low levels of impurities in the deposited films as well. The coatings appear to be composed of columnar grains, which are smaller than the average bulk material size. However, since the grain diameters of polycrystalline metals are still small compared with the irradiation area, one would expect this difference to have a very minor effect on the sputtering behavior.

4.3 Experimental Procedure

Each crystal used was cleaned with chemical solvents and rinsed with alcohol and deionized water prior to inserting it into the experimental facility. Once the desired facility base pressure had been achieved, gas was admitted to the differential pumping port of the ion gun. The typical operating pressure of this device was on the order of 2.6×10^{-2} Pa (2×10^{-4} torr). A 3 hour stabilization period was allowed after the gun was activated.

The Faraday probe was centered on the beam by adjusting its position with the micrometer gimbal stage and stepper motor until the current measured by the probe was maximized. A beam map was taken to confirm that the rastering created an axisymmetric beam current distribution. Once the probe alignment was completed, a beam current density profile was taken, and the QCM was moved into the beam. The sample temperature, differential pumping port pressure, and QCM monitor output were recorded with a computer-based data acquisition system. In each case, the sample was etched to

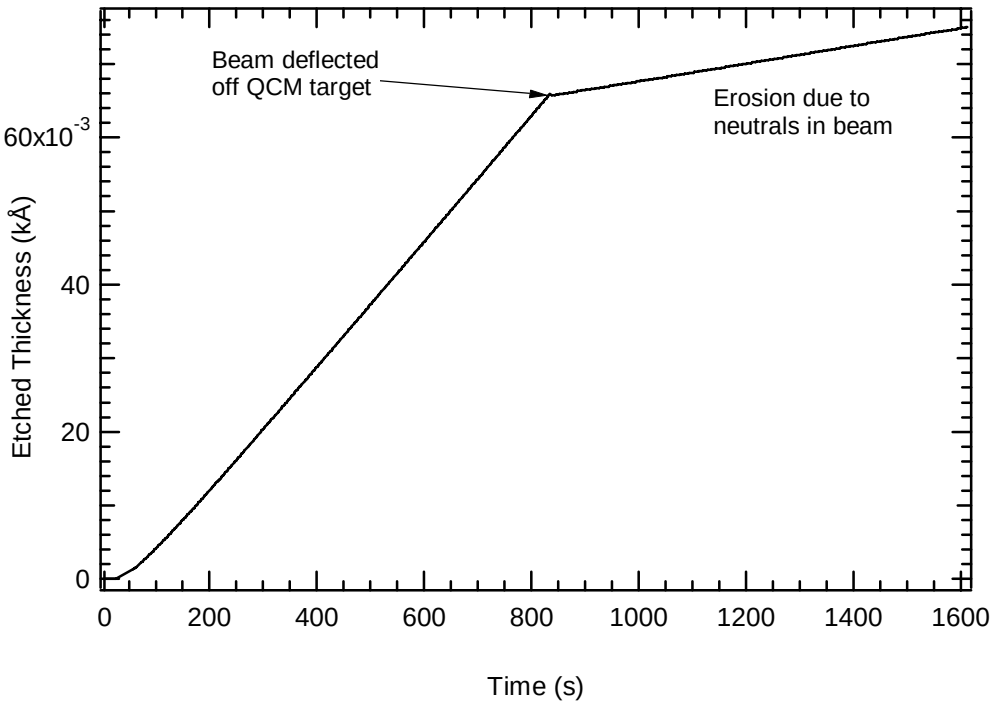

Figure 4.11: Measured Mo film thickness change during bombardment by 1 keV Xe^+ ions.

a depth of at least 40 Å, after which the ion beam was deflected completely off of the crystal surface to measure the sputter rate contribution from energetic neutrals.

The output from the thickness monitor for the case of 1 keV Xe^+ ions incident on Mo is shown in Figure 4.11. The total etch rate is the initial slope, which is simply the superposition of the effects of the ions and neutrals incident on the surface of the QCM. The etch rate due to neutrals is measured by the QCM *in situ* and subtracted from the total erosion rate to obtain the contribution of the ions only.

For measurements with bombarding energies of less than 200 eV, it was possible for the residual gas components in the facility to form a protective layer on the QCM surface that could not be destroyed by the low energy ions. For these cases, the surface was sputter cleaned at 1 keV immediately prior to etching. The effect of this phenomenon on the measurements is further discussed in Section 4.6. In addition, for measurements at different angles of incidence, the surface

was preconditioned by etching at normal incidence to a depth of 80 Å. This ensured that the surface topography of the sample was the same for all measurements.

Even though numerous steps had been taken to ensure the stable operation of the ion source, a small amount of drift (typically 5% or less) in the current output was unavoidable. To characterize the magnitude of this variation and its effect on the sputtering yield measurement, a second j_b profile was taken at the conclusion of each test. For measurements taken at normal incidence and for θ<45º, this was the only method of determining the total drift. In the sputtering yield calculations, a monotonic variation between the pretest and posttest profile was assumed. The QCM mount used for glancing incidence measurements allowed the total current to the target to be monitored continuously throughout the etching process. During these tests, the j_b variation appeared to be coupled with ambient temperature variations. Because the test duration was short compared to the temperature drift time scale, the j_b variations were monotonic, validating the assumption used in the near-normal incidence measurements.

As previously mentioned, a major advantage of this technique is the large number of measurements that can be taken in a short period of time. Typically, five test runs at 1 keV can be conducted during a single day of operation. As one might expect, the testing time required at lower energies is substantially longer. A single 80 eV molybdenum test requires nearly 17 hours to complete.

4.4 Data Analysis

The indicated thickness change represents an average over the entire QCM surface. Because the removal of mass from the target surface was not uniform, a correction was necessary to account for the variations in QCM sensitivity as a function of radius r and polar angle φ. An analytical function for this sensitivity c_f was derived by Cumpson and Seah (1990):

$$c_f(r,\varphi) = c_o \exp[-r^2(\alpha_1 \cos^2\varphi + \beta_1 \sin^2\varphi)] \qquad \textbf{4.2}$$

The constants α_1, β_1, and c_o depend on the material properties of quartz as well as the crystal geometry according to

$$\alpha_1^2 = \frac{\pi^2 \overline{C}_{66}}{8Rh_0^3 M_1}\left(1 - \frac{8k_{26}^2}{\pi^2} - \frac{2\rho_E h_E}{\rho_Q h_0}\right)$$
$$\beta_1^2 = \frac{\pi^2 \overline{C}_{66}}{8Rh_0^3 C_{55}}\left(1 - \frac{8k_{26}^2}{\pi^2} - \frac{2\rho_E h_E}{\rho_Q h_0}\right) \qquad \textbf{4.3}$$

In the above expressions, C_{55}, C_{66}, M_1, and k_{26} are elastic constants of quartz; h_o and R are the half-thickness and radius of curvature of the QCM; and ρ_Q is the density of quartz. Numerical values of these constants have been previously published [Cumpson, 1990; Duchemin, 1999]. The film thickness and density are denoted ρ_E and h_E. At first glance, the dependence of the sensitivity function on φ appears counterintuitive, given the circular geometry of the quartz resonator. However, the material properties of the quartz itself are anisotropic ($\alpha_1 \neq \beta_1$). The dependence of the response function on φ is not strong. Lines of constant c_f would form a set of ellipses with the major axis being approximately 12.5% longer than the minor axis and oriented along the x-direction.

Duchemin (1999) pointed out in previous work the benefits of using the higher sensitivity of the QCM near the center of the electrode and developed a method of applying the expression for c_f to sputtering calculations. In particular, if the beam current density profile $j_b(r)$ is known, the sputtering yield may be determined by

$$Y = \frac{\Delta\tau_{meas} Nq \int_0^a \int_0^{2\pi} c_f(r,\varphi) r dr d\varphi}{\Delta t \int_0^a \int_0^{2\pi} c_f(r,\varphi) j_b(r) r dr d\varphi} \qquad \textbf{4.4}$$

Note that $\Delta\tau_{meas}$ is the average thickness change calculated from the measured resonance frequency shift of the QCM, and Δt is the time interval over which the test occurred. As before, N refers to the target number density and q is the elementary charge. The above expression works well at normal incidence, when the ion dose forms a circular pattern independent of φ on the target. For any off-

normal angle θ, the beam projects an ellipse on the target surface. In this situation, j_b becomes a function of r and φ, with the major axis having been stretched by a factor of $1/\cos\theta$. The Faraday probe measures the current density profile along a single axis at normal incidence. To modify this profile for cases where the target is angled with respect to the beam, a simple geometrical correction is used. In addition, because the beam is projected over a larger area, the current density decreases. Hence, at glancing angles, measurements are more susceptible to error due to lower current densities.

The Faraday probe averages the measured ion beam current over the entire aperture. Because the aperture size is appreciable compared to the beam diameter, a slight (but not negligible) distortion of the j_b profile occurs. Retrieving the original profile based upon the measured data is not a trivial process. Averaging necessarily implies a loss of information over the measurement area of the probe and there is no unique inverse for this type of transformation. Given these difficulties, assumptions regarding the shape of the original profile are necessary. In this case, it is assumed that the distortion of the profile due to the probe is small, and that the non-averaged profile may be obtained by a linear transformation of the measured profile. An iterative scheme was employed to calculate the mapping parameters.

Figure 4.12 displays a demonstration of this technique. The original j_b profile is simulated by a continuous 2-D Gaussian distribution. The profile width has been selected to be similar to that produced by the ion gun. Calculating the current density over a 0.9 mm diameter aperture at discrete positions along one axis of the distribution, a simulated "measured profile" is generated. This displays how the original profile is distorted by the probe, underestimating j_b at the peak by 5%. The profile is adjusted through a constant multiple to obtain a "corrected profile." This parameter is adjusted though an iterative scheme to obtain the corrected profile that most closely approximates the measurement when averaged. Emphasis is placed on minimizing the errors closest to the center of the QCM. For the specific test case discussed above, the corrected profile is displayed in Figure 4.12.

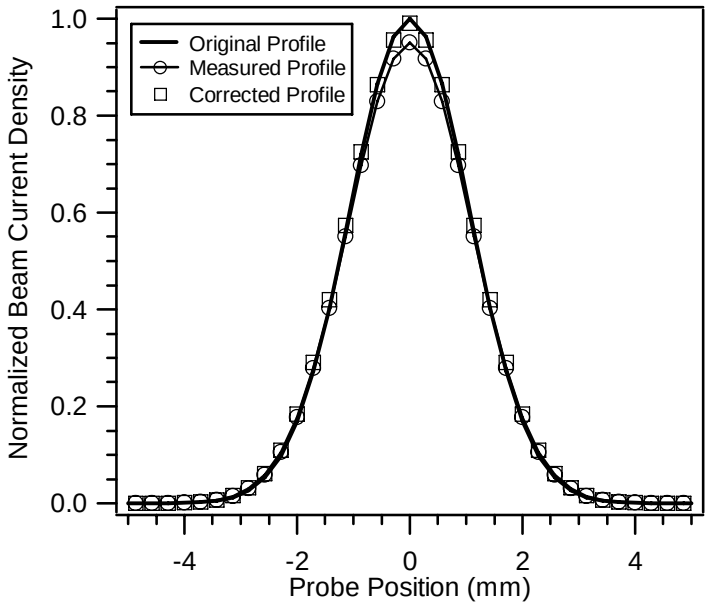

Figure 4.12: Beam current density profile showing errors caused by probe averaging.

4.5 Error Analysis

The error of the sputtering yield measurements in this work depends to a significant degree on the how accurately the beam current profile has been measured. To better ascertain the effectiveness of the j_b profile corrections discussed in the previous section, the QCM was replaced with a carbon disc mounted in the target holder. The disc was isolated from the holder with a thin Nomex ring and connected to ground through a picoammeter. The total current to the target was compared with the integrated profile over the QCM surface. In cases where the rastering amplitudes were adjusted to create an axisymmetric beam, measured beam current typically agreed with the total integrated current to within 4%. For cases where the beam was not axisymmetric, the two measurements differed by 10% or more.

The two raster frequencies (500 Hz and 10 Hz) were higher than the picoammeter response time. As a result, the instrument provided an averaged current output. To verify that the filtering process was not improperly biasing the results, a digital oscilloscope was used to capture the signal from the

Faraday cup collector over several raster sequences. The average current value measured by the oscilloscope agreed to within 1-2% of the picoammeter output.

Despite efforts to minimize ion current drift, some small transient effects were unavoidable during etching. The stability of the ion source depended mainly on pressure variations in the differential pumping port and on ambient temperature conditions and can be inferred from beam current density profiles before and after each test run as well as from changes in the sputtering rate. The difference in the yield using both the pretest and posttest profiles was calculated to assess the total contribution from this error source. In most cases, the yields calculated from both profiles differed by less than 5%. In the test configuration for glancing angle measurements, the ion current to the target was measured directly. As expected, transient effects were typically more severe for the longer, lower energy tests.

The QCM positioning uncertainty also contributed to the error. A 0.2 mm initial alignment uncertainty was assumed for all measurements in this study, corresponding to the step size used in the Faraday probe scans. For measurements where the target was angled with respect to the beam, a ±0.25º uncertainty in the incidence angle was assumed based on the resolution of the rotary positioning stage.

Temperature changes cause drift in the QCM resonance frequency and introduce systematic errors in the measurements. However, because the ion beam used in this experiment only produced a small dose to the target surface, in most cases the frequency drift was dominated more by ambient temperature changes than from beam heating. The shift in resonance frequency was calculated using curves published by EerNisse (1975). During most short duration tests, the thermoelectric cooler regulated the target temperature to within ±0.2 ºC, and to within ±2.0 ºC for the longer, lower energy tests. For the glancing angle measurements, the QCM mounting scheme did not allow for the use of a Peltier cooler to regulate the target temperature. The most severe temperature drift experienced with this configuration was less than 2 ºC.

The presence of double ions or other impurities in the beam could also potentially bias the results. As previously discussed, the ion source operating parameters were selected to minimize the fraction of double ions in the beam. For a 40 V discharge, less than 0.04% of the ions in the beam were Xe^{2+}. Assuming this ratio for an 80 eV ion beam (which represents the worst case), the measured sputtering yield would be biased less than 0.3% high by the presence of double ions.

Using standard error propagation methods, the error analysis suggests that, on average, sputtering yields measured in this paper could be considered accurate to within 5% to 6% at higher energies and between 6% to 10% at lower energies.

4.6 Results

As an initial step in validating the experimental setup, the normal incidence sputtering yields measured in this work were compared with other published values. As previously mentioned, the ion-target combinations investigated in this study were $Xe^{+}\rightarrow$Mo, $Ar^{+}\rightarrow$Cu, and $Ar^{+}\rightarrow$W. These measurements of normal incidence yields are given in Table 4.4 for an energy range of 80-1000 eV. Figure 4.13 and Figure 4.14 provide a comparison with previously published data. An empirical fit to these data developed by Matsunami, et al. (1984) for normal incidence sputtering yields is also included for comparison. The Matsunami empirical curve fit slightly underpredicts the trend displayed by most of the published results. It should be noted that this source provides generalized curves designed to fit numerous projectile/target combinations over a wide range of energies and does not necessarily provide a best fit for the specific conditions of interest here. A small adjustment to the curves suggested by Seah (2005) for noble gases eliminates this discrepancy.

Also included in the molybdenum data set are yield measurements taken without prior sputter cleaning of the target surface from 80 eV to 200 eV. At low energies, initial sputter cleaning using a higher energy beam had a significant impact on the measured sputtering yield. The inability of the low energy beam to completely remove absorbed monolayers of surface contaminants resulted in a non-negligible level of contaminant coverage. This effect became less pronounced at higher energies,

until it was negligible above 200 eV. Below 80 eV, a clean surface could not be maintained even with prior high energy sputter etching. In addition, the CEX cross sections for Xe and Ar become larger at lower energies, and at 80 eV fast-moving neutrals created by charge exchange account for more than 90% of the energetic particle flux to the target surface. Distinguishing this effect from erosion from ions becomes increasingly difficult at low energies. The combination of these two effects suggests that the low energy limit of the present experimental setup is approximately 80 eV.

The $Ar^+ \rightarrow Cu$ and $Ar^+ \rightarrow W$ measurements reported here agree well with previously published normal incidence data. At higher energies, the $Xe^+ \rightarrow Mo$ data are 5% higher than the mid-range of the literature values and are within the scatter between measurements from different laboratories.

With the accuracy of the experiment established for normal incidence, the dependence of the yields on angle of incidence was then examined for 1000 eV, 500 eV, and 300 eV Xe^+ incident on Mo. The yields for incidence angles between 0º and 80º are given in Table 4.5 and Figure 4.15. The $\cos(\theta)^{-f}$ dependence predicted by Sigmund (1969) is also included in Figure 4.15 with the suggested value of f=5/3 for each energy. The model is anchored to the measured sputtering yield at θ=0°. For several cases, multiple values for Y are included to establish the measurement repeatability and to validate the error analysis.

The dependence of Y on angle of incidence appears to conform to the expected behavior. From Figure 4.15, the rate of increase in Y with θ agrees well with that predicted by Eqn. 1 up to 40º to 45º. A drop-off in this rate is evident until a maximum is achieved between 50º to 55º. The yields decrease thereafter, with $Y(\theta_{max})/Y(0)$ between 1.6 and 1.8.

The optimum sputtering angle observed in this study appears at a lower value of θ than previously reported values at higher energies and lighter atoms. Such differences are not unexpected, however, given that the penetration depth of the projectile atom will be much greater in the higher energy case. At lower energies, the projectile remains closer to the surface and is scattered from its original trajectory more easily. Hence, one would expect lower energy yields to be less sensitive to angle of incidence.

Table 4.4: Normal incidence yield measurements, from the present work.

Energy (eV)	Y (atoms/ion)		
	$Xe^+ \rightarrow Mo$	$Ar^+ \rightarrow Cu$	$Ar^+ \rightarrow W$
1000	1.73±0.07	3.35±0.15	···
700	1.25±0.07	···	···
600	1.12±0.05	···	0.648±0.069
500	0.890±0.043	···	···
400	0.754±0.042	1.85±0.08	0.545±0.026
300	0.550±0.022	1.50±0.08	0.475±0.031
250	0.431±0.026	···	···
200	0.314±0.015	0.961±0.045	0.269±0.037
150	$0.184^{+0.012}_{-0.019}$	···	···
100	$0.064^{+0.003}_{-0.004}$	$0.370^{+0.020}_{-0.021}$	0.070±0.009
80	$0.023^{+0.001}_{-0.002}$	0.238±0.012	0.026±0.003

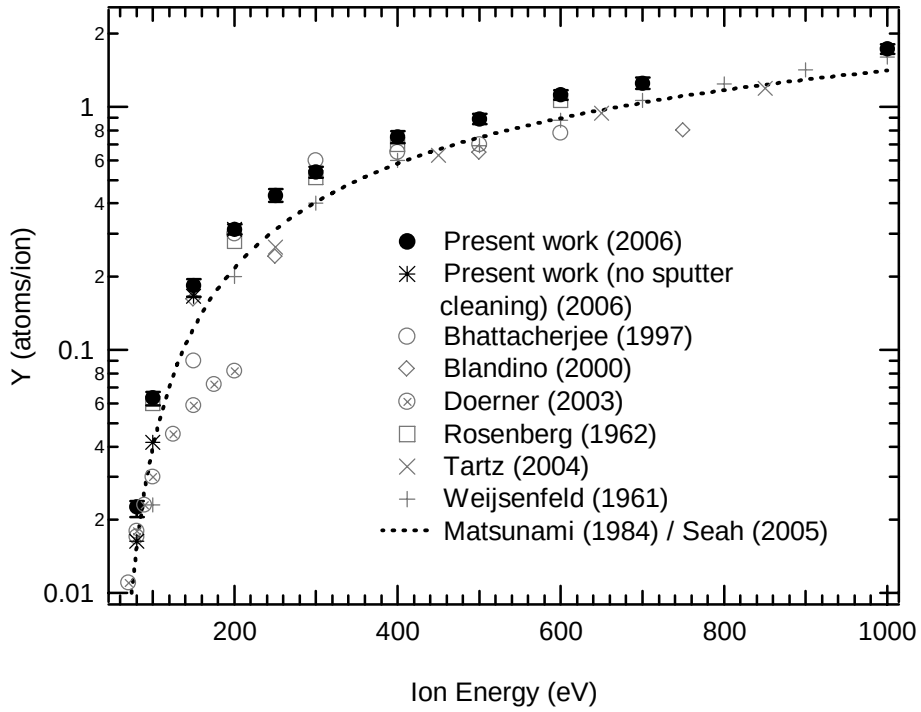

Figure 4.13: $Xe^+ \rightarrow$ Mo normal incidence sputtering yield measurements obtained in the present study for 80 eV to 1000 eV. Previous experimental data and empirical curve fits are included for comparison.

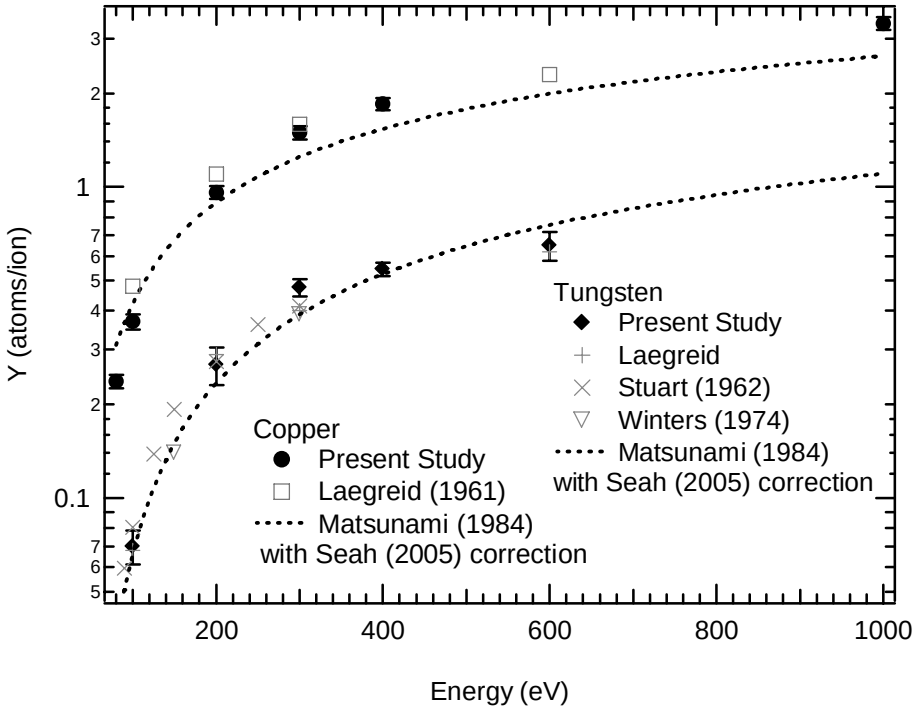

Figure 4.14: Cu and W sputtering yield measurements obtained in the present study for Ar^+ ions at normal incidence. Prior experimental data and empirical formulas included from other sources, as indicated.

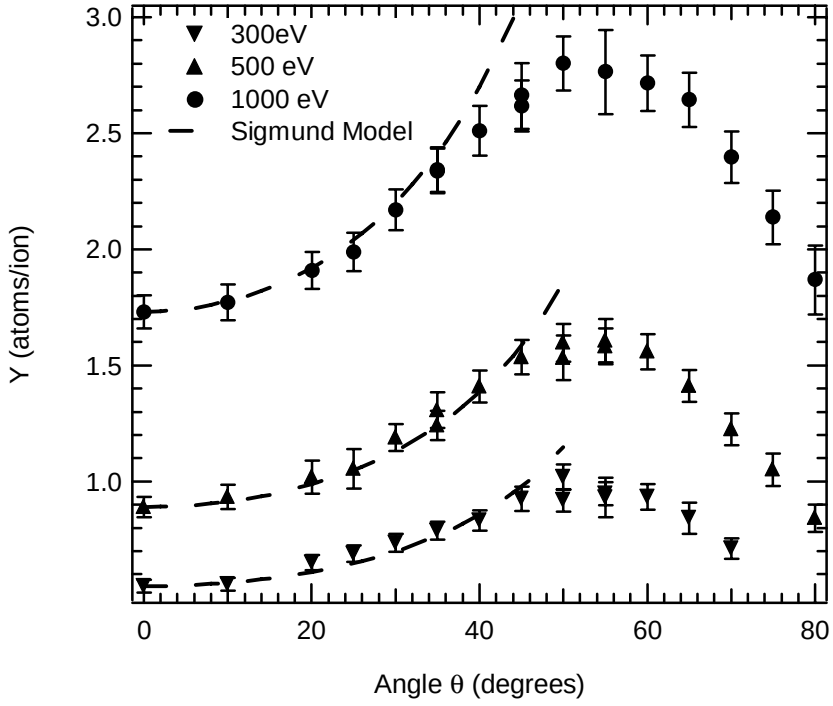

Figure 4.15: Sputtering yield variation for $Xe^+ \rightarrow$ Mo as a function of angle of incidence. All data from present work. Theoretical prediction from Sigmund (1969) included for comparison.

Table 4.5: Experimental data from present work showing the angular dependence of $Xe^+ \rightarrow Mo$ sputtering yields.

θ	Y, (atoms/ion)		
(deg.)	300 eV	500 eV	1 keV
0	0.550±0.022	0.890±0.043	1.73±0.07
10	0.556±0.023	0.934±0.052	1.77±0.08
20	0.651±0.027	1.02±0.07	1.91±0.08
25	0.688±0.029	1.06±0.08	1.99±0.08
30	0.736±0.032	1.19±0.06	2.17±0.09
35	0.789±0.032	1.24±0.06 $1.31^{+0.076}_{-0.078}$	2.34±0.10 2.34±0.10
40	0.831±0.036	1.41±0.07	2.51±0.11
45	0.926±0.045	1.53±0.10	2.62±0.11 2.66±0.14
50	0.920±0.040 1.02±0.06	1.53±0.09 1.60±0.08	2.80±0.12
55	0.948±0.041 0.931±0.084	1.61±0.09 1.58±0.08	2.77±0.18
60	0.934±0.056	1.56±0.08	2.72±0.12
65	$0.842^{+0.066}_{-0.068}$	1.41±0.07	2.64±0.12
70	0.711±0.043	1.22±0.07	2.39±0.11
75	···	1.05±0.07	2.14±0.12
80	···	$0.842^{+0.058}_{-0.061}$	1.87±0.15

4.7 Concluding Remarks

An experimental apparatus was developed to measure low energy sputtering yields at glancing incidence. A Faraday cup characterized the ion dose to the target, and an E×B probe quantified the presence of unwanted species in the beam. An *in situ* measurement of the erosion rate due to energetic neutrals was made by electrostatically deflecting the ions away from the target and subsequently recording the etch rate. Accounting for the radial mass dependence of the QCM allowed a narrow beam to be used. The target thin films were found to be an acceptable approximation to their respective bulk materials using a number of surface analysis techniques.

Yield measurements for Mo, Cu, and W targets over an 80 eV to 1000 eV energy range were found to be in satisfactory agreement with published data. Both Xe and Ar ion beams were used for bombardment. For θ ranging between 0º and 80º, yields for Mo were measured for Xe^+ energies of 300 eV, 500 eV, and 1 keV. An optimum sputtering angle occurred at 50º to 55º for these conditions,

with $Y(\theta_{max})/Y(0)$ ranging from 1.6 to 1.8. The variation in Y agreed well with the $\cos^{-f}(\theta)$ dependence predicted by Sigmund (1969) for angles less than 45º.

The high sensitivity of the QCM lends itself well to sputtering measurements, allowing etch rates to be measured *in situ*. The method offers the ability to generate a substantial yield database in a relatively short period of time. With minimal modification, this technique can be applied to a variety of other materials with the restriction that they must be deposited as a thin film at low temperature. How closely these thin films resemble the materials they are intended to simulate remains the most questionable aspect of this experimental method and must be addressed through careful analysis.

This page has been intentionally left blank.

Chapter 5: Carbon Sputtering Yield Measurements

The Extended Life Test (ELT) of the Deep Space 1 flight spare ion thruster demonstrated a lifetime of over 30000 hours for the molybdenum ion optics. However, near the end of the testing, the grid apertures had widened to the extent that electron backstreaming became a problem at higher throttle levels. In addition, wear-through pits between the grid apertures were observed, indicating they were near the end of their potential service life. To allow ion propulsion to be applied to missions where higher power and higher ΔVs are required, it is necessary to enhance the propellant throughput capability of the grids by a factor of 5 to 10 times that of the present state of the art design. As a result, a major point of emphasis within the ion propulsion community over the past decade has been to develop grids fabricated from sputter-resistant materials, such as carbon.

Predicting graphite grid life (and by extension, thruster life) requires an accurate knowledge of carbon sputtering yields. The yields for carbon materials are significantly lower than those of most metals, making them difficult to measure experimentally using standard weight loss techniques. In addition, carbon has many polymorphs, allowing it to take on numerous physical forms that have stark differences in physical properties. Carbon is also susceptible to chemical etching under energetic reactive ion bombardment. At low energies, this etching may mask the physical sputtering effects resulting from inert noble gas ions. In addition, carbon traps ions in the surface region to a higher degree than do metallic materials, which may significantly bias mass loss measurements that have been subjected to high irradiation doses. All of these factors likely contribute to the spread between values of C yields obtained at different laboratories, which can be found to vary by nearly an order of magnitude at low energies.

The experimental facility and techniques developed in Chapter 4 for metallic targets are well suited for carbon sputtering yield measurements at glancing incidence, and allow many of the problems discussed above to be addressed with only minor modifications. This chapter begins with

an overview of the recent carbon grid technology development that motivates these yield measurements. The material properties of state of the art carbon grids are analyzed and the difficulties associated specifically with measuring carbon etch rates are reviewed. A discussion of modifications to the experimental quartz crystal microbalance technique developed in the previous chapter to allow for carbon sputtering measurements follows, along with details on the target preparation and characterization. The chapter concludes with a presentation of normal and oblique incidence sputtering yields for $Xe^{+} \rightarrow C$ and $Ar^{+} \rightarrow C$.

5.1 Carbon Grid Technology Development

Carbon is unique because of the number of possible allotropes that may be obtained from the hybridization of its electron orbitals. A neutral carbon atom contains six electrons, and in its ground state two are located in each of the 1*s*, 2*s*, and 2*p* orbitals. By combining the 2*s* and 2*p* orbitals into four equivalent sp^3 hybrid orbitals, the valence state of the carbon atom may be increased from two to four. The additional bonding made possible through this process represents an energetically favorable condition compared to the ground state and is responsible for the tetrahedral structure of substances such as methane and diamond. Another common hybridization form occurs when the four *L* shell electrons are distributed into three sp^2 orbitals and a single delocalized *p* orbital. These bond types are found in all graphitic materials and result in crystals composed of layers of planar hexagonal structures. The sp^2 orbitals form the hexagonal planes and produce strong covalent (σ) bonds with adjacent carbon atoms. The delocalized *p* orbitals are perpendicular to these planes and interact with adjacent planes through weaker van der Waals (π) bonds. Because of the differences in bond strength between the σ (524 kJ/mol) and the π (7 kJ/mol) bonds, the physical properties of individual graphite crystals are highly anisotropic [Pierson, 1993].

Because of its relevance to carbon-carbon grid fabrication, the properties of graphite will be of primary interest here. Diamond coatings have been previously examined as a means of enhancing grid life, however, and a detailed study of diamond sputtering was conducted by Blandino (2001).

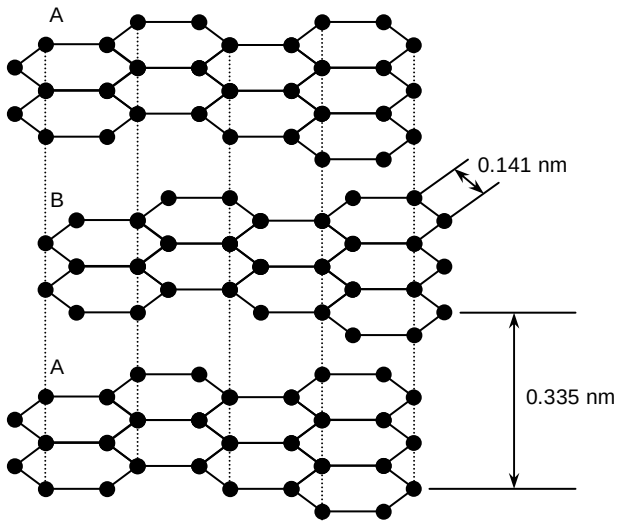

Figure 5.1: Structure of a graphite crystal, as in [Pierson, 1993].

Figure 5.1 shows the structure of a graphite crystal and illustrates the ABAB stacking order of the hexagonal planes. The dashed lines indicate the positions where atoms in adjacent planes overlap. Note that the distance between the atoms at the each vertex of the hexagonal pattern is 2.3 times smaller than the spacing between the planes.

The low sputtering yields associated with carbon materials can be partially attributed to a high surface binding energy, U_s. These energies are somewhat difficult to estimate and are commonly taken to be equal to the sublimation energy of the solid. This is a somewhat questionable approximation, however, given that the ejection of atoms by collisions is fundamentally different from thermal processes that cause desorption from the surface [Duchemin, 2001]. It is generally recognized that the surface binding energy for an individual atom will vary with position and depends on how it is bonded to nearby surface atoms. Hence, for a given surface, one would expect a distribution of binding energies [Sigmund, 1969].

The low sputtering yield of carbon cannot be attributed solely to a high surface binding energy, however, as sputtering behavior also depends on how the energy of an incident ion is deposited within the target surface. Heavy ions such as Xe^+ are not scattered easily when impacting low density, low atomic number targets such as carbon. This results in a greater portion of the energy being deposited

more deeply within the target medium, thereby decreasing the energy transferred to recoils near the surface. The effects of the deposited energy distribution have been developed by Winterbon (1970), and will be discussed further in Chapter 6.

5.1.1 Benefits and Development History

An initial study by Garner and Brophy (1992) recognized the potential benefits of carbon ion optics. Based on prior experimental measurements showing carbon sputtering yields to be several times lower than those of molybdenum at normal incidence [Rosenberg, 1962; Blandino, 2000], graphite grids can mitigate ion optics wear, resulting in a significant improvement in thruster throughput capability for the same operating conditions. As an alternative, substituting carbon for molybdenum enables operation at higher I_{sp} or thrust for a given propellant throughput. The mechanical properties of carbon also offer benefits to the thruster structural design. Graphite's small coefficient of thermal expansion mitigates buckling and helps maintain hole alignment between the screen and accelerator grids during heating associated with thruster operation, enabling operation at higher power densities. This is a significant advantage over metallic materials, for which much larger coefficients of thermal expansion cause buckling to become more severe at larger grid diameters. In addition, the high elastic modulus and low density of graphite make it ideal for spaceflight applications where a high strength to weight ratio is desired [Garner, 1992].

After Garner's initial work, development efforts focused on testing carbon optics in a practical laboratory setting and refining the manufacturing process. Once the benefits of carbon optics were validated through testing on laboratory model thrusters, much of the recent development work has been aimed at bringing the technology to a level of maturity suitable for implementation in spaceflight applications. Major technological hurdles associated with this objective included improving manufacturability and process control, achieving a robust design capable of surviving launch loads, and eliminating voltage stand-off problems. Recent work by Snyder (2003) focused on resolving these issues as part of the Carbon Based Ion Optics (CBIO) program at JPL. This study

extended the prior work by Garner (1992) and Mueller (1995) to 30 cm diameter optics for high I_{sp} applications. During the early design phase of ion thrusters intended for Nuclear Electric Propulsion applications, it was recognized that lengthy burn times would be required to satisfy mission requirements. For these applications, carbon optics were considered an enabling technology, and separate efforts at JPL and NASA GRC extended carbon grids to much larger dimensions [Randolph, 2004; Foster, 2004].

5.1.2 Grid Manufacturing Processes

Carbon-carbon (C-C) is a composite material that consists of fibers held together by a carbon matrix. The fabrication process for C-C is fairly lengthy and complex, in many cases requiring several months to complete. The first stage involves placing the fibers in the desired arrangement, with their orientation depending on the part geometry and the anticipated loading conditions. Typically, they are aligned along directions where the highest strength is required. Multi-directional weaves have been used to make the mechanical properties of the composite more isotropic, an advantage for parts with complex geometries and loading conditions. The matrix material is then introduced in the form of an organic precursor to fill the gaps between the fibers. A polymer resin having a high carbon yield is used in most applications. The resin typically undergoes two curing stages at low temperature (approximately 260 ºC) in an autoclave. Once this is complete, the resin is then charred at high temperature (800 to 1000 ºC), reducing it to pure carbon. This process, known as *pyrolysis*, involves a number of chemical reactions that decompose the precursor material. A common precursor is phenolic resin, used because of its high carbon yield.

Because some mass is lost from the phenolic resin during the pyrolysis stage, the resulting carbon residue is typically quite porous and fairly amorphous, consisting of many small, randomly oriented crystallites. Because of this, the matrix has poor mechanical properties at this stage, and several post-processing steps are required to make the composite more robust. The next fabrication step is a densification stage, where chemical vapor infiltration fills the voids between the fibers and the matrix

with carbon. The amorphous carbon is transformed to a stronger graphite crystal structure through a final high temperature heat treating process known as *graphitization*.

The fabrication procedure used specifically for C-C grids is discussed in detail in a recent publication by Beatty (2005). Pyrolytic graphite has also been used in large, high aspect ratio rectangular grids [Foster, 2004]. The manufacturing process for pyrolytic graphite structures differs from the C-C process in that a gaseous precursor is used exclusively. For pyrolytic graphite, the carbon is deposited via chemical vapor deposition (CVD) onto a substrate that has been molded into the shape of the desired final product. The deposition process produces layers of material, which may be removed from the substrate to produce a free-standing object once sufficiently thick. Because of the layered growth, the physical properties along a particular direction within the finished structure depends on the orientation with respect to the growth direction [Pierson, 1993].

5.1.3 Other Applications in Electric Propulsion

During ground testing, the ions accelerated out of the thruster eventually impinge on the interior walls of the vacuum facility, and a small fraction of the sputtered material redeposits on the thruster itself. The back-sputtering rate is mitigated to some degree by shielding the chamber walls with carbon panels and performing long duration tests in larger chambers. However, even with these measures in place, the redeposition processes cannot be completely eliminated. This is problematic because over time, conductive carbon layers will accumulate on thruster insulators, reducing their voltage stand-off capability [Marker, 2005]. Furthermore, if the testing goal is to assess sputtering damage to thruster components, then carbon redeposition could mask many of these effects by creating a sputter-resistant carbon layer over metallic components [Duchemin, 2001]. More accurate carbon sputtering measurements would allow the influence of these coatings on erosion rates encountered during endurance testing to be better understood.

5.2 Special Considerations for Carbon Sputtering

The previously discussed quartz crystal microbalance (QCM) approach for measuring sputtering yields was modified to allow for its application to carbon. Measuring carbon sputtering yields presents a specialized set of technical challenges compared to those of metallic materials. In the sections that follow, these specific issues are discussed, along with the associated experimental considerations required to address each of them.

5.2.1 Crystal Structure

For most sputtering processes of interest involving polycrystalline metallic materials, the assumption of an isotropic and amorphous target is valid. Whether or not this assumption holds true for carbon is questionable, given its anisotropic crystal structure. The effect of angle of incidence on single crystal structures is particularly dramatic, as some angles allow significant channeling into the surface, thereby reducing the sputtering yield [Roosendaal, 1981]. In many cases, chemical vapor deposition of carbon layers results in a preferred crystal orientation and could influence the sputtering behavior of the material.

As a surface is irradiated, ions come to rest at some depth in the target and create dislocations as they transfer energy to recoils. It is therefore worthwhile to determine whether the original crystal structure near the surface will be destroyed beyond recognition during this damaging process. Information on the state of the surface structure may be gained from low energy electron diffraction (LEED), where an incident electron beam is scattered off of a target, producing a diffraction pattern. The locations of the diffraction peaks are related to atomic positions near the surface. For a single crystal, atomically flat surface, these peaks will be quite sharp. The pattern degrades as the number of defects increases, and an amorphous surface will not have any characteristic peaks. In a review of studies using the LEED technique, Robinson (1981) noted that single crystal metallic targets bombarded with low energy noble gas ions cause a mild degradation of the diffraction pattern, which initially depends on the total irradiation dose. This effect disappears after the dose level reaches

approximately one incident ion per surface atom. This suggests that the pattern was degraded initially due to roughening of the surface, while the underlying crystal structure remained intact. Semiconductor surfaces, on the other hand, appear to be much more susceptible to damage, even from small doses of low energy ions. LEED patterns of semiconductors at room temperature are obliterated after irradiation (Robinson, 1981), indicating severe damage to the surface crystal structure. Under these conditions, the sputtering behavior of semiconductors is similar to that of amorphous materials.

An analysis of surface damage for the specific carbon materials and bombardment conditions for ion thrusters, while useful given the numerous polymorphs of carbon, was considered to be beyond the scope of this investigation. In lieu of such a study, care was taken to deposit the QCM coatings in such a manner that would reproduce the properties of the bulk material as closely as possible. A detailed discussion of the sample preparation method is discussed in Section 5.3.

5.2.2 Chemical Etching

The dominant mechanism of erosion for ion thruster grids is physical sputtering, where atoms in the target material are removed due to kinetic energy deposited within the surface by projectile ions. However, carbon materials are especially susceptible to various chemical effects, where implantation of reactive gas ions results in chemistry changes in the surface region. Such changes have been shown to drastically affect the sputtering yields of carbon materials, especially at low energies.

Reactions between implanted ions and target atoms result in chemical changes that alter the surface binding energy. Depending on whether the binding energy is increased or decreased, physical sputtering processes may be enhanced or reduced. The ejection mechanism is still kinetic energy transfer to molecules within the surface region through collision cascades. As a result, this type of chemical effect is also classified as physical sputtering. By contrast, chemical sputtering processes occur when chemical reactions between surface atoms and reactive gas ions produce molecules

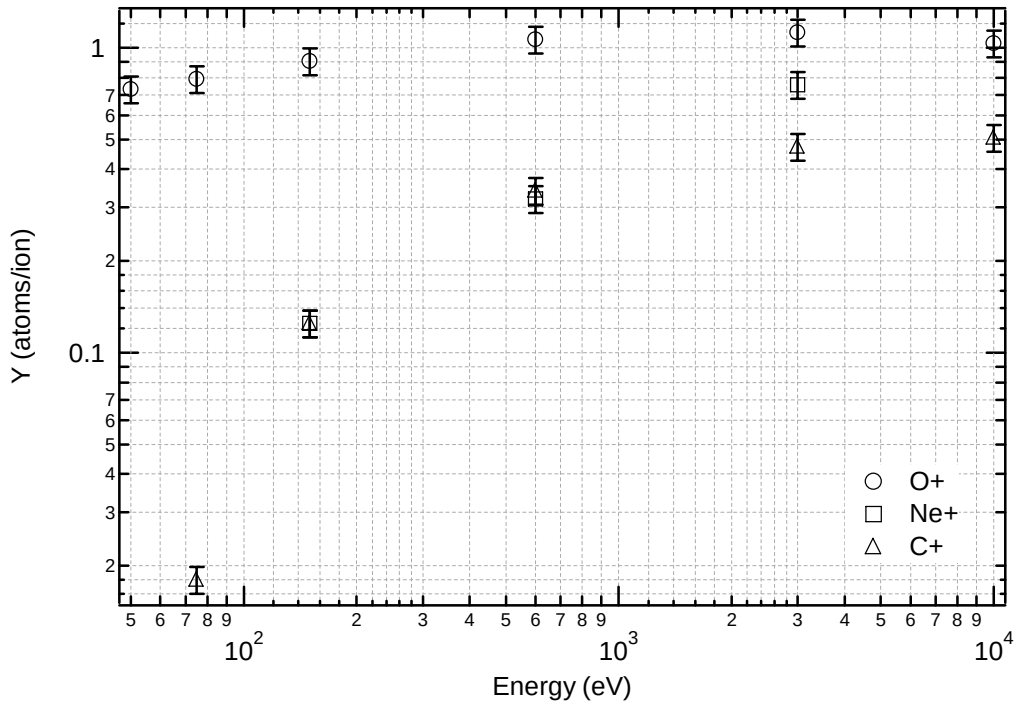

Figure 5.2: Sputtering yields of pyrolytic graphite measured for O^+, Ne^+, and C^+ beams at normal incidence. Data from [Hechtl, 1981].

directly on the surface itself. Typically, these molecules have a low binding energy and desorb at the temperature of the solid [Roth, 1983].

The effect of energetic reactive gas bombardment on carbon sputtering is quite pronounced, especially at low energies. This is evident from a study by Hechtl (1981) in which beams of O^+, C^+, and Ne^+ ions were used to bombard a polished pyrolytic graphite target at normal incidence. The beams were mass-separated, and the targets were maintained at room temperature during the course of the experiment. The resulting sputtering yields were measured by mass loss and are shown in Figure 5.2 with the 10% error bars suggested by the authors. The O^+ etch rate is 49% higher than the corresponding rate for Ne^+ at 3000 eV. The difference becomes more severe as projectile energy decreases. At 150 eV, the ratio of O^+ to Ne^+ sputtering yields is 7.2, and at 50 eV the O^+ yield is nearly 50 times greater than that of C^+. If the oxygen ions were inert, the expected dependence of the sputtering yields on energy would be similar to that of Ne^+ or C^+, both of which have similar atomic masses to O.

Given that chemical etching could mask the physical sputtering effects of interest for the measurements discussed in this chapter, care was taken in the execution of the experiment to eliminate any of these effects. Implantation of reactive species could potentially occur if trace amounts of H_2, O_2, CO, or H_2O were ionized by the ion source and accelerated toward the target. Several steps were taken to minimize this effect. The feed lines that admit gas into the differential pumping port were joined with metal seals and purged and baked in order to desorb water vapor from the tube inner walls. In addition, high purity (99.9995%) research grade xenon and argon were used as the working gases. For this gas purity specification, the major contaminant species exist only in very small amounts, and include H_2O (< 0.5 ppm), CH_4 (< 0.2 ppm), O_2 (< 0.2 ppm), N_2 (< 3.0 ppm), CO_2 (< 0.5 ppm), and CO (<0.5 ppm).

The residual gas analyzer (RGA) was also used to verify that the contaminant gas concentration was small. RGA spectra showing the gas composition with and without Ar flow are displayed in Figure 5.3. The detection threshold of the analyzer was 10^{-12} torr. Only minute differences are

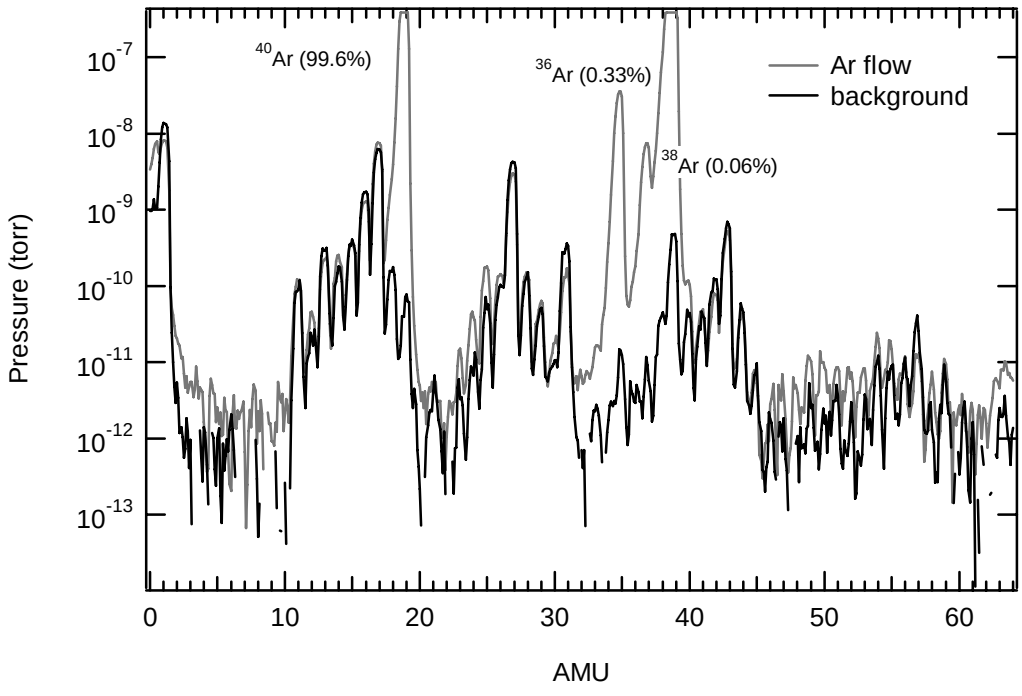

Figure 5.3: RGA spectrum showing working gas composition of during ion etching of the carbon sputtering targets used in this thesis work.

visible for the non-argon peaks, and the differences appear to be within the measurement uncertainty of the device.

5.2.3 Trapping of Ions within the Surface

In a recent study by Doerner (2003), Auger emission spectroscopy (AES) analysis indicated a high concentration of Xe (14%) trapped within the near-surface region of a carbon target bombarded with a plasma discharge. Because of the large mass difference between Xe and C, trapped xenon could significantly bias weight loss measurements for sputtering yields if no account were made for the distribution of implanted ions. AES measurements made on molybdenum samples irradiated under similar conditions did not detect any trapping of Xe.

In Figure 5.4, the C film thickness change measured during the present study for 300 eV Xe^+ ion bombardment is shown. The profile in this figure is subdivided into four segments representing different phases of the etching process. In region 1, transient effects from the accumulation of incident Xe ions in the target surface are visible once the graphite-coated QCM is inserted into the beam. The mass loss due to C sputtered from the target surface is much lower than the mass gain from Xe^+, resulting in a net increase in mass detected by the QCM. Eventually, the Xe saturates the surface and reaches an equilibrium concentration. This corresponds to region 2 of Figure 5.4, where the detected mass change is due only to sputtered carbon atoms. After enough material has been removed to establish an etch rate from the slope of the thickness change curve, the effects of energetic neutrals due to charge exchange processes in the ion gun are assessed by deflecting the ions off of the target. As can be seen in region 3, the flux of Xe to the target decreases in this case, and some of the Xe desorbs, resulting in a new equilibrium concentration in the surface. This is perceived as a transient increase in etch rate due to the loss of the massive Xe atoms within the target. Finally, a second dynamic equilibrium between energetic neutral flux and desorption is achieved, as displayed in region 4.

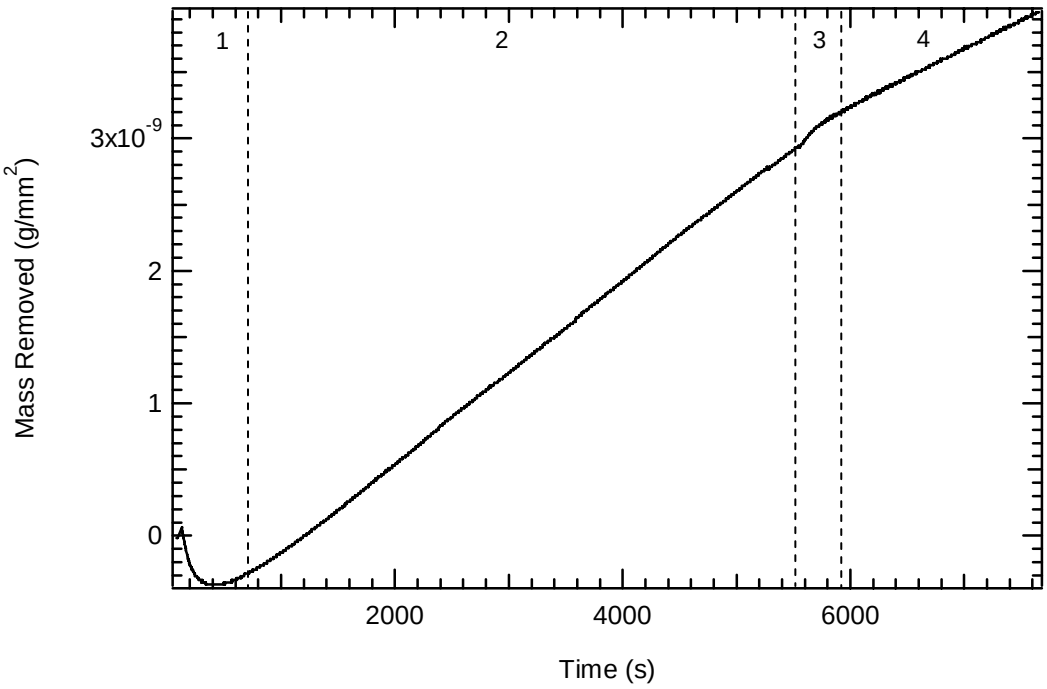

Figure 5.4: Etch profile for 300 eV Xe^+ incident on a C target.

Only the steady state processes in regions 2 and 4 of Figure 5.4 are used in calculations of the sputtering yield. Linear fits determine the total mass loss rate, and the energetic neutral contribution is subtracted to obtain the etch rate due to ions only. Before each testing sequence, the samples were sputter cleaned at high energy (1 keV) to remove any monolayers of adsorbed background gases on the surface. The mass loss due to this initial etching process is not shown in Figure 5.4.

5.3 Target Preparation and Analysis

Applying the experimental technique previously discussed in Chapter 4 to measure carbon sputtering yields requires that the properties of the carbon films deposited on the QCM target mimic those of the bulk material. An important consideration for developing coatings that will satisfy this requirement is whether the deposition process temperature exceeds the maximum allowable temperature of the quartz substrate, 573 ºC. Above this temperature, the quartz recrystallizes into a non-piezoelectric form. Because most carbon composite fabrication techniques used when

manufacturing ion thruster grids require temperatures in excess of 1000 ºC, a number of alternative low temperature deposition techniques were investigated.

As previously discussed in Section 5.1.2, during a conventional chemical vapor deposition (CVD) process, carbon is liberated through the thermal decomposition of a precursor gas and deposited onto a substrate. Common precursors include methane (CH_4), acetylene (C_2H_2), ethylene (C_2H_6), and propylene (C_3H_6) [Pierson, 1992]. The decomposition reactions for these gases typically occur at temperatures of 1100 ºC or higher. An alternate method for liberating the carbon from the precursor gas is plasma-CVD. In this case, an RF plasma source ionizes a propylene-argon or methane-argon gas mixture, allowing for deposition temperatures of 500 ºC or less. Film densities obtained using this method range from 1.5-2.1 g/cm^3 depending on the composition of the gas mixture [Inspektor, 1986]. This range of density values compares well with pyrolytic graphite coatings obtained with thermal CVD.

As an alternative to CVD processing, sputter deposition of the carbon films was also investigated. In a previous study by Hanna and Doerner (2004), deposition techniques were developed at UCSD, the University of California, San Diego, using a UHV facility. The deposition chamber was equipped with a 150 W magnetron sputtering source with a graphite target. The substrates were placed on a plate with a liquid nitrogen shroud approximately 6 in. away from the sputter gun and were heated and cooled between 200 ºC and -185 ºC at alternating intervals during the coating process. Xenon was employed as the working gas at a pressure of 5 mtorr. Using this method, carbon films that resisted flaking and adhered well to the substrate were created.

The film preparation methods described above were expected to provide carbon films that were roughly equivalent in density, although the plasma-CVD technique has the potential to yield a slightly more realistic approximation to the bulk material crystal structure. Given the considerable process development that would be required to achieve this, the more established sputter deposition technique was chosen to create the target films for this study. The QCMs used in the present work were coated by Hanna and Doerner using the deposition procedure described previously. Several industry sources

also attempted to deposit graphite films but were unsuccessful in creating coatings that adhered well to the surface. The resulting carbon layers from the UCSD method were approximately 0.9 μm thick.

Because of the amorphous structure of the carbon films, x-ray diffraction could not be used as a means of obtaining an estimate of the film density. Instead, a witness plate was placed in the deposition chamber along with the samples. A section of the plate was masked, allowing stylus profilometry to be used to determine the film thickness. Using this information in conjunction with weight gain measurements, the film density was found to be 1.6 g/cm^3. This is comparable to the properties of C-C grids, which have a density of approximately 1.8 g/cm^3.

5.3.1 SEM Images

As with the metallic targets, a scanning electron microscope (SEM) was used to characterize the surface topography of the carbon coatings. Figure 5.5 displays a high resolution image of a cross section of a fractured carbon film and Figure 5.6 shows a lower magnification scan of the surface. The cross section image reveals that the films are composed of many small diameter, closely packed, columnar grains. This is similar to the structure observed in the molybdenum coatings described in Chapter 4. As shown in Figure 5.6, the surface, while macroscopically smooth, appears very rough at length scales on the order of 10-100 nm. A more detailed characterization of the surface corrugations is described in Chapter 6. However, given the rather small dimensions of a typical collision cascade during low energy ion bombardment, surface roughness may play an important role in determining the sputtering behavior of materials.

The coatings were deposited in a high purity UHV environment, which serves to reduce the potential for surface contamination. The SEM was used to verify this fact by performing an x-ray fluorescence analysis. Aside from the materials contained in the QCM substrate and electrodes (including Au, Cr, Si, and Fe), no elements other than C were detected in quantities above the threshold of the SEM.

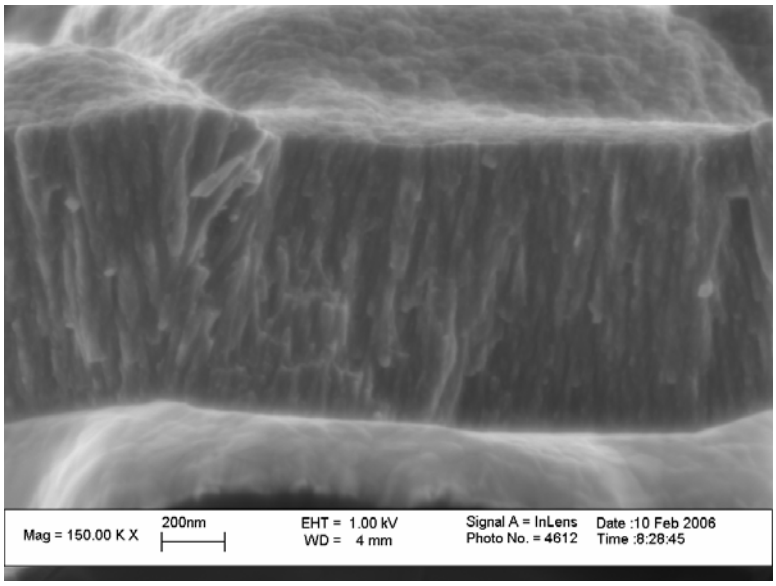

Figure 5.5: SEM image showing the carbon film cross section.

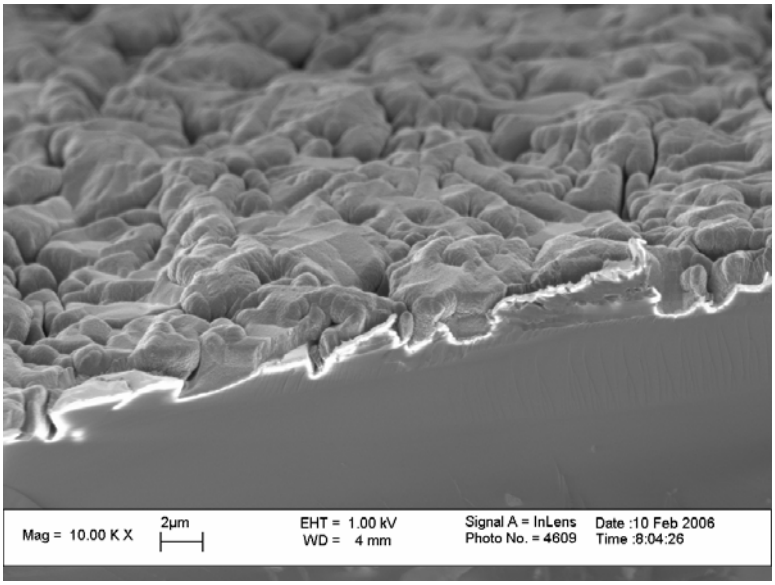

Figure 5.6: SEM image of the carbon film topography.

5.3.2 Raman Spectroscopy Results

For metallic targets, x-ray diffraction has previously been used to provide insight into the crystal structure. Because such measurements provide ambiguous results for carbon coatings, Raman spectroscopy has been used as a method to characterize bond types. The general method uses a laser

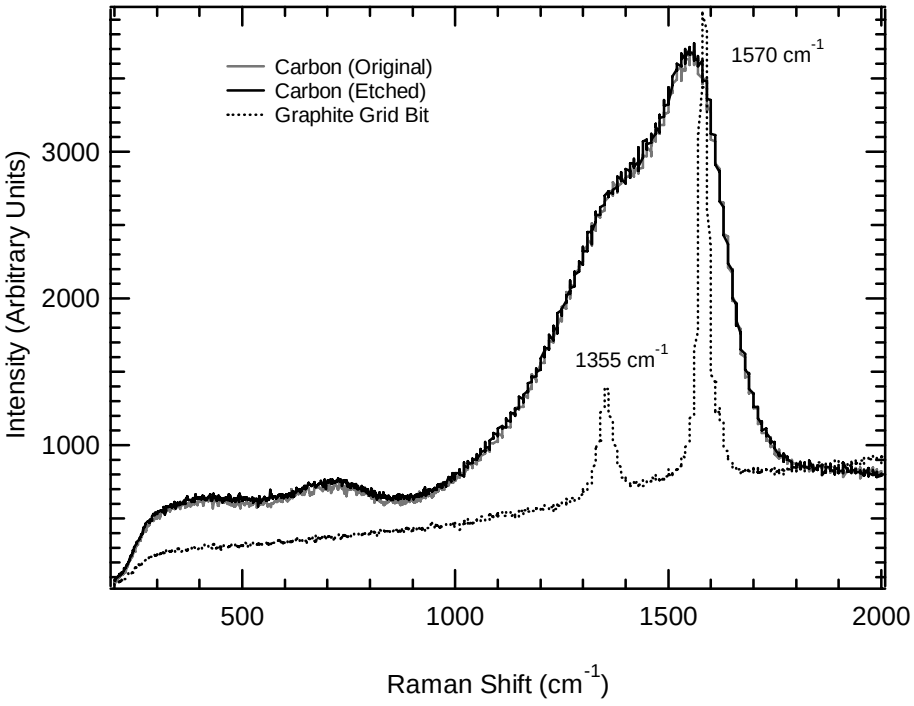

Figure 5.7: Carbon film Raman analysis.

beam to interrogate different bonding states in a sample. Most of the incident photons will be scattered elastically, resulting in no frequency change. However, a small fraction will excite a vibrational state and the scattered photon will be of a lower frequency. The Raman shift is given by

$$\nu = \frac{1}{\lambda_{incident}} - \frac{1}{\lambda_{scattered}}$$

where λ refers to photon wavelength. The magnitude of this shift depends on, among other things, the bonding structure of the solid. For example, in carbon materials, a sharp peak at 1332 cm^{-1} is indicative of sp^3 bonding, suggesting a diamond-like crystal structure. The sp^2 bonding of graphite is characterized by a broader peak at 1570 cm^{-1}. A number of secondary peaks are also visible for higher Raman wave numbers [Tuinstra, 1970].

Raman spectra for the samples used in this study are shown in Figure 5.7. For comparison, the spectrum from a carbon-carbon grid segment from the 65 cm diameter NEXIS thruster has been overlaid. This spectrum features a sharp peak at 1570 cm^{-1}, indicating that the films are highly

graphitic. In addition, a secondary peak is visible at 1355 cm^{-1}. The strength of this peak corresponds to an increase in disordered graphite in the film as well as to a decrease in crystal size [Tuinstra, 1970]. A larger number of crystal defects also increases the peak width. For the carbon films used in this study, the prominence of the 1355 cm^{-1} peak relative to the 1570 cm^{-1} peak therefore indicates that the film is composed of small graphite crystals with many defects, a conclusion supported by the SEM imagery. The "etched" spectrum in Figure 5.7 corresponds to a carbon film that had been subjected to 1 keV Ar^+ bombardment. This process did not appear to substantially affect the Raman spectrum, suggesting that additional crystal defects were not introduced in significant numbers as a result. Finally, it should also be noted that the Raman scattering efficiency for sp^2 bonding is much higher than that of sp^3 bonds in carbon. Because of this, any sp^3 bonding characteristics may be masked by the presence of the 1355 cm^{-1} peak.

5.3.3 Summary

The target analysis indicates the thin films deposited in this study are a reasonable approximation to carbon grid materials. The deposition had the advantage of being a low temperature process, allowing the coatings to be created without damaging the piezoelectric properties of the QCMs. In addition, the films adhered well to the substrate and had densities (1.6 g/cm^3) that were representative of the bulk materials of interest. The largest deviation from the bulk properties was observed with the Raman analysis, which indicated that the films were composed of highly disordered graphite, containing many small crystals with many defects. This structure, however, is representative of a surface that has been damaged significantly by ion bombardment. Given the effects of xenon trapping discussed in Section 5.2.3, it is likely that ion thruster grids would also be damaged in a similar manner after a short period of operation. A LEED analysis on single crystal graphite could be used to verify this assumption.

5.4 Experimental Results

Carbon sputtering yields were measured for both Ar^+ and Xe^+ ion bombardment over an energy range of 100 eV to 1000 eV. Aside from the changes discussed in Section 5.2, the experimental procedure and error analysis remained essentially the same as discussed for the metallic targets in the previous chapter. These data are given in Table 5.1 and are compared with previously published values in Figure 5.8 and Figure 5.9.

Measurements at varying angles of incidence for Xe^+ ion energies of 600 eV and 1 keV are presented in Table 5.2 and Figure 5.10. The peak sputtering yield occurs at θ_{max}=65º, with the ratio $Y(\theta_{max})/Y(0)$=4.7. The sputtering yields increase much more than the Mo data and peak at a much higher angle of incidence. The reasons for this difference will be examined in detail in the following chapter.

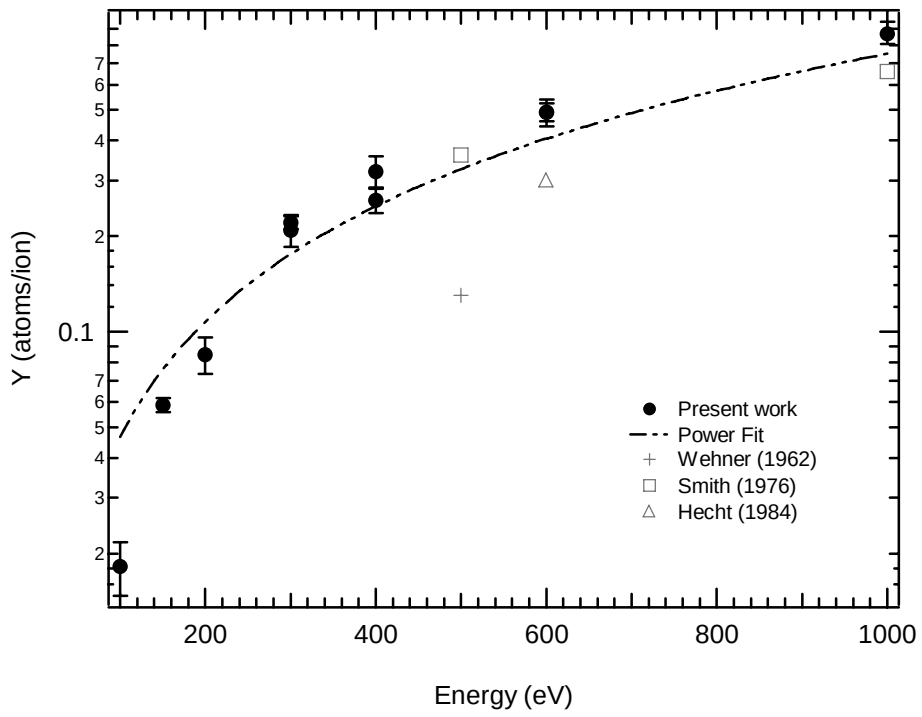

Figure 5.8: $Ar^+ \rightarrow C$ sputtering yields at normal incidence measured in the present study, with previous experimental data included for comparison. Power fit to the current experimental sputtering database developed as part of this thesis work.

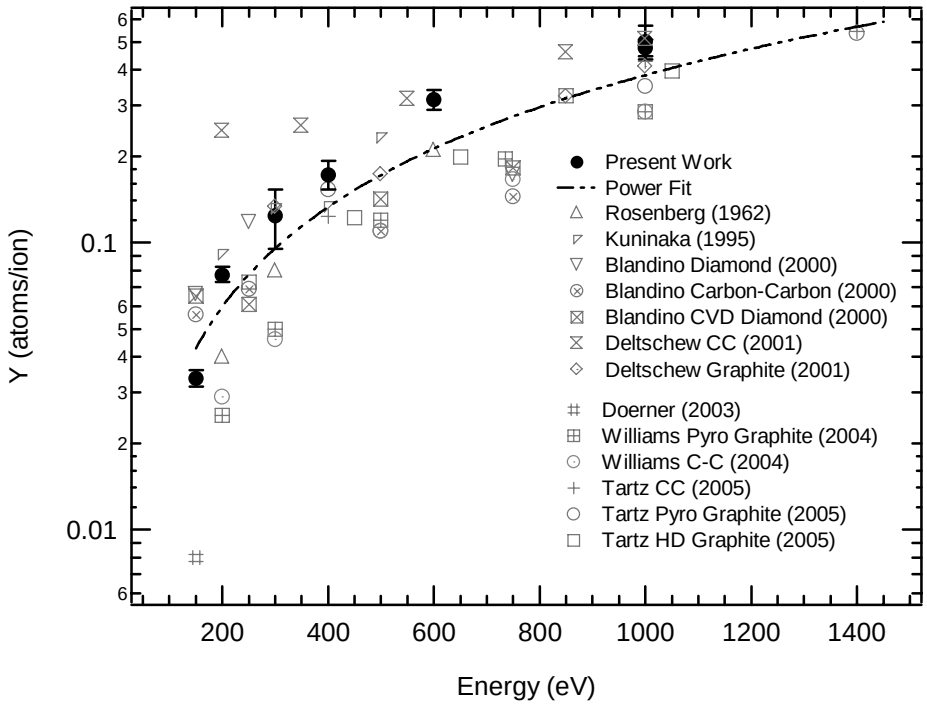

Figure 5.9: Xe^{+}→C sputtering yields at normal incidence measured in the present study, with previous experimental data included for comparison. Power fit to the current experimental sputtering database developed as part of this thesis work.

Table 5.1: Normal incidence carbon yield measurements, from the present work.

Energy (eV)	Y (atoms/ion)	
	Xe^{+}→C	Ar^{+}→C
1000	$0.502^{+0.069}_{-0.068}$	$0.893^{+0.078}_{-0.062}$
	$0.477^{+0.034}_{-0.030}$	
600	$0.316^{+0.026}_{-0.025}$	$0.512^{+0.049}_{-0.048}$
		$0.515^{+0.032}_{-0.030}$
400	$0.172^{+0.020}_{-0.019}$	$0.326^{+0.038}_{-0.034}$
		$0.264^{+0.024}_{-0.022}$
300	0.124±0.029	$0.229^{+0.011}_{-0.010}$
		$0.217^{+0.025}_{-0.024}$
200	$0.077^{+0.005}_{-0.004}$	0.087±0.011
150	0.034±0.002	0.063±0.003
100	···	0.019±0.003

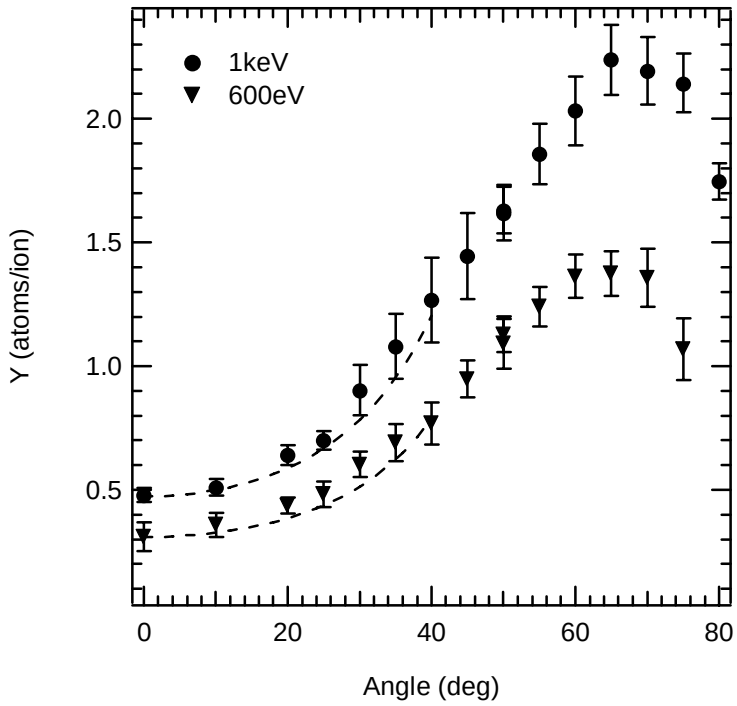

Figure 5.10: Carbon sputtering yields at varying incidence; all data from this thesis work.

Table 5.2: Xe^{+}→C sputtering yields measured in the present study, at varying incidence.

θ (deg.)	Y (atoms/ion)	
	600 eV	1 keV
0	$0.310^{+0.030}_{-0.026}$	$0.499^{+0.030}_{-0.026}$
10	$0.358^{+0.050}_{-0.048}$	$0.532^{+0.035}_{-0.031}$
20	$0.437^{+0.033}_{-0.030}$	$0.669^{+0.040}_{-0.039}$
25	0.482±0.052	$0.731^{+0.038}_{-0.031}$
30	$0.601^{+0.053}_{-0.050}$	$0.927^{+0.068}_{-0.063}$
35	$0.691^{+0.076}_{-0.074}$	$1.13^{+0.11}_{-0.10}$
40	0.768±0.086	1.32±0.13
45	$0.947^{+0.078}_{-0.071}$	1.51±0.17
50	1.13±0.10	$1.69^{+0.18}_{-0.17}$
	1.09±0.07	$1.66^{+0.10}_{-0.09}$
55	1.24±0.08	$1.89^{+0.12}_{-0.11}$
60	1.36±0.09	2.07±0.12
65	1.38±0.09	2.28±0.14
70	1.36±0.12	2.23±0.14
75	1.07±0.13	$2.18^{+0.14}_{-0.13}$
80	···	$1.77^{+0.12}_{-0.11}$

5.5 Discussion

The agreement between the carbon sputtering measurements of the present study and those appearing in published literature at normal incidence is good. The data obtained with this study appear to be within the midrange of the published data sets at energies less than 600 eV, and near the higher end of the data scatter at energies greater than this.

Figure 5.9 includes sputtering yields of Xe^+ incident on a variety of carbon materials from a number of different studies. The published data are distinguished by a fairly large spread between measurements conducted in different laboratories. In addition, there is no obvious correlation between the yield data and crystal structure of the target material. This runs somewhat counter to expectation, given the sizable difference between the diamond sp^3 bond strength (711 kJ/mol) versus that of the sp^2 graphite bonds (524 kJ/mol). Furthermore, the anisotropic crystal structure of graphite caused by the relatively weak bonding between hexagonal planes of atoms would also suggest that the crystal structure should play an important role in determining the total sputtering yield. A possible cause for the lack of correlation between sputtering yield and target crystal structure may be that this effect is masked by surface roughening or other processes discussed in Section 5.2. Both Blandino (2000), Tartz (2005), and Williams (2004) provide a discussion of target damage, as well as SEM images, before and after each testing period. These images clearly show changes in the surface topography due to sputtering. A more detailed surface characterization could yield insight into the effect of surface roughness on the overall sputtering yield.

Empirical curve fits, such as those developed by Matsunami (1984) and Yamamura (1996), significantly underpredict the sputtering yields, especially at lower energies [Tartz, 2005]. This could be partly due to the lack of available experimental data at the time the curve fits were published. In addition, these studies also rely on input parameters such as the surface binding energy, U_s, which are difficult to estimate. If an accurate curve fit is desired, a simpler relationship that captures the basic energy dependence of the sputtering yields would be of more use than the empirical relations.

Sigmund (1969) suggests that for incident heavy ions in the keV energy range, the yields depend roughly on stopping power:

$$Y(E) = 0.0420\alpha \frac{S_n(E)}{U_s} \quad \textbf{5.1}$$

The Lindhard (1968) power cross section may be used to estimate $S_n(E)$. Inserting this cross section, the nuclear stopping power becomes

$$S_n(E) = -\frac{1}{N}\frac{dE}{dR} = \int_0^{T_m} Td\sigma = \int_0^{\gamma E} T(CE^{-m}T^{-1-m}dT) = \frac{C}{1-m}\gamma^{1-m}E^{1-2m} \quad \textbf{5.2}$$

Combining the two formulas above suggests a dependence of $Y(E) \sim E^{1-2m}$. In the energy range of 100 eV <E< 1 keV, the accuracy of the Lindhard cross section diminishes. In this situation, Sigmund suggests the following sputtering relationship for lower energies, based on the simpler Born-Mayer interaction:

$$Y(E) = \frac{3}{4\pi^2}\alpha\frac{\gamma E}{U_s} \quad \textbf{5.3}$$

The above formula indicates a $Y(E) \sim E$ dependence. Based on Eqns. 5.1 and 5.3, a simple power fit of the form $Y(E)=AE^n$ for the present carbon sputtering yield database is proposed, where A and n are the fitted parameters. These are shown below in Table 5.3, for both Ar^+ and Xe^+ incidence. The fitting formula described above is expected to be accurate for energies as low as 100-200 eV. Experimental measurements have shown sharp decreases in sputtering yields as a function of energy below 100 eV [Doerner, 2003]. The binary collision assumption used in Sigmund's work also begins to break down in this energy range, indicating the need for a modeling effort for low energy sputtering.

Table 5.3: Carbon sputtering yield fit parameters.

Ion	A	n
Ar^+	1.78×10^{-4}	1.21
Xe^+	1.31×10^{-4}	1.16

In Figure 5.10, the sputtering yield data are compared to a $\cos(\theta)^{-f}$ dependence. The f=5/3 value suggested by Sigmund's theory (1969) underpredicts the sensitivity of Y on angle of incidence at low angles. As previously mentioned, the C data exhibit a much stronger dependence on angle of incidence compared with the $Xe^{+}\rightarrow$Mo data from Chapter 4. The $\cos(\theta)^{-f}$ form was adjusted to match the experimental observations, with f=7/2. The differences between the carbon and molybdenum data sets will be examined further in the following chapter.

5.6 Concluding Remarks

In this investigation, carbon sputtering yields were measured experimentally at varying angles of incidence under xenon bombardment. Such data are of great importance for modeling ion thruster propellant throughput capability, where accurate yields are needed for most computational models designed to assess grid wear. The measurements were obtained using a quartz crystal microbalance (QCM) technique that had been developed and validated previously for metallic targets.

A great deal of attention was devoted to obtaining carbon coatings that accurately approximated the properties of bulk graphite. Possible deposition methods were constrained by the temperature limitations of the substrate material. A low temperature sputter deposition process developed at UCSD allowed films that adhered well to the surface to be created. Analysis of a witness plate placed in the sputter deposition chamber indicated a coating density that was comparable to the bulk material. Scanning electron microscopy (SEM) and Raman spectroscopy indicated that the films were composed of disordered graphite, considered to be a reasonable approximation to a sputter-damaged carbon surface.

The high sensitivity of the diagnostic technique developed in this thesis is ideally suited for measuring the etch rates of sputter-resistant materials such as carbon. Conventional mass loss measurements based on gravimetric or profilometry methods require days of continuous ion source operation to obtain an individual sputtering data point. The technique employed here, by contrast, reduces the necessary test duration to roughly 3 hours. The *in situ* measurements from the QCM

provided the unique benefit of enabling ion trapping in the target surface to be observed during bombardment, an effect that cannot be observed with other techniques.

C sputtering yields measured under Ar^+ and Xe^+ bombardment at normal incidence were in close agreement with previously published data over an energy range of 200 eV to 1 keV. An empirical curve fit based on results of existing sputtering transport theory models is proposed. For Xe^+ ions, the first glancing angle yield measurements for C were obtained. Over the range of $0° \leq \theta \leq 80°$, an increase in C sputtering yield by a factor of 4.7 was observed, with $Y(\theta_{max})/Y(0)$ occurring at 70°. This is significantly different from the sputtering behavior observed for Mo in the previous chapter.

Chapter 6: Surface Characterization and Modeling

As discussed in Chapter 3, a number of fairly sophisticated sputtering theories exist. However, most of the major approximations made by these models involve large simplifications in the treatment of the surface boundary condition. These approximations are generally required to make the mathematics or computational solution tractable, but at a cost of lower accuracy for oblique angles. For the transport theory case, recall that the target medium is treated as being infinite, and the surface is an imaginary plane through which particle motion is tracked. For Monte Carlo codes using the binary collision approximation, the surface boundary is somewhat more sophisticated, as particles are tracked in a half-space rather than an infinite space. However, the surface is still treated as being atomically flat, with a planar surface binding energy as a threshold for particle ejection. Since sputtering at oblique incidence involves numerous collisions near the surface, simplified treatments such as these tend to be insufficiently detailed under these conditions.

Often, the experimental studies that these models are compared with also are lacking in terms of surface characterization. Few studies provide a detailed analysis of target surface roughness or crystal structure, both of which could have a dramatic impact on sputtering at glancing incidence. The average ion range for 1 keV Xe^+ incident on Mo is on the order of 13 Å. From the scanning electron microscope (SEM) imagery of the previous sections, however, it is clear that this is much smaller than the average surface feature size for the samples used in this study. At a microscopic level, the local angle of incidence may be different from the angle the target makes with the beam from a macroscopic perspective. Portions of the surface may be shadowed from sputtered particles by large surface features, resulting in redeposition sites at these locations. Clearly, surface roughness could influence the measured sputtering yields, and understanding these effects requires a detailed characterization of the target surface roughness.

In general, addressing the issues discussed above would partially resolve the large discrepancies previously observed between the experimental data and modeling approaches. In this chapter, these effects are addressed through modifications to modeling approaches described in Chapter 3. The chapter begins with a discussion of a solution to the Sigmund transport theory model in two dimensions. This solution is used to reconstruct the damage and range distributions for different ion-target mass ratios and addresses the observed differences in the sputtering yield angular dependence between molybdenum and carbon. In the following sections the effects of surface roughness are examined in detail. Surface corrugations are mapped with atomic force microscopy, a technique that allows features to be measured with a height resolution of 1 nm. This surface map is used to characterize the local beam incidence angle distribution.

6.1 Analysis of Experimental Results

Sputtering yield measurements as a function of angle of incidence were measured for Mo and C under Xe^+ bombardment and have been discussed in Chapters 4 and 5 of this thesis. These data have been normalized to their normal incidence values and are presented together in Figure 6.1. The data appear to collapse onto two distinct curves suggesting that, for the projectile energies investigated, the difference in target material has a profound influence on the angular dependence of the sputtering behavior. It also suggests that the peak sputtering yield and the angle at which this occurs are not strong functions of incident ion energy, at least over the energy range relevant for ion propulsion. For Xe^+ incident on C, Y increases by a factor of 4.7, peaking between 65º and 70º. For the Mo case, a much smaller ratio of $Y(\theta_{max})/Y(0) = 1.6$ is evident, with $50º < \theta_{max} < 55º$.

The differences between the Mo and C sputtering at oblique incidence are better understood by considering how the target atoms scatter the projectile ion. Such insight may be gained using transport theory to calculate detailed information about the collision cascade dimensions. Of particular interest is the kinetic energy transferred to the target as a function of depth, as well as the distribution of projectiles once they come to rest within the surface. Obtaining this information

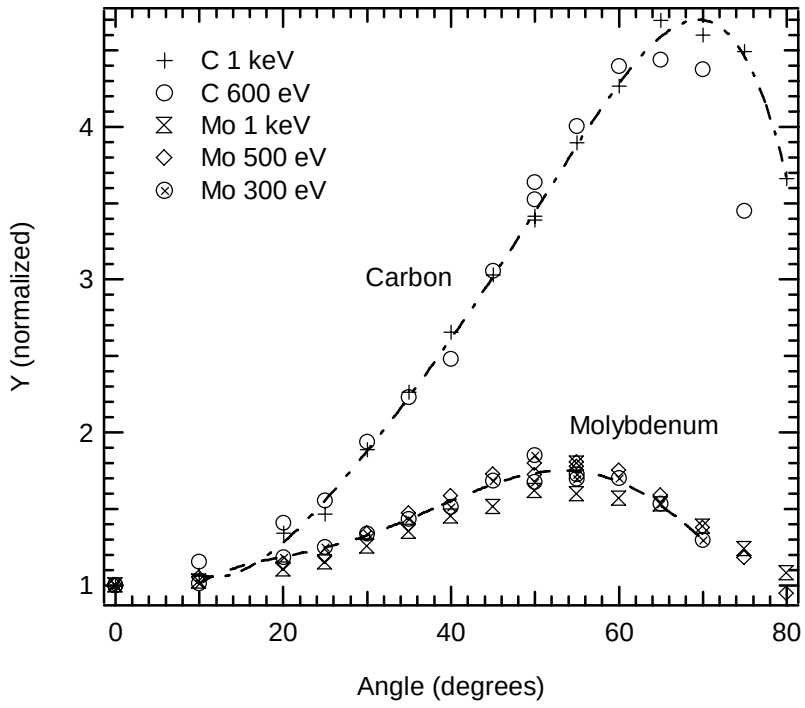

Figure 6.1: Normalized sputtering yield plots for the experimental data collected in this study. The dashed lines are intended only to guide the eye.

requires the construction of the damage and range distributions from spatial moments of Boltzmann's equation. Only the general approach for accomplishing this is included in Sigmund's original work (1969); more detailed discussions of this approach are provided by Sanders (1969) and Wintenbon (1970).

6.1.1 Calculation of Spatial Moments

Our present interest in solving Boltzmann's equation is to obtain expressions that allow us to reconstruct the distribution $F(E,\mathbf{r})$. Recall that whether or not $F(E,\mathbf{r})$ represents the range or damage distribution depends on the inclusion of terms that account for recoils in the collision operator of Boltzmann's equation. The form of the distribution depends on the geometry under consideration. For the case of a planar source, F will be a function of only one spatial coordinate x, energy E, and the direction cosine of projectile impact angle $\eta=\cos(\theta)$. For a point source geometry, the distribution may be constructed in three dimensions, using a beam centered coordinate system. However, because

the target medium is usually assumed infinite and isotropic, the problem is essentially reduced to two dimensions because the cascade geometry is independent of azimuth angle. The coordinate systems used in the analysis of both geometries are shown in Figure 6.2.

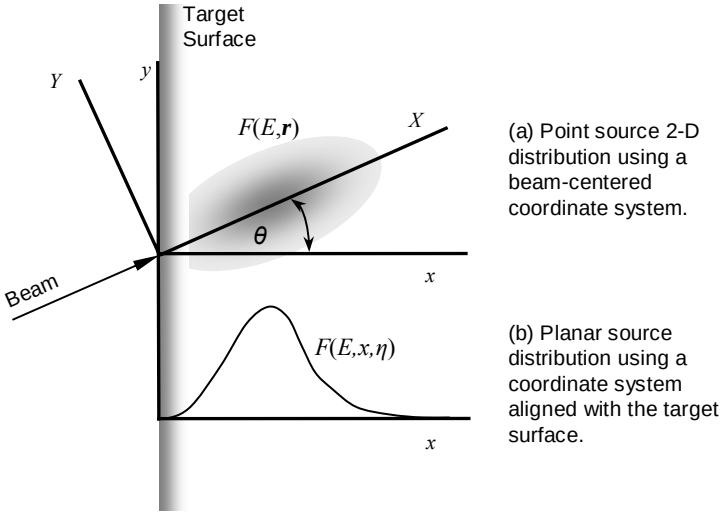

Figure 6.2: Coordinate system for range and damage distribution calculations.

Solutions for the distributions may be obtained computationally, though an analytical approach provides a great deal of insight into the factors influencing cascade dimensions. The general procedure involves calculating spatial moments of the distribution function, which provide insight into a number of important statistical properties. The physical significance of the first few moments is outlined in Table 6.1 and Table 6.2 for the 1-D planar and 2-D point source, respectively. The first order moments are of fundamental importance as they provide information on the mean depth $\langle X \rangle$ of the distributions within the target surface. Given an infinite and isotropic target, the cascade geometry is not expected to depend on azimuth angle. Because of this, the distribution must exhibit symmetry about the X-axis in the beam centered coordinate system, and $\langle Y \rangle = \langle Z \rangle = 0$. However, of particular interest for the present analysis are the second order moments, as they indicate the width of the cascade both parallel and perpendicular to the direction of ion impact. The notation of Winterbon (1970), which defines longitudinal straggling as $\langle \Delta X^2 \rangle / \langle X \rangle^2$ and transverse straggling as $\langle Y^2 \rangle / \langle X \rangle^2$,

will be used throughout this study. The centralized higher order moments account for *skewness* (the degree of asymmetry in the distribution) and *kurtosis* (how sharply peaked the distribution is).

Table 6.1: Spatial moments for a planar source coordinate system. [Winterbon, 1970]

Mean projected range	$R_p(E) = \int xF(E,1,x)dx$
Mean depth	$< x >= \int xF(E,\eta,x)dx = \bar{x}$
Longitudinal straggling	$\sigma_{\|}{}^2(E) = \int (x - R_p(E))^2 F(E,1,x)dx$
Transverse straggling	$\sigma_{\perp}{}^2(E) = \int x^2 F(E,0,x)dx$
Skewness	$< \Delta x^3 >= \int (x - \bar{x})^3 F(E,\eta,x)dx$
Kurtosis	$< \Delta x^4 >= \int (x - \bar{x})^4 F(E,\eta,x)dx$

Table 6.2: Spatial moments for a 2-D beam centered coordinate system. [Winterbon, 1970]

Mean depth	$< X >= \int XF(\vec{r},E)dXdYdZ = \overline{X}$
Longitudinal straggling	$< \Delta X^2 >= \int (X - \overline{X})^2 F(\vec{r},E)dXdYdZ = \sigma_{\|}$
Transverse straggling	$< Y^2 >= \int (Y - \overline{Y})^2 F(\vec{r},E)dXdYdZ = \sigma_{\perp}$
Skewness	$< \Delta X^3 >= \int (X - \overline{X})^3 F(\vec{r},E)dXdYdZ$
Kurtosis	$< \Delta X^4 >= \int (X - \overline{X})^4 F(\vec{r},E)dXdYdZ$

6.1.2 1-D Solution Method

The Boltzmann equation may be solved directly in two dimensions. However, it is mathematically easier to derive the solution using the planar source and transforming this solution to the beam centered coordinate system. The details of this process are presented in Appendix A, and will be applied in the following sections. For this reason, the 1-D derivation is a useful starting point for this analysis. The spatial moments may be expressed as follows:

$$< x^n >= \left(\frac{E^{2m}}{NC} \right)^n \sum_{l=0}^{\infty} (2l+1) A_l^n P_l(\eta) \qquad \textbf{6.1}$$

To eliminate the dependence on E, N, and C, it is useful to define

$$< x^n >= \nu_n \left(\frac{E^{2m}}{NC} \right)^n \tag{6.2}$$

Once the spatial moments have been calculated, the range and damage distributions may be reconstructed. Prior experimental measurements of range and damage suggest the distributions are roughly Gaussian in shape. An expansion that has been used extensively in neutron transport applications is the Edgeworth series, given as a sum of Hermite polynomials in the following form:

$$F(x(\xi)) = \frac{1}{\sqrt{2\pi}} e^{-\xi^2/2} \sum_{m=0}^{\infty} c_m He_m(\xi) \tag{6.3}$$

From a practical standpoint, only a finite number of terms may be used in the reconstruction of the distributions, and the Edgeworth series does not represent a unique solution to the Boltzmann equation under these conditions. Note that ξ is a normalization parameter for the cascade depth that depends on the first two spatial moments:

$$\begin{aligned} \xi &= \alpha(x - a) \\ a &= \nu_1 \\ \alpha &= \frac{1}{\sqrt{\nu_2 - a^2}} \end{aligned} \tag{6.4}$$

The coefficients c_m are sums of Hermite polynomials in terms of spatial moments:

$$c_m = \frac{\alpha}{m!} \sum_{r=0}^{m} \binom{m}{r} \alpha^r \nu_r He_{m-r}(-a\alpha) \tag{6.5}$$

6.1.3 2-D Range and Damage Distributions

For a 2-D point source geometry, we may construct the damage and range distributions from spatial moments using a bivariable Edgeworth expansion [Longuet-Higgins, 1963; Lokas, 1998].

This distribution has the form

$$F(\xi(x),\chi(y)) = \frac{1}{2\pi}\exp\left[-\frac{\xi^2+\chi^2}{2}\right]\left[1+\frac{1}{6}\left(\lambda_{30}H_{30}+3\lambda_{21}H_{21}+3\lambda_{12}H_{12}+\lambda_{03}H_{03}\right)+\ldots\right] \qquad \textbf{6.6}$$

The H_{ij} are a two-dimensional version of the Hermite polynomials. For the special case where the ξ and χ variables are not correlated, these polynomials reduce to $H_{nm}(\xi,\chi)=H_n(\xi)H_m(\chi)$ [Lokas, 1998]:

$$\begin{aligned} H_{30} &= \xi^3 - 3\xi \\ H_{21} &= -\chi - \chi\xi^2 \\ H_{12} &= -\xi - \xi\chi^2 \\ H_{03} &= \chi^3 - 3\chi \end{aligned} \qquad \textbf{6.7}$$

The coefficients λ_{ij} are defined according to

$$\lambda_{ij} = \frac{\kappa_{ij}}{(\kappa_{20}^{i}\kappa_{02}^{j})} \qquad \textbf{6.8}$$

where the κ_{ij} are the *cumulants* of the distributions. Edgeworth expansions are commonly expressed in terms of cumulants, κ_{ij}, rather than moments, v_{ij}, for the sake of simplicity. The cumulants defined in terms of moments for the terms necessary to reconstruct the distribution function up to a second order approximation are [Longuet-Higgins, 1963]:

$$\begin{aligned} \kappa_{20} &= <X^2> - <X>^2 = <\Delta X^2> \\ \kappa_{02} &= <Y^2> - <Y>^2 = <Y^2> \\ \kappa_{30} &= <X^3> - 3<X><X^2> + 2<X>^3 \\ \kappa_{03} &= <Y^3> - 3<Y><Y^2> + 2<Y>^3 = 0 \\ \kappa_{21} &= 2<Y><X>^2 - 2<X><XY> - <Y><X^2> + <X^2Y> = 0 \\ \kappa_{12} &= 2<X><Y>^2 - 2<Y><XY> - <X><Y^2> + <XY^2> = <XY^2> - <X><Y^2> \end{aligned} \qquad \textbf{6.9}$$

The bivariate Edgeworth expansion is used to generate the damage and range distributions for both molybdenum and carbon in two dimensions. The resulting distributions are shown in Figure 6.3 and Figure 6.4. Because the beam centered coordinate system has been employed, the cascade shape is invariant with angle of incidence. This illustrates one of the deficiencies associated with infinite medium solutions, as portions of the collision cascades may exist outside of the domain of interest.

With the distributions shown above, recoils may move across the surface plane, undergoing collisions outside of the target and moving back across the boundary.

Figure 6.3 and Figure 6.4 also illustrate the different distribution shapes for molybdenum and carbon. The Mo cascade shapes are much more spherical than the carbon case, indicating a much greater ratio of transverse to longitudinal straggling. This can be expressed quantitatively by examining the variation of $\langle Y^2 \rangle / \langle \Delta X^2 \rangle$ as a function of mass, shown graphically in Figure 6.5. Note that as M_2/M_1 increases, $\langle Y^2 \rangle / \langle \Delta X^2 \rangle$ becomes larger, indicating a cascade elongated along the direction of impact. Likewise, for large mass ratios $\langle Y^2 \rangle / \langle \Delta X^2 \rangle$ approaches 1, indicating a nearly spherical cascade. The variation of straggling as a function of mass ratio is shown in Figure 6.6. Higher transverse straggling under these conditions makes sense physically, because the lighter target will be less able to scatter the projectile off of its original trajectory.

From a qualitative standpoint, the variation in collision cascade shape provides insight into how sensitive a particular material will be to sputtering by a particular ion species. It has been established that the sputtering yield increases as the incidence angle θ increases because more collisions take place near the surface. More energy is deposited near the surface as a result, allowing a greater number of recoils to achieve sufficient energy to overcome the surface binding energy, U_s. For a collision cascade that is more elongated along the direction of the beam, a greater variation in energy deposited near the surface would be expected as a function of θ. This is clearly the case for carbon, and the experimental data show an increase in Y by a factor of 4.7. Likewise, molybdenum, which has a much more spherical cascade structure by comparison, shows a much milder sensitivity to θ. More quantitatively accurate predictions of the sputtering yield variation with angle, including the location of θ_{max} and the decrease in Y at glancing incidence, would require a much more detailed treatment of the surface than has been typically applied in transport theory solutions.

Note that in both Figure 6.5 and Figure 6.6, there is no explicit dependence on incident ion energy, E. The moments of the distribution function scale according to $(E^{2m}/NC)^n$, where C and m are constants that depend on the parameters of the collision, and n is the moment order [Winterbon,

1970]. Hence, both $\langle Y^2 \rangle$ and $\langle \Delta X^2 \rangle$ scale according to $(E^{2m}/NC)^2$, and considering the ratio $\langle Y^2 \rangle / \langle \Delta X^2 \rangle$ eliminates the energy dependence. Likewise, $\langle X \rangle$ scales according to (E^{2m}/NC), and therefore both the longitudinal straggling $\langle \Delta X^2 \rangle / \langle X \rangle^2$ and transverse straggling $\langle Y^2 \rangle / \langle X \rangle^2$ (as defined by Winterbon in 1970) are independent of energy as well. This suggests that the relative dimensions of a collision cascade are not energy dependent. However, it is important to apply this conclusion with care. The cross sections used in the solution of the transport equation are valid over a limited energy range (dictated by the collision parameter, m.) In addition, the cross section form used here assumes only elastic collisions and neglects electronic stopping. Fortunately, these assumptions are valid for low energy, heavy ion scattering over the limited energy range of interest for ion propulsion applications. Under these limitations, this analysis appears to support the experimental observations where the data from the same ion target combinations at different energies collapse onto the same curves.

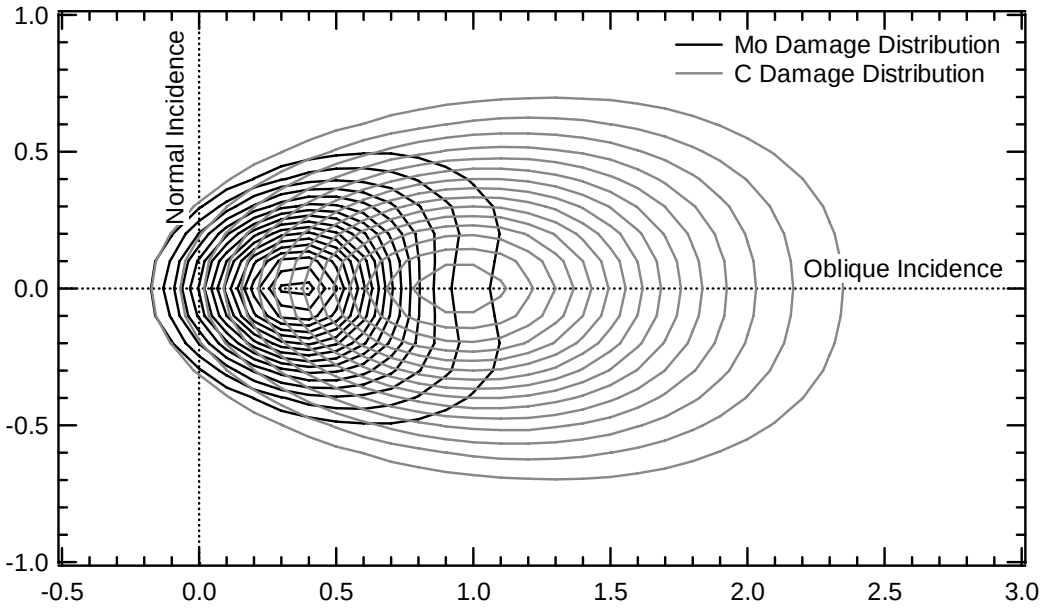

Figure 6.3: Damage distribution for C and Mo collision cascades, calculated using the method developed by Winterbon (1970). Axes have been normalized to the path length $R(E)$.

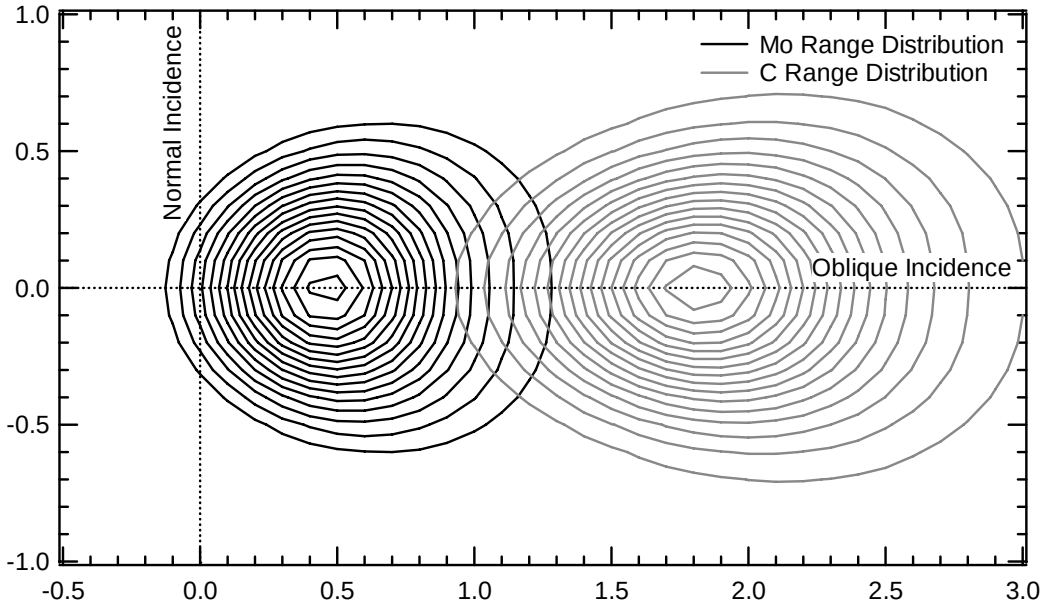

Figure 6.4: Range distribution for C and Mo collision cascades, calculated using the method developed by Winterbon (1970). Axes have been normalized to the path length *R*(*E*).

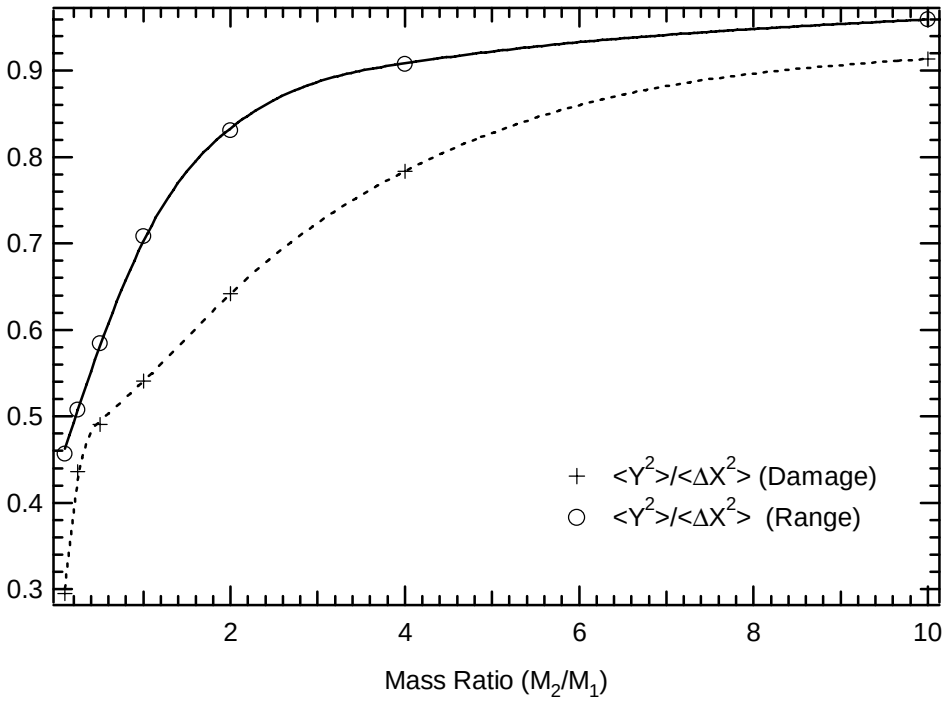

Figure 6.5: Ratio of transverse to longitudinal straggling as a function of mass fraction. Calculations from present work.

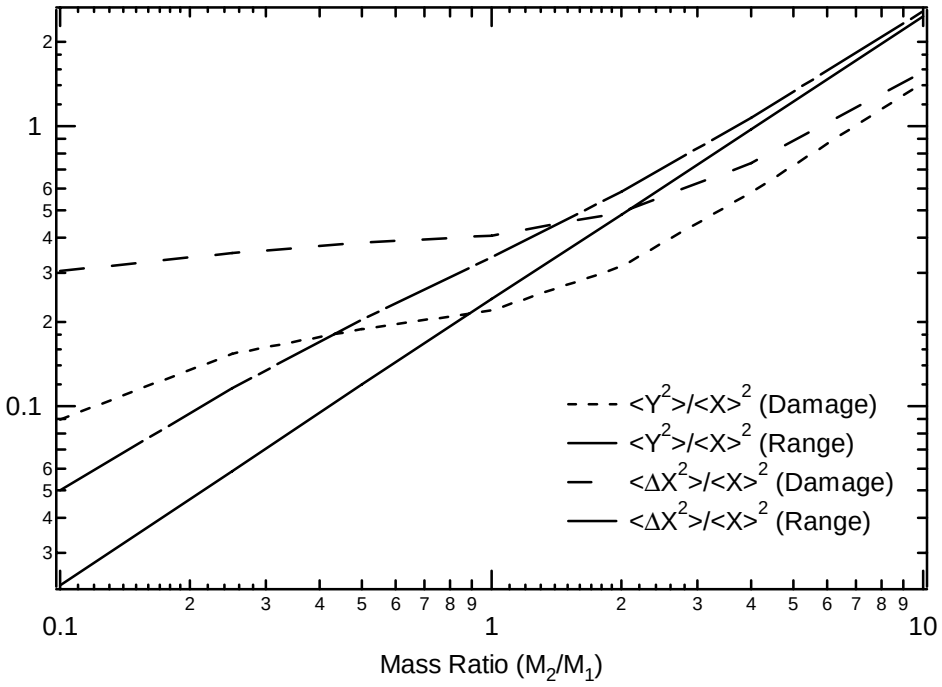

Figure 6.6: Longitudinal and transverse straggling as a function of mass fraction, as in [Winterbon, 1970].

6.2 Surface Height Characterization

Macroscopically, the coated QCMs from the sputtering experiments appear perfectly smooth. Under low level magnification with a laboratory microscope, some surface texturing is visible. With a high magnification SEM, these surface variations appear quite large in extent. This illustrates that the significance of surface roughness clearly depends on the scale of interest and brings up the question of what the appropriate characteristic length is for sputtering processes. A logical choice would be the projected range $R_p(E)$ of the incident particles. Using Ziegler's stopping power program TRIM, the projected ranges for $Xe^+ \rightarrow C$ and $Xe^+ \rightarrow Mo$ are shown in Table 6.3.

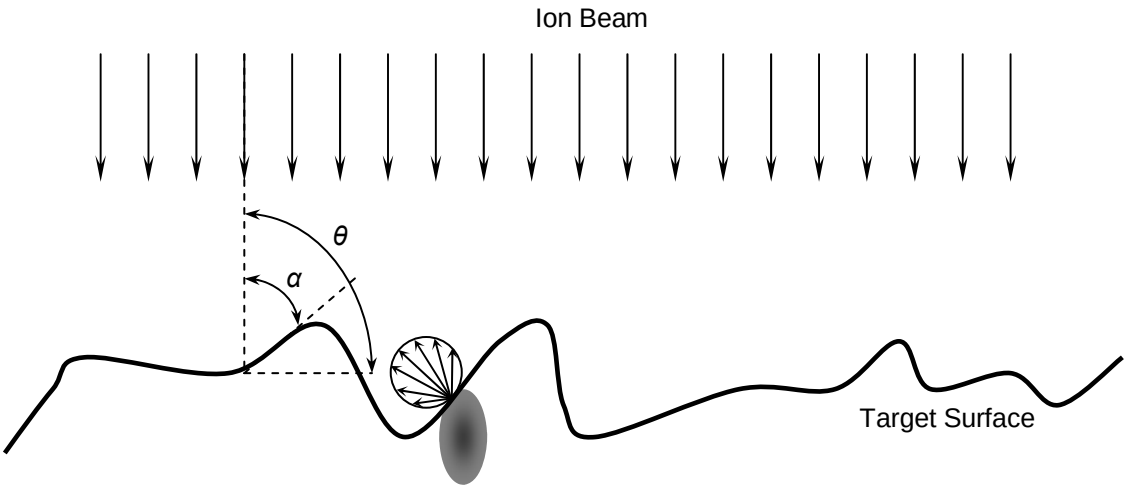

Figure 6.7: Local angle of incidence for a rough surface.

Table 6.3: Projectile ranges for Xe^+ incident on C and Mo.

Ion Energy, eV	Projected Range, Å	
	$Xe^+ \rightarrow C$	$Xe^+ \rightarrow Mo$
100	13	5
200	17	7
300	20	8
500	25	10
700	29	11
1000	33	13

From the table, xenon atoms only penetrate 33 Å in a carbon surface. However, most surfaces that have been textured by large ion bombardment doses have surface structures significantly larger than this. In the cross section SEM images of the films used here, thickness variations of at least 0.1 μm may be clearly seen. Based on these observations, it seems reasonable to distinguish the *local* angle of incidence from that of the overall macroscopic surface. The difference between these two quantities is illustrated in Figure 6.7, where α and θ indicate the local and overall angles, respectively. The shaded region shows the relative size of the collision cascade, along with the efflux of sputtered particles from this point. Note that at increasing incident angles, portions of the surface may become

shadowed by large features. Furthermore, redeposition will occur in areas where the trajectories of sputtered particles intersect with higher points on the surface.

6.2.1 Atomic Force Microscope Measurements

To address the issues of surface roughness, the surface feature heights of the samples used in this study were characterized with an atomic force microscope (AFM). While a number of other diagnostic techniques, including stylus profilometry, exist to accomplish this task, the AFM was selected due to its high sensitivity and its capability to create a surface height map over a given area. A typical AFM, shown in Figure 6.8(a), uses a small measurement tip attached to a cantilever to probe the sample. As the sensing needle approaches contact, the van der Waals forces between the probe tip and the atoms of the target surface cause deflections of the cantilever, which may be measured with a position sensitive detector. For this application, optical interferometry or scanning tunneling microscopy are typically able to measure cantilever deflections as small as 10^{-2} Å [Oura, 2003]. The cantilever assembly is mounted to a small computer driven piezoelectric scanning stage that controls the needle position to a high degree of accuracy. The scanning stage moves the tip over the sample in a raster pattern, providing surface height output as a function of x-y position.

The samples in this study were sputter deposited, and the resulting surfaces had height variations on the order of 200 nm. While certainly within the sensing range of an AFM, this is a fairly large height scale. Because of this, the AFM was operated in *tapping* mode, where the sensing needle oscillates vertically with an amplitude on the order of 10 Å. This allows it to make soft contact with the surface during each cycle, which is ideally suited for characterizing rough surfaces.

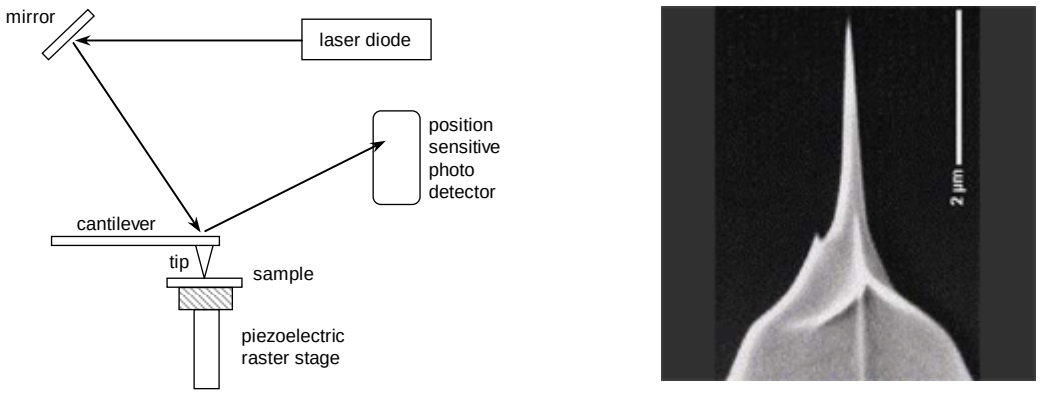

Figure 6.8: (a) AFM Schematic, as in [Zhao (2001)] (b) SEM image of Veeco TESP-HAR tip, from [Veeco (2006)]

In addition, care must be taken to ensure that systematic errors are not introduced by the finite size of the measurement tip. The tip used in this study was a Veeco TESP-HAR, which is specifically designed for characterizing surfaces with large corrugations. The tip itself is nanofabricated to a height of 1.5 μm and a base width of 290 nm, giving it a high aspect ratio, as shown in Figure 6.8(b). It tapers off to a spike with a radius of curvature of 10 nm. This apex is not atomically sharp, and during soft contact, only the atoms that compose the largest surface feature on the spike interact with the sample. Even with the high aspect ratio of this tip, features on the sample that have very steep edges or sharp points will not be imaged properly. In such situations, the surface may contact points on the side of the tip as well as on the apex, introducing undesired *convolution* artifacts as the measurement needle drags across the sample. This limits the achievable scan region to areas that will not see large variations in surface height. For the conditions of this study, the maximum grid size obtained was a 5 μm square. This area, however, was sufficiently large to capture a statistically meaningful sampling of the surface. A grayscale map of a 5 μm × 5 μm region on the carbon sample surface appears in Figure 6.9. In addition, Figure 6.10 shows a 3-D map of this same sample region, along with a height distribution function (note that the vertical scale on the 3-D map is much smaller than the horizontal scale.) The surface features fall within an approximately normal distribution, with a height standard deviation of 136 Å.

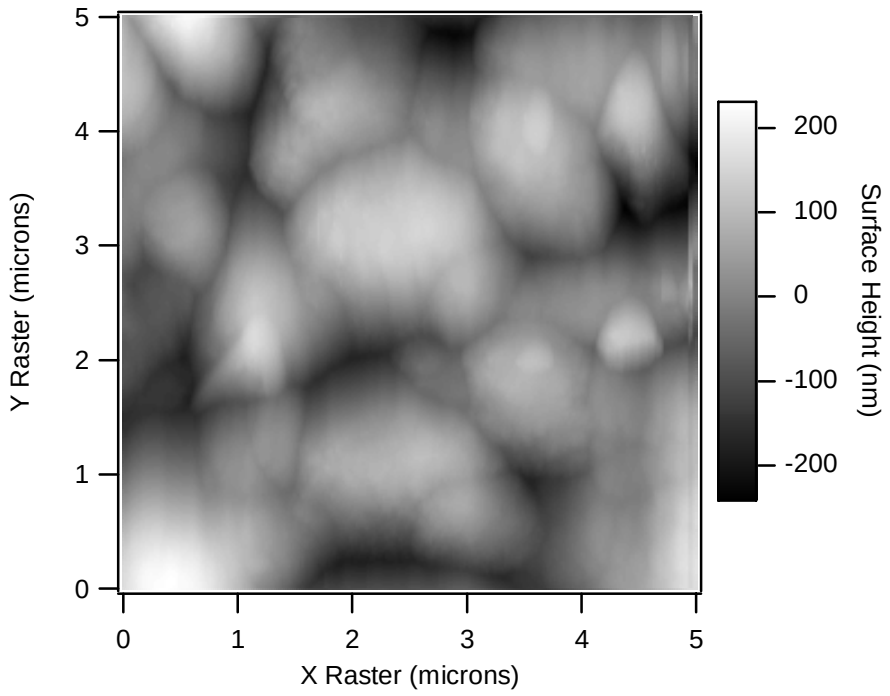

Figure 6.9: AFM scan of the carbon samples used in the present work, 5 µm × 5 µm area.

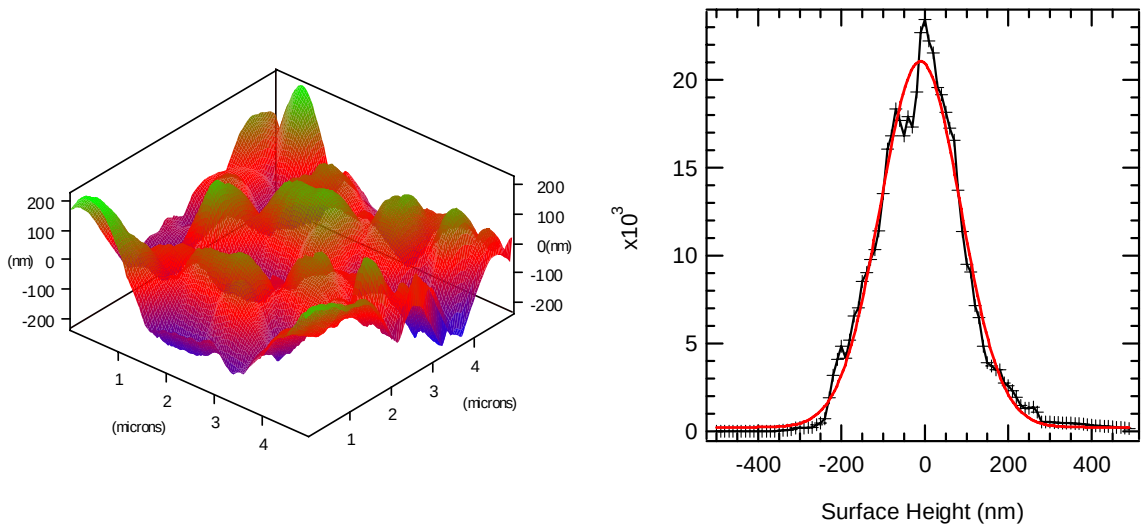

Figure 6.10: AFM scan measurements for the carbon samples used in the present work. (a) 3-D carbon sample surface height map of a 5 µm square region (b) surface height distribution function.

6.2.2 Analysis of Local Angle of Incidence

As previously discussed, one must differentiate between the local angle of incidence, α, and the overall angle of incidence, θ, when the size of the surface features is much larger than the collision cascade dimensions. The atomic force microscope (AFM) data file containing the digitized surface representation can be used to obtain "local" incidence angle information. Here we use an approach similar to that employed by Kustner (1998), where the surface grid is broken into small triangular panels. For a given triangular panel, the vertices are given by the points

$$\begin{aligned} r_1 &= [x_1, y_1, z_1] \\ r_2 &= [x_2, y_2, z_2] \\ r_3 &= [x_3, y_3, z_3] \end{aligned} \qquad \textbf{6.10}$$

Vectors defining two adjacent sides of each triangle are

$$\begin{aligned} v_1 &= r_2 - r_1 \\ v_2 &= r_3 - r_1 \end{aligned} \qquad \textbf{6.11}$$

The normal to each surface segment is then calculated:

$$\vec{n} = \left. \frac{\vec{v}_1 \times \vec{v}_2}{\|\vec{v}_1\| \cdot \|\vec{v}_2\|} \right|_{n_z>0} \qquad \textbf{6.12}$$

Requiring that $n_z>0$ ensures that all of the surface normal vectors are facing outward. Finally, the local angle of incidence is determined by

$$\alpha = \arccos\left(\frac{\langle \vec{n}, \vec{n}_b \rangle}{\|\vec{n}\| \cdot \|\vec{n}_b\|} \right) \qquad \textbf{6.13}$$

where $\mathbf{n_b}$ indicates the beam direction. The surface map shown in Figure 6.9 was analyzed in this manner. For macroscopic angle of incidence values of θ = 0º, 45º, and 60º, the local angle α distribution is given in Figure 6.11. One striking aspect of the normal incidence case is that the most probable α value does not occur when θ = 0º, but rather at ~17º. Similar behavior was also observed by Kustner from an analysis of scanning tunneling microscope (STM) measurements of graphite that had been bombarded by hydrogen. This could suggest a preferential growth angle for the carbon

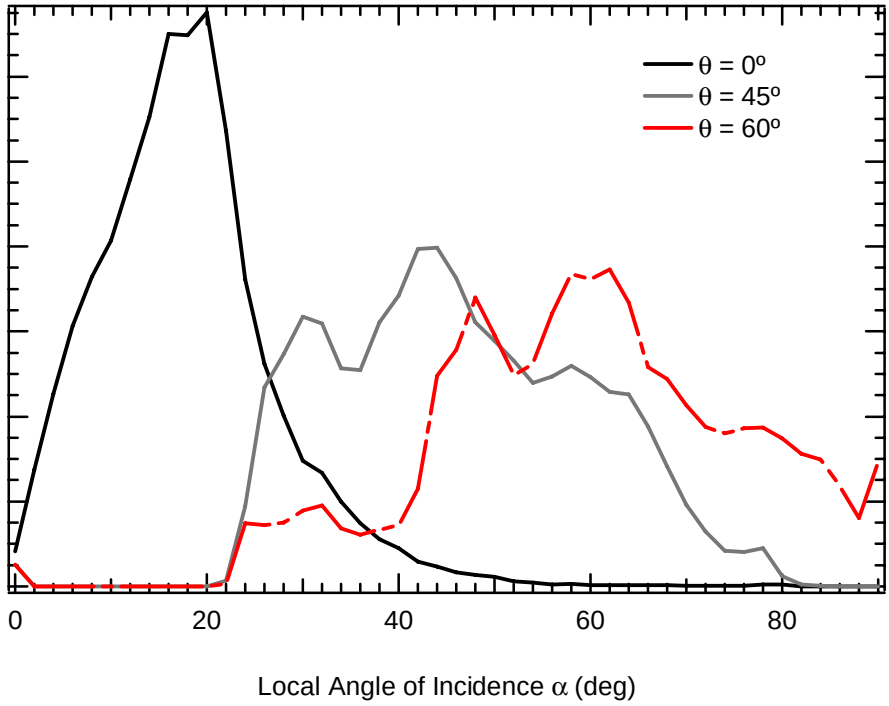

Figure 6.11: Local angle of incidence distribution, calculated from atomic force microscope measurements taken as part of the present work.

films used in this study. At higher angles of incidence this no longer appears to be the case, as the most probable value of α appears to coincide with the macroscopic incidence angle for θ=45º and 60º.

From this analysis, the importance of surface roughness is evident. Even for the relatively smooth surfaces of the target materials used here, there is a significant spread in local angle distribution. Such a distribution could be used as an input for Monte Carlo simulations such as TRIM [Ziegler, 1985] to determine the influence of surface roughness on sputtering yield. These calculations would require that shadowing and redeposition effects be accounted for accurately [Kustner, 1998] Measurements of the distributions of sputtered particles (as described in [Williams, 2004]) would be of particular benefit for this application.

6.3 Concluding Remarks

In this chapter, a number of techniques were used to model the experimentally measured Mo and C sputtering yields. When scaled by their normal incidence values, the yield data collapsed onto two distinct curves, indicating significant differences in the yield variation as a function of θ. In particular, the C data showed a much higher sensitivity to incidence angle, with $Y(\theta_{max})$ occurring at nearly glancing incidence.

To gain insight into these observations, existing transport theory models were used to calculate the relative dimensions of the range and damage distributions in two dimensions. Because sputtering processes depend on how the energy from the projectile ion is dissipated within the solid, reconstructing these distributions provides insight into how much energy has been deposited near the surface. At higher projectile to target mass ratios, the cascade shape is elongated, as was the case with C. By comparison, the transverse straggling of the distribution function was much higher for the case of Mo, indicating a nearly spherical cascade shape. In addition, transport theory solutions revealed that while collision cascade shape depends strongly on the ion-target particle mass ratio, it is not a strong function of incident particle energy. For the energy ranges of interest for electric propulsion applications, the sputtering behavior as a function of incidence angle can be considered independent of ion energy. This is particularly advantageous for extrapolating the results obtained in the present study to other energies.

For the low energies of interest in this study, the incident Xe ions do not penetrate more than 3 nm within the target surface. Most real surfaces have structures that are much larger than this, and the local angle of incidence for the ion beam may not necessarily be the same as the macroscopic angle of target with respect to the beam. Atomic force microscopy allowed the texturing of the samples used in this study to be characterized over a small area. For the carbon films analyzed here, an average surface feature height of 136 nm was found. The atomic force microscope data were used to calculate local incidence angles over the surface, indicating that the ions strike the surface over a

range of impact angles. Such information could be incorporated into computational sputtering models to determine the effect of surface roughness on the total sputtering yield. The program TRIM [Ziegler, 1985], for example, accepts a text file input allowing the user to specify the direction and energy of the incident particles. The distribution of angles calculated in Section 6.2.2 could be incorporated into such a file for use within TRIM or any comparable Monte Carlo software package.

This page has been intentionally left blank.

Chapter 7: Cathode Sputtering Measurements Using Surface Layer Activation

The previous three chapters have focused on sputtering mechanisms pertinent to ion thruster grids. In the final portion of this thesis, the emphasis now shifts to understanding cathode erosion processes. Recall that the bombardment conditions in this region of the discharge chamber have not been characterized well enough to allow for accurate modeling of cathode wear. Because of this, diagnostics aimed at characterizing the erosion rates directly would be of great benefit for predicting thruster service life.

The erosion rates of the discharge cathode keeper in a 30 cm NASA Solar Electric Propulsion Technology Applications Readiness (NSTAR) configuration ion thruster were measured using a technique known as surface layer activation. Recall that the keeper electrode consists of a Mo orifice plate electron beam welded to a Ta tube and sits just downstream of the cathode assembly. The location of the keeper in a typical ion thruster configuration is shown in Figure 7.1. The surface layer activation (SLA) diagnostic used in the present work involved producing a radioactive tracer in the keeper surface by high energy proton bombardment. This bombardment caused a small fraction of the Mo^{95} present in the orifice plate to be transmuted to a radioactive isotope, Tc^{95m}. The activity of the tracer material was monitored with a gamma spectroscopy system. When the surface was subjected to wear processes, some of the radioactive tracer was sputtered along with the rest of the material in the cathode surface, and resulting decrease in activity was correlated with a depth calibration curve to yield the eroded depth. The primary objectives of this investigation were to validate the experimental technique by reproducing erosion data from previous wear studies and to determine the effect of different engine operating parameters on erosion rate.

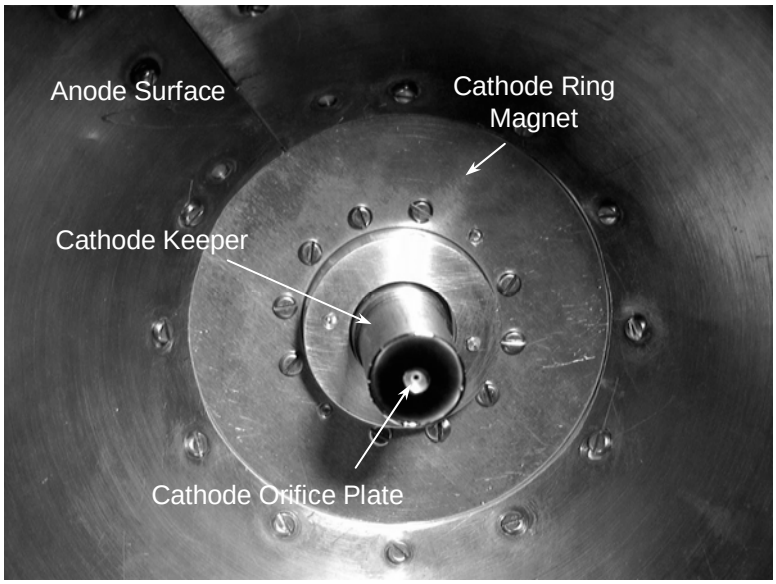

Figure 7.1: Image showing the placement of the cathode keeper withing the 30 cm laboratory model thruster developed for this study.

7.1 Summary of Experimental Technique

Surface layer activation is a sensitive diagnostic that can be used to rapidly measure keeper wear under a variety of thruster operating conditions. The general technique involves bombarding the material under consideration with a high energy ion beam produced by a particle accelerator or cyclotron. The ions colliding with the surface have a known probability of causing a nuclear reaction, which transmutes some of the target atoms to a radioactive isotope. Knowledge of the beam energy, angle of incidence, and reaction cross sections allows the activity per unit depth to be calculated. Activity is typically defined as the number of decays per second in units of Bq (1 decay/s) or Ci (3.7×10^{10} decays/s). The depth calibration is also determined directly by activating a stack of uniform foils and measuring their relative activities. Before the actual experiment is to be conducted, the activity level of the tracer material is recorded via a gamma spectroscopy system. After the test has concluded, another spectrum is recorded, and a scaling parameter between the two spectra is determined and correlated with a total mass loss.

Because of the high sensitivity of SLA, it was expected that accurate measurements could be obtained after 40 hours of thruster operation based on the erosion rates seen in previous life tests. The technique allows localized measurements to be made because only the material in the activated region is monitored. In general, the width of the activated region is limited by the beam diameter and the masking techniques used, which in this case allowed for activated bands approximately 1 mm wide. One of the most attractive attributes of this technique is the fact that the decrease in activity represents a direct measure of mass loss. The relationship between the measured signal and the erosion rates is governed by a simple depth calibration curve that is known accurately. There is no need to infer erosion rates from the densities or emission spectra of sputtered particles as is the case with many other techniques.

SLA has been used frequently in the automotive industry as a method of measuring wear rates of components in internal combustion engines [Kosako, 1991]. In this case, a $Fe^{56}(p,n)Co^{56}$ reaction is utilized, and the wear rate is measured in real time by monitoring the radioactivity of the engine oil. It has also been applied to measuring the wear of railway rails and cutting tools, the effectiveness of different lubricants, and corrosion studies [IAEA TECDOC-924, 1997]. In materials that cannot be directly activated, such as plastics and carbon composites, recoil implantation may be used [Ditrói, 1996]. In electric propulsion applications, SLA has been applied at Princeton University in magnetoplasmadynamic (MPD) thruster cathode erosion studies [Marks, 1982; Polk, 1997].

7.1.1 Activation Parameters

The activation parameters depend on the target material, the desired reaction products, and the required sensitivity. Reactions that result in tracer materials with half lives of several months are ideal for SLA applications, because the decay rate is sufficiently fast to minimize facility contamination hazards, while allowing for a reasonably long testing window. In addition, it is desirable to have only a single reaction product since multiple overlapping photopeaks require higher resolution equipment and more complex data analysis procedures. The software used to analyze the

spectra in this study is capable of resolving multiple components, although to do so, a reference spectrum for each would be required. To increase the sensitivity, the proton beam may be angled with the target surface, thereby compressing the activated region into a thinner layer. This has the effect of increasing the amount of activity per unit depth, providing higher resolution.

The cathode keepers used in this investigation were fabricated to the same specifications used for the NSTAR flight thrusters. The keeper itself consists of a 19.0 mm (0.75 in.) diameter tantalum tube with a 1.5 mm (0.06 in.) thick molybdenum orifice plate electron beam welded to the downstream end. The orifice hole diameter is 4.8 mm (0.1875 in.). To eliminate any differences in the activation profiles due to surface roughness, the downstream surface of each orifice plate was polished to a 1 micron finish. The keepers were activated by bombarding the molybdenum orifice plate with a 10.4 MeV proton beam. This resulted in two nuclear reactions that transmuted a small percentage of the Mo^{95} to the gamma-emitting technetium isotopes Tc^{95m} and Tc^{96}:

$$Mo^{95}(p,n)Tc^{95m}$$

$$Mo^{95}(p,n)Tc^{96}$$

The reaction yield for Tc^{96} is actually 60 times higher than that of Tc^{95m} [IAEA TECDOC-924, 1997]. However, because its half-life is so short, its activity drops to negligible levels after approximately 2 months, allowing the spectrum to be analyzed as though it was produced by one isotope only. High resolution Ge(Li) detector scans confirmed that the Tc^{96} contributed only minimally to the total activity measured.

Three keepers were activated, each at a different radial location based on the erosion profile that resulted from the 8200 hour test. The activated sites were circular bands concentric with the orifice, each 1 mm wide. Activating in thin bands rather than small spots (as is typically done in many industrial applications) decreased the dosage per unit area of the part, thereby decreasing the potential for radiation damage to the surface. Furthermore, this type of activation mitigated the effects of any asymmetries in the erosion pattern. A radiograph of the activated regions of the keepers using gamma-sensitive paper is shown in Figure 7.2. The gaps in the activated areas are due to the masking

technique used during the activation process. The total activity of each band was 2 μCi, 50% of which was within 30 microns of the surface. The shallow depth was achieved by angling the proton beam 60 degrees with respect to the orifice plate surface. The keeper with the smallest diameter activated ring was subjected to the most severe dose from the proton beam, at a level of 0.040 $\mu A \cdot hr/mm^2$ (1.4×10^{-4} C/mm^2). For these conditions, the ratio of number density of Tc^{95m} to Mo^{95} was calculated to be on the order of 10^{-26}.

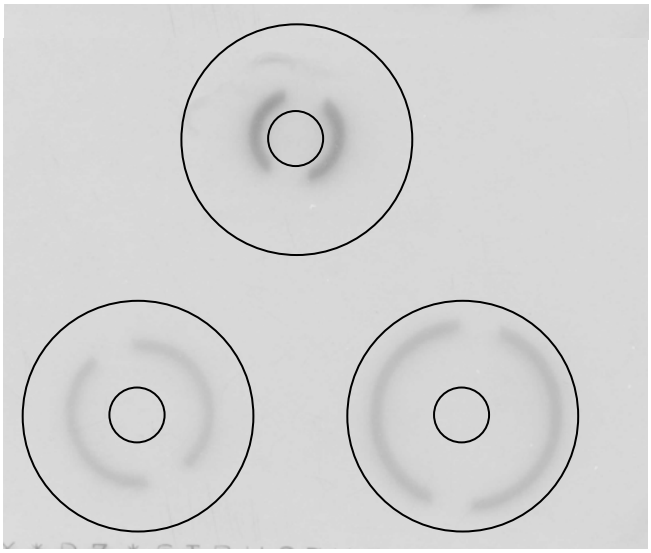

Figure 7.2: Radiograph of activated cathode keepers with gamma-sensitive photographic paper (courtesy Kenneth Oxorn, ANS Technologies). The black outlines indicate the keeper orifice geometry.

7.1.2 Calculation of Depth Calibration Curve

The depth calibration used in this study is derived from both previous experimental measurements and calculations based on reaction cross section data. The experimental method involves activating a stack of foils of uniform thickness (on the order of several microns.) The activity in each foil may then be measured in relative amounts by gamma spectroscopy. The calculated profile was produced with a software package known as TLAPrfl [Wallace, 1999]. The software utilizes existing foil stack data at known beam energies for 63 different reactions. Empirical

relationships and stopping power data from Ziegler's reference volumes (1985) are used to extrapolate to intermediate activation energies.

Figure 7.3 displays a depth calibration curve for an 11 MeV activation of Mo^{95} at normal incidence. The experimental data obtained from IAEA TECDOC-924 (1997) is displayed with the calculated profile for this case. The agreement between the foil stack data and the profile is considered to be good, especially for depths less than 50 μm. A detailed analysis of the errors associated with these curves appears in Section 7.1.5.

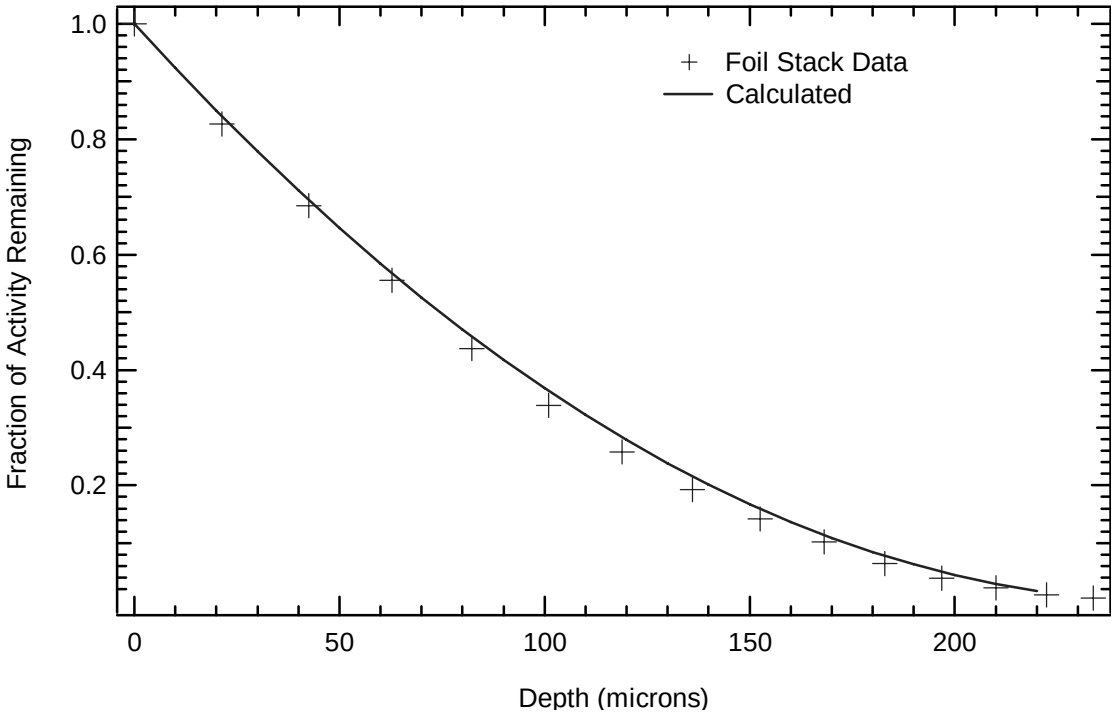

Figure 7.3: Activity vs. depth profile for 11 MeV proton beam activation of Mo^{95}.

7.1.3 Experimental Procedure

The SLA experiments were designed to minimize the turnaround time between subsequent runs and to make the conditions of each test as repeatable as possible. Prior to each test, a reference spectrum of an activated keeper was collected over a 12 hour period. Once this was completed, the keeper was mounted to a cathode and installed in a laboratory mock-up of the DS1 flight thruster.

The thruster itself remained mounted in the vacuum chamber, as it was designed to allow the cathode to be extracted easily from the back magnet ring by simply removing a portion of the plasma screen and disconnecting the propellant line and electrical leads. After the engine was reassembled, the chamber was pumped down, and the cathodes were conditioned according to the same procedures used during the ELT. Once the thruster was started, typically 20 to 30 minutes were required for its operating parameters to stabilize, after which an automated data acquisition system controlled and monitored the test conditions. After the completion of each experiment, the vacuum system was vented up to atmospheric pressure, and the above process was repeated for each subsequent experiment. A typical test could be completed by a single individual (in this study, the author), in a time frame of approximately 1 week.

Between tests, the cathodes were stored in a nitrogen purge box to prevent contamination. Once the eroded keeper was removed from the thruster, another gamma spectrum was collected and compared to the pretest reference data. Special care was taken to minimize handling keepers so as not to damage or contaminate them during this process. The only material that came into contact with the downstream surface of the keeper was a Teflon sleeve used to ensure repeatable positioning of the keeper within the detector and to prevent contamination of the detector itself. A background scan with only the sleeve in the detector was taken after each spectrum was collected to ensure that none of the radioactive material had been removed from the downstream surface.

The gamma spectroscopy system that was used to measure the activity of the samples included a NaI(Tl) scintillation detector containing a 7.6 cm by 7.6 cm cylindrical crystal. A schematic of this system is depicted in Figure 7.4. The samples were loaded in a 5.1 cm deep, 2.5 cm diameter cavity in the detector. The crystal emits a number of photons proportional to the energy of the incident gamma that it absorbs. The base of the crystal is attached to a photomultiplier tube (PMT) which generates a voltage signal based on the number of photons emitted by the crystal. The entire assembly is encased in a copper-lined lead shield to filter out background radiation. The voltage signal is processed by a multi-channel analyzer (MCA).

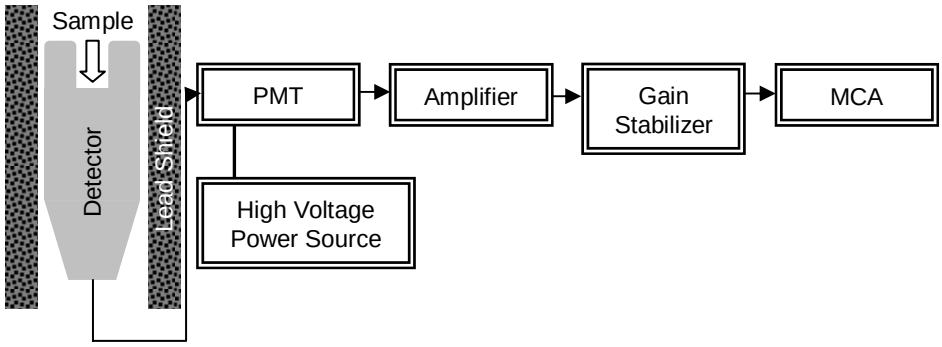

Figure 7.4: Schematic of NaI(Tl) detector setup.

To obtain high resolution scans, a Ge(Li) semiconductor detector available at the California Institute of Technology was used. The higher resolution was necessary to detect impurities in the activated samples, since the photopeaks from the contaminant isotopes were rather close to those of Tc^{95m}. Only one line from Tc^{96} could be discerned, at 849.9 keV.

A comparison of the spectra obtained with each type of detector is shown in Figure 7.5. Prominent photopeaks and half-life data are shown in Table 7.1.

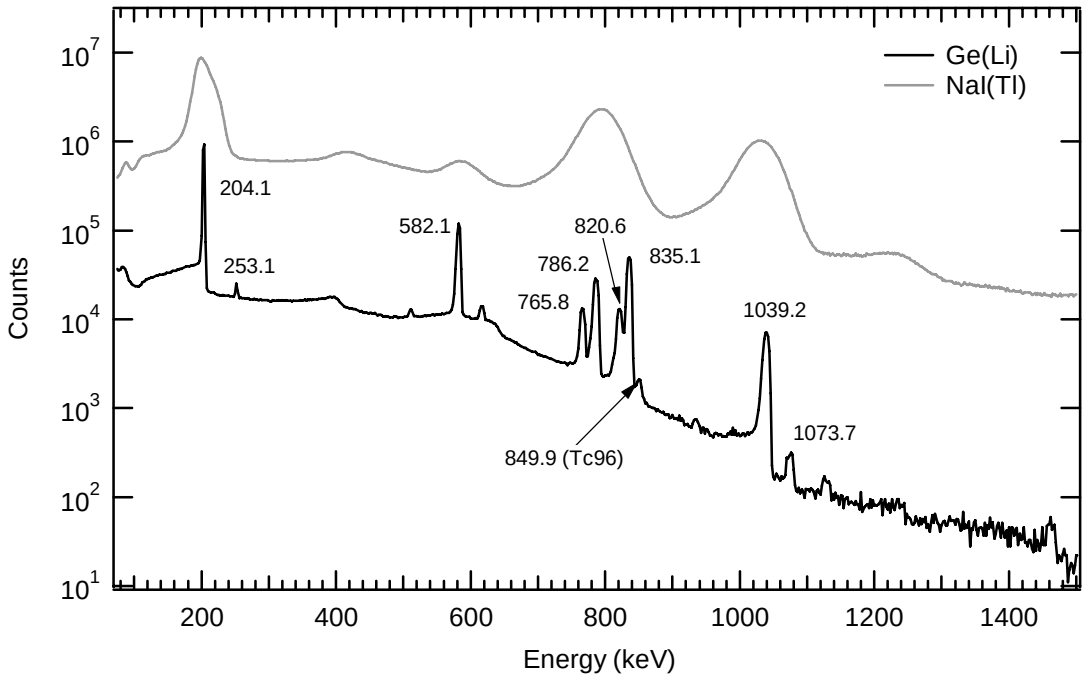

Figure 7.5: Tc^{95m} spectra scans from Ge(Li) and NaI(Tl) detectors.

Table 7.1: Properties of activated products over the range of interest of this experiment.

	Photopeaks (keV)	Half Life
Tc^{95m}	204.1, 582.1, 1039.2	58.72±0.15 days
Tc^{96}	778.2, 812.5, 849.9	4.28±0.07 days

Although the Ge(Li) detectors offer much better energy resolution, NaI(Tl) detectors were favored in this study. Because the spectrum is essentially composed of only one isotope and all of the photopeaks decay at the same rate, there was no significant penalty for using these types of detectors. Since the total activity was of primary interest here, the energy resolution of the NaI(Tl) detectors was sufficient for the purposes of correcting for gain and threshold drift, as discussed in Section 7.1.5. Furthermore, the counting efficiency of the NaI(Tl) detectors is superior to the semiconductor detectors. Hence, shorter counting times are required, enabling a faster turnaround time between tests.

7.1.4 Data Analysis

The method of resolving the scaling parameter between the gamma spectra is an iterative least squares scheme. This method has been successfully employed in the past at Oak Ridge National Laboratories to determine the concentrations of radioactive contaminants in chemical solutions [Schonfeld, 1966]. The method was later enhanced to allow for the measurement of MPD thruster wear rates [Polk, 1997].

The sample count rate in a particular channel *i* is given by

$$y_i = \frac{z_i^s}{\tau^s} - \frac{z_i^b}{\tau^b} \qquad \textbf{7.1}$$

The sample spectrum may be the composite of several reference spectra. The count rate in the reference spectrum for a particular channel *i* produced by an isotope *j* is given by

$$a_{ij} = \frac{z_{ij}^{r}}{\tau_j^{r}} - \frac{z_{ij}^{b}}{\tau_j^{b}} \qquad \textbf{7.2}$$

The relationship between the two spectra is

$$y_i = \sum_{j=1}^{h} a_{ij} m_j + \varepsilon_i \qquad \textbf{7.3}$$

The objective of the weighted least squares method is to find a solution $\hat{m}_j$ that minimizes the error term ε_i according to some weight factor matrix W_{ij}. The diagonal elements of $\boldsymbol{W}$ are generally the inverse of the count rates in each of the channels, in order to mitigate the effect of peak broadening in the experimental data. As a result, the best fit provided by the least squares method is given by

$$\hat{\mathbf{m}} = (\mathbf{a}^{\mathbf{T}}\mathbf{W}\mathbf{a})^{-1}\mathbf{a}^{\mathbf{T}}\mathbf{W}\mathbf{y} \qquad \textbf{7.4}$$

Large errors may occur if there is significant gain and threshold drift in the instrument electronics. The least squares methodology is ideally suited to correcting for such errors. Details of the implementation of these methods are described in detail by both Schonfeld (1966) and Polk (1997).

7.1.5 Error Analysis

The greatest advantage in using SLA to measure low wear rates is the high accuracy that is attainable. To ensure that this level of accuracy is achieved, a careful examination of sources of error was conducted.

Error in the scaling parameter between the sample and reference spectrum arises from statistical fluctuations in the count rate of each channel. This uncertainty is given by Schonfeld (1966) and Polk (1997):

$$\hat{\sigma}^2(\hat{m}_j) = \frac{1}{n-h}\left(\sum_{i=1}^{n} W_{ii} a_{ij} a_{ij}\right)^{-1} \sum_{i=1}^{n} W_{ii}\left(y_i - \sum_{j=1}^{h} a_{ij}\hat{m}_j\right)^2 \qquad \textbf{7.5}$$

Note that for a given channel, the statistical fluctuation is approximated by

$$\sigma^2(y_i) = \frac{y_i^s + y_i^b}{\tau^s} + \frac{y_i^b}{\tau^b} \qquad \textbf{7.6}$$

From this relationship it is clear that the two steps that may be taken to effectively reduce the variance in count rates are reducing the background count rate by surrounding the detection system with lead shielding, and increasing the collection live times. In this study, collection times in excess of 10^4 seconds were used, making statistical noise an insignificant source of error in the measurements.

The photomultiplier tube of the detection system also introduces a potentially significant error source. The PMT heats up during operation causing amplifier gain and threshold shifting. To eliminate this effect, a software gain stabilization is implemented as the spectrum is being collected. The gain is actively controlled so as to maintain a single photopeak in a specified energy window. This is sufficient to nearly eliminate threshold shifting and to hold the gain shifting to within 3%. A secondary software correction is used after the spectra are collected to completely eliminate the gain shifting. Tests of the gain and threshold shift correction methods demonstrated that this source of uncertainty does not contribute significantly to the measurement error.

The measured reduction in activity must be corrected for the natural decay of the radioisotope. This introduces another factor affecting the measurement precision, namely the uncertainty in the half life of Tc^{95m}. The published value is 61±2 days, from a study by Unik and Rasmussen (1959). This value was arrived at by a technique known as "peak stripping," which is less accurate than the least squares fitting scheme employed in this study. The half-life of a pure Tc^{95m} sample was measured as part of this study, yielding a value of 58.72±0.15 days. The improved measurement is due primarily to enhancements in the analysis method (iterative least squares) and to the fact that technetium can be more readily produced in a purer form today than when the previous study was undertaken. The half-life measurement was also used as a test for the data analysis software prior to running the actual wear experiments.

In addition, the trace amounts of Tc^{96} remaining in the activated samples during the early portion of the testing affected the count rates. Typically, the Tc^{96} contribution to the spectrum was less than 0.33% of the total number of counts. Furthermore, the short half-life of this isotope (4.2 days) made it significant only in the first two tests conducted. The error due to the decay of these contaminants is a slight overprediction of the wear rate.

The depth calibration curve was expected to be the largest source of error in the SLA measurements. Error associated with this curve arises from uncertainty in both the published experimental data at different energies and from how well the calculated calibration fits these data for intermediate energies. In the foil stack data, foil thicknesses are measured via a precision microbalance. The relative activity present on each foil is measured via a gamma spectroscopy system similar to that used in this study. The uncertainty in the foil thickness can be converted to an error in activity level, allowing it to be added to the statistical error in the activity measurement. The depth calibration curve is nearly linear for shallow depths (less than 15 microns.) To determine how well the interpolated curve over this shallow range agreed with measured data, experimental measurements from an 11 MeV activation were compared to the calculated profile. Calculations of linear fits over the range of interest indicated a worst case error in slope of ±3.5% due to uncertainty in the agreement between the foil stack data and the calculated depth profile.

There are also uncertainties introduced by the wear process itself. If the eroded depth is uneven across the activated region the perceived depth may be skewed depending on the shape of the depth calibration curve in this region, and the degree to which the erosion is non-uniform. This problem is avoided by having a uniform density distribution within the activated region, which is essentially true over the range of interest considered here.

Radiation damage is another factor that may affect the sputtering characteristics of the activated samples, although the amount that is considered to be significant is often subjective. One measure of radiation damage is the number of displacements per atom or "dpa." This may be interpreted as the number of times an atom undergoes a displacement from its lattice position during a collision

cascade. For proton activations of metallic materials, the primary mechanism by which incident particles lose energy is through interactions with the electrons in the target. For this type of interaction, the Rutherford cross section is appropriate, an approximation of which was calculated and used in this analysis. Electronic interactions dominate through most of the range of interest, and most nuclear interactions occur below 120 μm. Using the methodology presented by Schilling (1994), a dpa of 5×10^{-5} was calculated for the activations in this study, suggesting that the effects of radiation damage would be minimal.

Redeposition of sputtered material on the keeper surface is another concern because such material would be indistinguishable to the detector from the activated bands and would cause an underestimation of total wear. The fact that there is no direct line of sight from the keeper to itself makes it unlikely that sputtered products would be redeposited. To determine where most of the material was deposited experimentally, a series of witness plates were attached to different locations on the interior of the thruster discharge chamber during one of the experiments. Measurements of the activity of the material coating the plates after testing confirmed that most of the sputtered products from the keeper were deposited on surfaces near the grids. The activity accumulated on witness plates mounted near the cathode region was on the order of 10^{-6} times less than the total activity of the keeper itself, suggesting that error due to deposition in this region is negligible.

7.2 Erosion Experiments

7.2.1 Thruster Hardware

A laboratory model of the NSTAR thruster (known as the "NKO thruster") was developed for use in this investigation because contamination concerns precluded using any of the engineering model thrusters (EMTs.) Portions of the thruster discharge chamber were constructed at Caltech. The author of this thesis fabricated the cathode assemblies, the cathode ring magnet, grid mounting hardware, and outfitted the thruster for high voltage operation. The NKO discharge chamber is

aluminum, with the magnets themselves and their placement identical to those used on the flight engines. In addition, the orifice geometry of the 0.635 cm (0.25 in.) diameter laboratory model cathode was identical to those of the flight thrusters (FTs) and EMT2.

Detailed magnetic field maps of the cathode region of NKO and FT2 indicated that the field strength was accurately replicated, with the axial field strength at the cathode tip within 3.5% in NKO. The thruster was outfitted with a molybdenum grid set from a J-Series thruster. The grids were fabricated with the same hole geometry as the later NSTAR series thrusters. The grids in this study had been used in previous tests, and the hole diameter had enlarged to a maximum of 1.2 mm, which falls between the original 1.14 mm and the 1.4 mm hole size observed at the end of the 8200 hour test. The gap between the ion optics assembly and the downstream magnet ring was adjusted so that it was identical to that of FT2.

All testing was conducted in JPL's 2.5 m x 5.5 m Thruster Performance and Endurance Test Facility. The chamber itself is equipped with three cryogenic pumps, producing a base pressure of 1.1×10^{-5} Pa (8.0×10^{-8} Torr). During thruster operation, the maximum pressure was 2.7×10^{-3} Pa (2.0×10^{-5} Torr). All pressures were measured with an ion gauge calibrated for N_2. The tank pressure is divided by a gas correction factor of 2.874 to obtain the ambient pressure in xenon. The discharge chamber propellant flow rate was corrected for ingestion of ambient gas assuming free molecular flow using the measured chamber pressure. The chamber is equipped with an E×B probe and two Faraday probes. The power supply system was composed of components similar to those used on the recently completed ELT [Sengupta, 2003]. A data acquisition system also similar to that used during the ELT allowed for measurement of the thruster electrical parameters to within ±0.5%.

A preliminary test was conducted to verify that the thruster performed similarly to the DS1 ion thruster over the entire NSTAR throttle range. In general, the agreement between the NKO and FT2 values prior to life testing was good, as demonstrated in Table 7.1. Furthermore, the measured double ion fraction and keeper ion current also matched closely with those measured during an earlier series of tests with EMT4, as shown in Table 7.3.

Table 7.2: NKO vs. FT2[a] performance data over the entire NSTAR throttle range.

TH Level	J_D (A) NKO	V_D (V) NKO	J_D (A) FT2	V_D (V) FT2
0	5.06	25.45	4.64	25.97
3	5.73	26.35	5.37	27.06
6	8.10	25.00	7.42	25.37
8[b]	9.18	24.90		
12	11.70	25.19	10.83	25.17
15	14.60	24.00	14.06	24.45

[a]FT2 performance data taken as part of a performance acceptance test prior to starting the ELT
[b]Performance acceptance test data not available at TH 8 for FT2 pretest conditions

Table 7.3: NKO vs. EMT4 keeper ion current and double ion current along the thruster centerline.

TH Level	Keeper Ion Saturation Current		J++/J+	
	NKO	EMT4	NKO	EMT4
8	127 mA	121 mA	0.273	0.225
15	191 mA	187 mA	0.303	0.262

The NKO thruster's discharge parameters also fall well within the spread of values observed from wear testing of EMT2 and FT2, as well as performance testing of EMT4. This provides confidence that the NKO thruster accurately reproduces the discharge chamber environment of NSTAR thrusters. This is displayed in Figure 7.6, where the discharge parameters for these thrusters are compared with those of the NKO. The average value of each operating parameter is indicated by the triangular marker, and the extent of the maximum and minimum values obtained during long duration testing is indicated by bands when applicable.

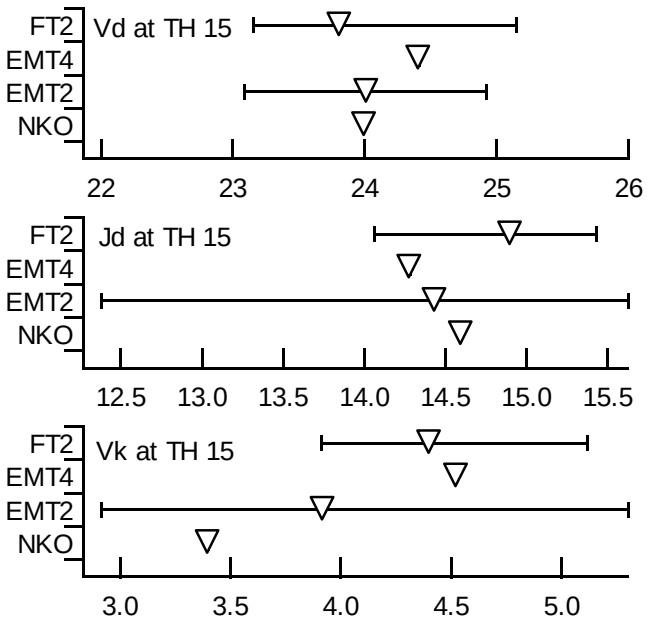

Figure 7.6: Range of discharge parameters for NSTAR configuration thrusters, including NKO (present work), FT2 [Sengupta, 2003], EMT4 (JPL laboratory tests, unpublished), and EMT2 [Polk, 1999].

Because wear rates are being measured over a rather short period of time, it is essential that the thruster operating parameters be stable for the duration of each test and that the thruster performance be reproducible with each iteration. After startup, the engine parameters generally stabilized after approximately 20 to 30 minutes of operation. The thruster appeared to perform similarly between subsequent tests, although over time the performance of the engine was noted to degrade with repeated exposures to atmosphere. Although the cathodes were reconditioned at the beginning of each test, it is suspected that the repeated exposure to the water vapor and oxygen in the air had an unfavorable effect on the cathode inserts, causing a small increase in discharge voltage and neutralizer keeper voltage with time.

7.2.2 Experimental Conditions and Results

A total of 9 tests were conducted, each between 40 and 90 hours in duration. The objectives of the first four erosion tests were to validate the SLA method as a viable wear diagnostic for ion

thrusters, and to establish the repeatability of the technique. These results are displayed in Table 7.4. Note that the location of the activated band is given as a function of the keeper outer radius, r_o.

The next five tests were aimed toward investigating the variation of wear rate due to changes in the keeper potential. The TH 8 throttle point was considered for this case, since recent life test data suggest that a short between the keeper and the cathode may have accelerated the erosion rate at these operating conditions [Sengupta, 2003]. Two methods were used to bias the keeper positive with respect to cathode potential. First, an adjustable resistor was wired in parallel with the 1 kΩ resistor that typically couples the anode to the keeper. In subsequent cases, the keeper was biased positive with a 0-30V power supply. Results from tests conducted at four different keeper potentials are shown in Table 7.5. Data from two tests that were conducted with the purpose of establishing the erosion profile at this throttle point are shown in Table 7.6.

Table 7.4: TH 15 erosion rate test results.

r / r_0	Test Duration (hrs)	8200 Hour Erosion Rate (μm/hr)	Measured Erosion Rate (μm/hr)	Mass Loss Rate (μg/hr-mm^2)	V_D (V)	V_{CK} (V)
0.341	70.9	0.0387	$0.0546^{+0.0022}_{-0.0028}$	$0.562^{+0.023}_{-0.028}$	23.86±0.24	3.39±0.10
0.540	80.4	0.0629	$0.0853^{+0.0033}_{-0.0053}$	$0.877^{+0.034}_{-0.054}$	24.07±0.21	3.32±0.17
0.735	74.8	0.0508	$0.0589^{+0.0024}_{-0.0026}$	$0.605^{+0.025}_{-0.027}$	23.92±0.15	3.51±0.10
0.735	51.8	0.0508	$0.0540^{+0.0023}_{-0.0023}$	$0.555^{+0.024}_{-0.024}$	24.15±0.25	3.29±0.33

Table 7.5: TH 8 erosion rates with different keeper potentials.

r / r_0	Test Duration (hrs)	Measured Erosion Rate (μm/hr)	Mass Loss Rate (μg/hr-mm^2)	V_D (V)	V_{CK} (V)
0.341	76.0	0.0311± 0.0014	0.320± 0.014	25.42±0.22	7.88±0.14
0.341	86.5	0.0349± 0.0014	0.359± 0.015	25.43±0.13	6.04±0.06
0.341	39.7	0.0401± 0.0017	0.412± 0.018	24.72±0.19	2.48±0.06
0.341	44.7	0.0538± 0.0023	0.553± 0.024	24.76±0.24	0 (Shorted)

Table 7.6: TH 8 erosion profile test results.

r / r_0	Test Duration (hrs)	Measured Erosion Rate (μm/hr)	Mass Loss Rate (μg/hr-mm^2)	V_D (V)	V_{CK} (V)
0.341	39.7	0.0401± 0.0017	0.412± 0.018	24.72±0.19	2.48±0.06
0.540	44.5	0.0291± 0.0013	0.298± 0.014	24.69±0.22	2.57±0.10

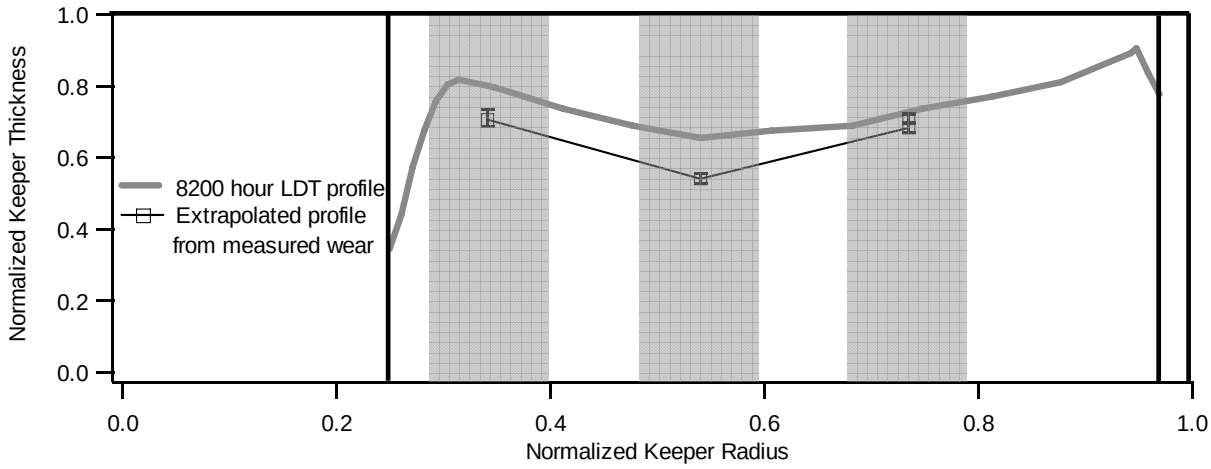

Figure 7.7: Extrapolated erosion profile after 8200 hours of operation at TH 15. The LDT profile (from [Polk, 1999]) is included for comparison.

7.3 Discussion

7.3.1 Replication of LDT Wear Rates

The erosion rates measured by the SLA technique at TH 15 agree well with those calculated from the 8200 hour keeper profile. A comparison of the LDT profile and the extrapolated wear after the same amount of time based on the SLA measurements is shown in Figure 7.7. The gray regions denote the location of the activated bands. The profile shape from the LDT has been accurately reproduced, with the magnitude of the erosion rates measured to be 7% to 41% higher. After the tests were completed noticeable texturing of the keeper surfaces was observed, as shown in Figure 7.8.

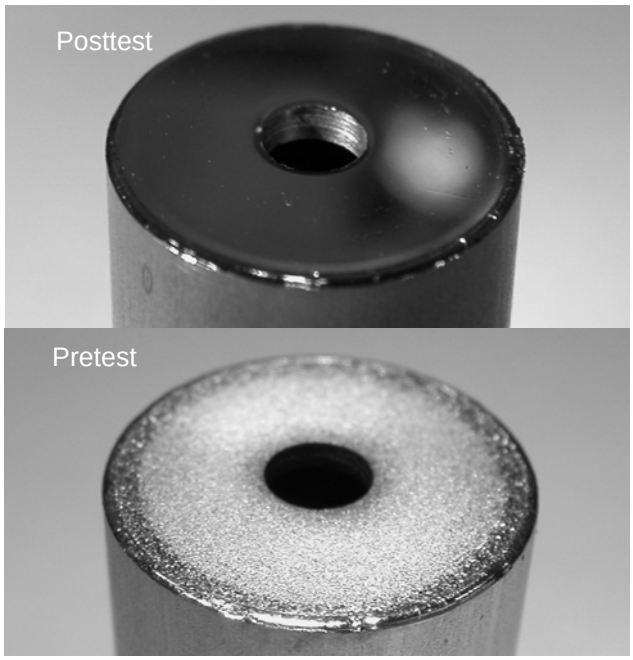

Figure 7.8: Downstream keeper surface before and after 70 hours of operation at TH 15.

In order to properly interpret the SLA results, it is important to note that the LDT profile represents the erosion rates integrated over the entire 8200 hour duration of the test. As shown in Figure 7.6, the discharge voltage of EMT2 varied between 23.1 V and 24.9 V, the keeper voltage varied between 2.9 V and 5.3 V, and the keeper erosion rate also changed as a function of time. During the short duration of the SLA experiments, the performance of the NKO thruster was representative of the performance of NSTAR thrusters, but may not correspond to the "averaged" operating conditions of EMT2 during the LDT. This does not indicate that the wear rates predicted by SLA are unrealistic, but suggests that the SLA measurements are a "snapshot" of what the erosion rates in EMT2 were for a particular set of operating conditions. This is inherently true of all short-term wear diagnostics and is not a specific flaw associated with the SLA technique.

For the purpose of establishing margins on thruster component life, extensive life testing has been the technique of choice in the past. However, such wear testing has produced differences between tests, even when conditions are carefully controlled. For example, posttest analysis of the keeper

from the 1000 hour wear test indicates a maximum erosion rate of 0.070 μm/hr, 11% higher than the maximum measured during the LDT [Polk, 1996], [Domonkos, 2001]. Both tests included engineering model thrusters very similar to each other in construction, run under the same operating conditions. The author suggests that if long duration testing is not feasible, the SLA technique can provide results of comparable accuracy in a much shorter time frame. SLA may also be used to evaluate the sensitivity of erosion rates to different thruster operating parameters, another topic addressed by this investigation.

7.3.2 Repeatability

It was desirable to examine the repeatability of results between the beginning of the test cycles to the end. As previously mentioned, small changes in thruster performance were noticed after repeated exposures to atmospheric pressure between tests and could affect the erosion rate of the keeper. A test of the keeper activated at r/r_o=0.735 for the TH 15 setting was conducted twice. The measured wear rates correspond closely with each other (to within 9%) and the calculated error bars for these points overlap.

7.3.3 Sensitivity of Erosion Rate to Keeper Potential

It was suspected that the keeper voltage substantially influenced the erosion rate, based on observations from the ELT. The energy of an ion that falls through the sheath between the discharge plasma and the keeper at a potential V_{CK} with respect to the cathode is dependent on the voltage difference between the discharge plasma and the cathode keeper. It is reasonable to conclude that increasing the keeper voltage will reduce the ion energies at the keeper surface, thereby decreasing the erosion rate.

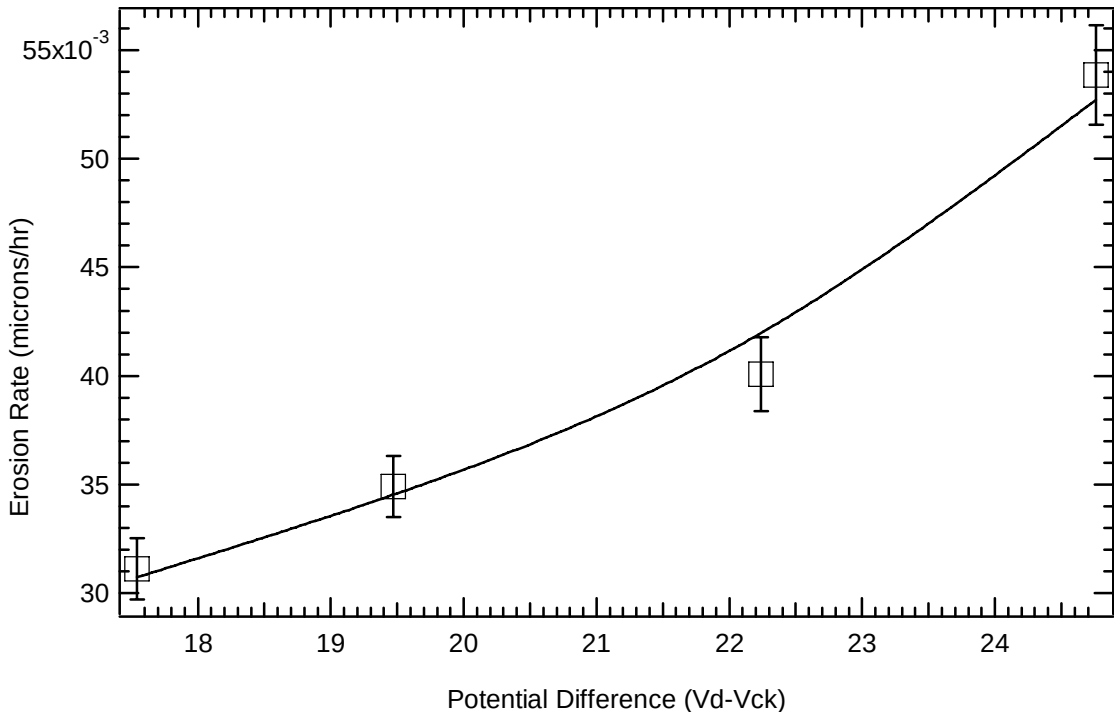

Figure 7.9: Erosion rates as a function of keeper potential at the TH 8 throttle setting for the r/r_o =0.341 position.

Four tests of the inner activated region were conducted at the TH 8 throttle point, with the keeper biased to different potentials. The results from this analysis are displayed in Table 7.5 and Figure 7.9. When the keeper is shorted to cathode the erosion rate increases significantly and is comparable to the TH 15 nominal case at the same position. Increasing the keeper potential with respect to the cathode reduces the erosion rate monotonically. This was accomplished by decreasing the resistance between keeper and anode, allowing it to float at a higher potential with respect to the cathode. Applying a bias voltage of nearly 8 V decreases the erosion in the measured region to 0.0311 μm/hr.

7.3.4 Variation of Erosion Rate with Throttle Level

Two tests at TH 8 were aimed at measuring the variation in the wear profile with distance from the keeper centerline. The data from these tests are shown in Table 7.6 and in Figure 7.10. Erosion data with the NKO thruster at this operating point display two important attributes. First, the wear

rates appear to be less overall at the lower throttle level than at TH 15. In addition, a different wear profile is shown with the most severe wear near the orifice.

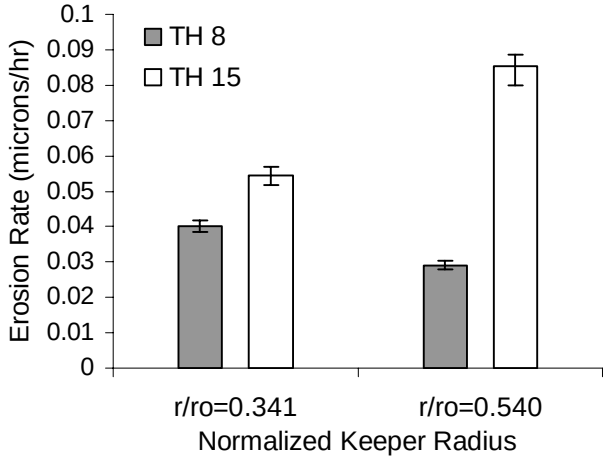

Figure 7.10: Comparison of keeper downstream surface erosion rates for TH 8 and TH 15.

The tests conducted in this investigation indicate that the measured wear at TH 8 is insufficient to have caused the rapid destruction of the keeper during the ELT. From the values obtained here, it is predicted that just over 50% of the orifice plate would have been eroded after 15000 hours of operation at the ELT throttle levels. However, ELT photographs display complete wear-through at this position for the same amount of time. The wear rates along the orifice wall were not measured in this study, and could be substantially greater than those on the downstream face. An additional activation of the keeper orifice was attempted in a later study, the results of which are discussed in Appendix B. However, due to technical difficulties associated with the test facility, these experiments were unable to conclusively address the problem of keeper orifice erosion.

The data obtained from the wear tests suggests possible courses of action for reducing the keeper erosion rate. Biasing the keeper with respect to cathode common could significantly enhance keeper life. This would a cause a slight decrease in total thruster efficiency resulting from the additional power required to operate the keeper bias supply. With a 7.50 V bias applied to the keeper, 0.372 A of current was used for a total power consumption of 2.79 W. Another course of action would be to

fabricate the keepers from materials with lower sputtering yields, such as carbon. Recent success in wear testing cathodes outfitted with carbon keepers suggests that this is a feasible option [Hayakawa, 2002].

7.4 Concluding Remarks

The surface layer activation method was validated in this investigation by reproducing the wear pattern observed in the 8200 hour LDT at TH 15. The TH 8 erosion profile was found to differ significantly from the TH 15 profile. At TH 8, the wear is greatest near the orifice, as compared to the TH 15 condition, where the wear is largest near the middle of the profile. In addition, at the nominal TH 8 case, the erosion rates were significantly less than at TH 15.

Keeper potential appears to have a significant effect on the erosion rate. Four tests conducted at TH 8 indicate that the erosion rate increases significantly when the keeper is shorted to cathode. Furthermore, biasing the keeper to a higher positive voltage can be used as a technique to combat erosion.

Wear tests on a laboratory model thruster produced erosion data for 8 different operating conditions, each after only 40 to 90 hours of operation. Evaluation of this number of conditions using conventional long duration testing would have required thousands of hours of operation. Tests similar to these could be applied in future propulsion projects to accurately measure the erosion rates of cathode and grid components. Such measurements could be used to identify potential life limiting phenomena, validate models of wear processes, and help qualify engines for the required service life.

This page has been intentionally left blank.

Chapter 8: Conclusions

Ion propulsion systems offer higher efficiencies and specific impulses than more conventional chemical thrusters, making them an enabling technology for many ambitious robotic spacecraft missions requiring large ΔVs. Their low thrust requires reliable operation over long periods of time, making thruster service life assessment of great importance. Damage to critical components by sputtering is a serious concern, and a better understanding of thruster erosion mechanisms is necessary to develop models that predict propellant throughput capability. In this study, these fundamental processes responsible for damage to ion thruster components were investigated both experimentally and from a theoretical standpoint.

Long duration ion thruster testing has shown that the discharge cathode and ion optics assembly are susceptible to damage by energetic particle bombardment. Such testing, however, is a costly and impractical way of determining the dependence of wear rates on different operating conditions. As a result, recent experimental and modeling efforts have emphasized the characterization of the pertinent plasma bombardment conditions. Applying these results to a calculation of material removal rates depends on the availability of accurate sputtering data for the conditions of interest. Such data are sparse however, because the grids and discharge cathode are fabricated from sputter-resistant materials such as molybdenum or carbon, and the bombarding ions typically have energies less than 500 eV. For grid wear, the ion angle of incidence is also important, and this effect is poorly modeled by most transport theory and Monte Carlo approaches. This suggests the need for both additional experimental data and models to enhance the present sputtering database for heavy ion bombardment at low energies.

Damage to ion thruster grid apertures was addressed through a series of low energy sputtering experiments. Sputtering yields were measured at grazing incidence to simulate bombardment of the ion optics surfaces by charge exchange ions. The experimental method involved the use of an ion

beam to etch a quartz crystal microbalance coated with the desired target material, allowing measurements to be taken up to 80º from the surface normal. This method was capable of detecting changes in mass as small as 5×10^{-9} g. The energy range of the incident ions was varied between 80 eV to 1 keV. The metallic thin films were prepared by sputter deposition and were coated to a thickness of up to 8 μm. The target materials were characterized using SEM and x-ray diffraction to ensure that they accurately approximated the bulk materials of interest. To validate the experimental method, sputtering yields of Mo, Cu, and W under Xe^+ and Ar^+ bombardment at normal incidence were compared with published literature values. For Xe^+ ions incident on a Mo target at varying angles θ from the surface normal, the sputtering yield increased according to a $\cos\theta^{-5/3}$ dependence predicted by transport theory results up to 40º. Sputtering yields increased by a factor of 1.6 over this range. The optimum angle for sputtering was found to be 55º, after which the yields rapidly decreased.

The quartz microbalance technique was also used to characterize carbon materials that have been incorporated into more advanced ion thruster designs. In general, measurements of carbon sputtering yields are prone to error when compared to metallic materials due to much lower etch rates and increased susceptibility to chemical etching due to gas impurities. A number of techniques were developed to address these concerns. The carbon films for the QCMs were produced with a low temperature sputter deposition process developed at the University of California, San Diego, to create coatings that approximated the density of the bulk material. The crystal structure and surface topography were analyzed with Raman spectroscopy and SEM imagery. Measurements of carbon sputtering yields were made for $0º\leq\theta\leq80º$ under Xe^+ and Ar^+ bombardment. Over this range, an increase in C sputtering yield by a factor of 4.8 was observed, with $Y(\theta_{max})/Y(0)$ occurring at 70°. Yield measurements at normal incidence showed satisfactory agreement with published values from previous studies.

Two different approaches were used to model the experimental sputtering yield results. First, the dimensions of the range and damage distributions relevant to ion thruster applications were evaluated

using existing transport theory models. Use of a 2-D point source solution to Boltzmann's equation revealed the importance of projectile to target mass ratio to the transverse width of the collision cascade. A higher sensitivity to angle of incidence is expected for cases where the ratio of longitudinal range to transverse straggling is large. The second approach modeling approach was to evaluate the effects of surface roughness using existing Monte Carlo codes. The surface roughness of the samples used in this study was assessed using atomic force microscopy to obtain distributions of feature heights and local angles of incidence.

For the case of cathode wear, the plasma bombardment conditions have not been characterized with a sufficient level of accuracy to allow cathode wear rates to be accurately determined. As a result, a sensitive diagnostic known as surface layer activation (SLA) was used to address cathode sputtering directly. This diagnostic technique involved producing a radioactive tracer in the cathode surface by high-energy proton bombardment. The decrease in activity of the tracer material could be correlated to an eroded depth once the surface was exposed to a plasma environment. The activated cathodes were tested in a 30 cm xenon ion thruster over a range of throttle points, providing insight into the plasma bombardment conditions in this region of the discharge chamber. The erosion profile at the TH 15 (2.3 kW) setting observed during the 8200 hour life demonstration test was reproduced with a measured maximum erosion rate of 0.085 μm/hr. Testing at the TH 8 (1.4 kW) setting demonstrated that variations in keeper voltage had a significant effect on the erosion, with a positive bias with respect to cathode potential decreasing the wear rate significantly. Measurements were achieved after operating times of 40-90 hours, with a typical uncertainty of ±0.003 μm/hr.

8.1 Additional Contributions

At the time the work described in this thesis was initiated, no experimental apparatus was in existence at JPL for performing sputtering yield measurements or surface layer activation measurements. Because of this, much of the experimental hardware described in this thesis was designed and fabricated by the author specifically for the tests described in this document. In

particular, this included building the apparatus used to obtain the sputtering measurements. This involved refurbishing a UHV chamber, as well as selecting and installing the pumps required to achieve base pressures in the 10^{-10} torr range. In addition, the sample manipulator, Faraday cup, and QCM holders were designed and constructed by the author. While the ion source was a commercially available model from Kimball Physics, the external deflection plates used to filter the beam represented a customized modification. The author also programmed all of the data acquisition software.

The surface layer activation tests required the use of a laboratory model thruster which was capable of simulating the discharge properties of the flight thrusters used on Deep Space 1. A significant effort was devoted to the fabrication of the NKO thruster for this purpose by the author of this work. The discharge chamber of the laboratory model thruster had originally been constructed at Caltech as part of an Ae 104 (Experimental Methods) course. However, the thruster had not been outfitted for use at high voltage and included cathodes which were not similar in geometry to the flight models. The author of this thesis addressed these problems by designing and fabricating laboratory model discharge and neutralizer cathodes. The magnetic field of the NKO thruster was also modified by the author (including the design and fabrication of a new cathode magnet ring and pole piece.) In addition, a significant portion laboratory power system and high voltage wiring needed to operate the thruster with beam extraction was constructed as part of this thesis.

8.2 Implementation of Sputtering Measurements in Computational Models

In addition to providing enhanced insight into the physics of sputtering at glancing incidence, the yield measurements obtained as part of this work may be incorporated into computational models to allow for improved estimates of thruster life. In Chatper 2, the CEX2D and CEX3D grid erosion codes were discussed in detail. As previously mentioned, these codes simulate the charge exchange

(CEX) processes which occur in the apertures of ion thruster grids and calculate the energies and fluxes of ions to the grid surfaces. The ion fluxes may be related directly to a material removal rate using the expression below:

$$\frac{dm}{dt} = n_t M_t = Y(E,\theta) n_i M_t$$

Note that $Y(E,\theta)$ denotes the sputtering yield as a function of energy and incidence angle. In the above equation, the change in mass of the target, dm/dt, depends on the flux of incident ions, n_i, and the atomic mass of the target material M_t. Since n_i is provided as part of the CEX2D output and M_t of the grid material is known, the sputtering yields are the final component needed calculate the mass loss of the target. (Alternately, if the density of the target material is known, dm/dt may be converted to a rate of thickness change.)

In Chapter 6, it was noted that when the sputtering yields for a particular ion-target combination were normalized to their values at perpendicular incidence, measurements taken at different energies collapsed onto a single curve. This characteristic is particularly useful for implementation in a computational model, because a simple curve or spline fit may be applied to the normalized data to account for the variation in yield as a function of incidence angle. The absolute yields may then be calculated by incorporating the energy dependence of the normal incidence data.

Prior to this study, accurate sputtering yield data for Xe^+ incident on Mo and C at varying angles of incidence was not available in the published literature. This led to a large uncertainty in ion thruster grid life calculations because the codes were forced to rely on unreliable sputtering yields estimates at large angles. For example, in the CEX2D grid simulation code, the same functional form for the sputtering yields was assumed for all ion-target combinations [Brophy, 2002]. A peak sputtering yield occurring at an incidence angle of 45° from the surface normal was assumed, with the maximum ratio of $Y(\theta)/Y(0)$ being approximately 1.6. This approach is seriously flawed for a number of reasons. As shown in Chapter 6, one of the most important factors which influences the sputtering behavior is the ion-target combination (or more specifically, the atomic mass of the incident and

recoiling particles.) The assumption of the same dependence of Y on θ for all ion target combinations is clearly a gross simplification in this case. In addition, as observed in Chapter 5, the variation of carbon sputtering yields as a function of angle of incidence is much greater than the assumed functional form. For carbon, $Y(\theta)/Y(0)=4.7$, which is much larger than the value of 1.6 assumed by CEX2D. Use of the original functional form will underestimate the mass loss by carbon grids by a factor of 3 for near grazing incidence, resulting in an over-prediction of thruster life. For this reason, it is expected that the sputtering measurements obtained in this thesis would result in a significant improvement in predictions of ion thruster life, especially for the case of carbon ion optics.

Another aspect of grid wear which must be taken into account by computational models is the gradual change in aperture geometry during operation. Observations from prior endurance testing indicate that this process does not occur linearly with time [Sengupta, 2003]. Because the accelerator grid holes become enlarged due to sputtering damage, their transparency to neutral propellant atoms increases. An increase or decrease in the neutral density in the region between the grids would influence the CEX ion production rate. Since most grid codes calculate the erosion rates for only a static configuration [Brophy, 2002; Anderson, 2004], a time-stepping algorithm may be necessary to account for gradual geometry changes.

8.3 Future Directions

From the previous discussion, it is clear that one of the major results from this work has been the application of sensitive diagnostic techniques to aid in the understanding of sputtering processes. This brings to light a number of other applications that would be beneficial to thruster development. An area of active research is the effects of thruster plumes on spacecraft surfaces. Energetic ions produced in the thruster beam have the potential to damage spacecraft solar arrays and contaminate sensitive instruments with sputtered particles. In addition, there is strong interest in the sputtering behavior of insulators used in Hall thrusters. With relatively minor modifications, the sputtering

setup developed in this study could also be applied to an investigation of the sputtering behavior of these materials.

A topic of immediate interest for the SLA technique would be a thorough investigation of keeper orifice wear. An experimental approach and some preliminary results are discussed in Appendix D. A systematic examination of the variation of keeper wear with changes in the orifice geometry and cathode flow rates would be of particular interest. Such work would also complement other experimental and computational work presently underway at JPL.

SLA can also be applied to non-metallic materials such as carbon. While carbon cannot be activated directly, recoil implantation of Be^7 can be used as an alternate method of introducing a tracer material into the surface. This type of technique would be especially beneficial as a method of assessing sputtering effects associated with carbon thruster components geared toward longer thruster life.

This page has been intentionally left blank.

Appendix A: Transformation to Beam-Centered Coordinates

The analysis of a planar ion source allows range and damage distributions to be calculated as a function of one spatial variable, depth. The distributions are expressed in terms of spatial moments using an Edgeworth expansion. To construct the damage and range distributions in two dimensions, a point source is considered. However, it is not necessary to solve the Bolzmann transport equation using the new coordinate system, as several transformations exist to allow the spatial moments for the 1-D case to be converted to the beam-centered coordinate system of the 3-D case. Winterbon (1970) discusses this method in detail for conversions to 3-D rectangular, cylindrical, and spherical coordinates. For the purposes of analyzing the transverse straggling, the transformation to rectangular coordinates is of the most interest. Following the nomenclature of Winterbon (1970) the desired moments for the point source geometry are of the form:

$$f_{n,2m,2l} = \int dXdYdZX^{n}Y^{2m}Z^{2l}F(\vec{r})$$

A relationship devised by Berger and Spencer (1959) allows the moments, *f*, to be expressed in terms of the 1-D moment coefficients, *A*:

$$f_{n-2m,2m,0} = \frac{1}{\binom{n}{2m}} \sum_{l=0}^{\lfloor n/2 \rfloor} (2n-4l+1) A_{n-2l}^{n} \beta_{nml}$$

where

$$\beta_{nml} = \frac{1}{2^{n-2l}} \sum_{k=k_o}^{\lfloor n/2 \rfloor} \binom{k}{m} \frac{(-1)^{k-l}(2n-2l-2k)!}{(k-l)!(n-l-k)!(n-2k)!}$$

and k_o=*m* or *l*, depending on which is larger.

Appendix B: Cathode Keeper Orifice Wear Measurements

The results of the SLA measurements discussed in Chapter 7 suggest that the keeper erosion on the orifice plate downstream surface was insufficient to have caused the rapid wear observed during the ELT. A set of measurements aimed at characterizing orifice wear were conducted. Due to technical issues associated with the thruster and experimental facility, only a limited number of measurements were taken. The results from this are therefore considered to be inconclusive and are included to supplement the discussion of Chapter 7.

B.1 Activations

Surface layer activation (SLA) is ideally suited for characterizing orifice wear because of its capability of providing localized measurements. By masking the downstream surface of the keeper, the orifice itself may be selectively activated. The same activation scheme for the work of Chapter 7 was also used here. As before, a 10 MeV proton beam bombarded the orifice wall to create the radioactive tracer. This reaction converted the molybdenum target atoms to a technetium isotope, Tc^{95m}, according to the reaction $Mo^{95}(p,n)Tc^{95m}$. In this process, the molybdenum atom essentially absorbs a proton and emits a neutron. The activity of the samples at the start of testing was approximately 1μCi. The beam angle of incidence was adjusted to compress 50% of the activity into a 30 μm depth near the surface. Tc^{95m} is a gamma emitter, and a NaI spectroscopy system was used to measure the activity of the samples.

The keeper used in this study was fabricated at JPL and is shown in Figure B.1. Since most of the activity is contained in a small region near the surface, the condition of the orifice wall is an important consideration for this experiment. During the machining process, the orifice was reamed 0.010 in. smaller than desired. To ensure that the orifice hole was a perfect cylinder, the hole was

Figure B.1: Cathode keeper with polished orifice hole wall.

then ground to the finish diameter. This also had the effect of reducing the average surface roughness to approximately 0.4 μm. A final polishing process left the surface with an average roughness of 0.2 μm. The polishing process introduced a slight radius of curvature to the edge of the orifice. It is estimated that this curvature was less than 0.013 mm (0.0005 in.) A sharp corner was necessary to allow the downstream face to be completely masked, allowing only the orifice to be activated.

B.2 Thruster Hardware and Test Chamber

Because one of the objectives of this thesis was to compare the measured erosion rates on the orifice wall with those obtained on the downstream surface in Chapter 7, it was desirable to reproduce the test conditions of the earlier work as faithfully as possible. As much of the original hardware was used as was feasible, including the thruster discharge chamber (NKO1) and cathode assembly. The most significant difference between test runs was the ion optics assembly. Previously, a molybdenum grid set from a J-Series mercury ion thruster had been used. This series of thrusters was developed at Hughes Research Laboratories in the late 1970s and early 1980s, and many characteristics of the NSTAR thruster were inherited from this design. As such, the grid dimensions from the two programs were quite similar, with only minor differences. Details of the J-Series program and on the

ion optics assembly are discussed by Maloy (1981) and Aston (1987). The differences between the specific ion optics sets used in this study are given in Table B.1.

Table B.1: Grid Set Characteristics.

	J-Series	NSTAR
Grid Gap, mm	0.61	0.66
Accel. Grid Thickness, mm	0.38	0.51
Hole Diameter, mm	1.20	1.14

All other modifications to the hardware since the completion of the previous work have been superficial in nature. A set of probes had been added to the discharge chamber for another series of experiments. For this experiment, the probes were removed, and the probe holders were covered. In addition, minor modifications to the ground screen were made and a new neutralizer assembly was used. None of these changes were expected to have a significant influence on the testing results.

The tests were conducted at JPL in a 2.5 × 5.5 m vacuum facility. The chamber was capable of achieving a base pressure in the 2.7×10^{-5} Pa (2.0×10^{-7} torr), and a working pressure of 8.0×10^{-4} Pa (6×10^{-6} torr) during thruster operation at TH 8. The ion gauge for this system was calibrated for Xe gas. A computer-based data acquisition system was used to continuously monitor and control the thruster operating parameters. The feed system was capable of regulating the propellant mass flow rate to within 3% of the desired set-point.

B.3 Results

Two orifice erosion tests were conducted, each at the TH 8 operating condition. Both tests were approximately 40 hours in duration. Because the keeper was intermittently shorted to the cathode during the ELT, the same condition was reproduced during the second test to examine this effect. The first test was conducted at the nominal TH 8 condition, with the keeper tied to the anode through a 1 kΩ resistor. Table B.2 displays thruster performance data from each of these tests. The measured erosion rates and corresponding mass loss rates for these two tests are given in Table B.3.

Table B.2: Thruster Operating Conditions.

Test #	Location	J_D, A	V_D, V	V_{CK}, V
1	Orifice	9.22±0.45	25.46±0.90	2.78±0.39
2	Orifice	9.34±0.43	25.92±0.54	0 (shorted)

Table B.3: Measured Erosion Rates.

Test #	Location	Test duration, hrs	Erosion rate, μm/hr	Mass loss rate, μg/hr·mm^2
1	Orifice	39.8	0.0355±0.0010	0.362±0.010
2	Orifice	45.0	0.0584±0.0013	0.595±0.014

Slight differences in thruster performance may be noted from the previous and most recent measurements. In particular, the discharge voltage increased between 0.6 V and 1.2 V. The keeper voltage was also higher for the nominal TH 8 case, by approximately 0.3 V. The potential difference between keeper and anode has been shown to affect the wear rate. However, these variations are still within the expected range for an NSTAR type thruster, and a realistic comparison with previous results is still possible. Such increases in voltage over a long time period are not uncommon and are likely caused by repeated exposure of the cathode inserts to the atmosphere.

For the nominal TH 8 operating condition, the orifice wall wear was approximately 73% of the downstream wear measured closest to the orifice. The orifice wall wear was 6% larger than the downstream wear for the shorted case.

After the first TH 8 test, the downstream edge of the polished orifice surface was significantly textured due to sputtering. This texturing gradually became lighter until the upstream edge, which showed very little damage. This indicates that the wear was non-uniform over the orifice wall, and the values given in Table 4 are averaged over the entire surface. This does suggest, however, that prolonged operation at TH 8 would result in chamfering of the orifice. Such an erosion pattern is supported by photographs from the ELT.

Numerous problems were encountered with running the thruster at higher throttle levels for prolonged periods of time. The discharge voltage and current drifted significantly over the course of

a 40 hour operating period. A high recycle rate at these throttle levels hampered efforts to obtain stable operation as well. Similar problems were encountered while running NKO2 in the same chamber, which implies that these issues have arisen due to facility related problems. Thus, at the present time, erosion measurements could only be made at TH 8 (and lower throttle levels).

With the combination of the orifice wall and downstream surface erosion rates, it should be possible to compare the wear rates obtained in the present paper with the results of the ELT. By 10451 hrs (when operation at TH 8 was completed), the orifice diameter had opened up to 0.987 cm (0.385 in.) The total mass loss corresponding to a complete wear-through of this region amounts to 0.892 g. For comparison with measurements obtained here, a scaled version of the keeper erosion profile from the LDT is assumed for the TH 15 operation up to 4937 hrs, and erosion data obtained in the present paper and Chapter 7 is used to calculate the contribution from operation at TH 8. These erosion rates predict a total mass loss of 0.365 g in this region, significantly less than that observed during the ELT. It is clear that further interpretation of the data given in Table B.3 is required in order to make such an analysis, due to the significant changes in geometry experienced by the keeper orifice plate during testing. The assumption that the plasma conditions which create the erosion remain the same regardless of the keeper orifice geometry is unrealistic. Further analysis and testing is required to address this issue, and a proposed method to address this topic is discussed in the next section.

B.4 Concluding Observations

In this study, direct measurements of cathode keeper orifice wear have been made using surface layer activation. The orifice erosion rates measured for the TH 8 operating condition were found to be comparable to those previously measured on the downstream surface, indicating that the radial wear is at least as significant.

The wear was clearly non-uniform over the polished surface, with heavier sputtering inferred from greater texturing of the polished surface downstream of the cathode. This would certainly have caused significant chamfering of the orifice, as seen in previous life tests.

The wear rates measured in this study were insufficient to have caused the rapid erosion observed during the ELT. It is of interest to investigate the effects of large geometry changes on keeper erosion.

This page has been intentionally left blank.

References

Anderson, J. R., Goodfellow, K. D., Polk, J. E., Rawlin, V. K., and Sovey, J. S., "Long Duration Ground Testing of the Deep Space 1 Flight Spare Ion Thruster – The First 15600 Hours," International Electric Propulsion Conference Paper #IEPC-01-076, Oct. 2001.

Anderson, J. R., Katz, I., and Goebel, D., "Numerical Simulation of Two-Grid Ion Optics Using a 3-D code," AIAA Paper #2004-3782, Jul. 2004.

Anderson, J. R., Vaughan, D., and Fitzgerald, D., "Experimental and Theoretical Analysis for Designing a Grid Clearing System for the NEXT Ion Propulsion System," AIAA Paper #2005-3866, Jul. 2005.

Anderson, H. H. and Bay, H. L., in *Sputtering by Particle Bombardment I: Physical Sputtering of Single Element Solids*, edited by R. Behrisch, Springer-Verlag, Berlin, p. 145-218 (1981).

Arwakawa, Y. and Nakano, M., "An Efficient Three-Dimensional Optics Code for Ion Thruster Research," AIAA Paper #1996-3198, Jul. 1996.

Aston, G. and Brophy, J. R., "Ion Accelerator System Mounting Design and Operating Characteristics for a 5 kW 30 cm Xenon Ion Thruster," AIAA Paper #87-1075, May 1987.

Bassner, H., Berg, H.-P., Kukies, R., and Müller, H., "Flight Test and Ground Investigation Results of the RITA Experiment on EURECA," AIAA Paper #94-2848, Jun. 1994.

Beatty, J. S., Snyder, J. S., and Shih, W., "Manufacturing of 57 cm Carbon-Carbon Composite Ion Optics for a 20 kW Class Ion Engine," AIAA Paper #2005-4411, Jul. 2005.

Behrisch, R., in *Sputtering by Particle Bombardment I: Physical Sputtering of Single-Element Solids*, edited by R. Behrisch, Springer-Verlag, Berlin, 1981, p. 1.

Bhattacharjee, S., Zhang, J., Shutthanadan, V., Shivaparan N. R., and Smith, R. J., *Nucl. Instr. and Meth. in Phys. Res. B*, **129** (1), 123-129 (1997).

Biersack, J. P., *Nucl. Instr. and Meth. in Phys. Res. B*, **27**, 21-36 (1987).

Blandino, J. J., Goodwin, D. G., and Garner, C. E., Diamond and Related Materials, **9** (12), 1992-2001 (2000).

Blandino, J. J., "Application of Diamond Films to Electric Propulsion: Low Energy Sputter Yield Measurement and MPD Plasma Assisted Chemical Vapor Deposition," California Institute of Technology, Ph.D. Thesis, Pasadena, CA, Apr. 2001.

Brophy, J. R., Polk, J. E., and Pless, L. C., "Test-to-Failure of a Two Grid, 30 cm dia. Ion Accelerator System," International Electric Propulsion Conference Paper #IEPC-93-172, 1993.

Brophy, J. R., Polk, J. E., and Rawlin, V. K., "Ion Engine Service Life Validation by Analysis and Testing," AIAA Paper #1996-2715, 1996.

Brophy, J. R., Katz, I., Polk, J. E., and Anderson, J. R., "Numerical Simulations of Ion Thruster Accelerator Grid Erosion," AIAA Paper #2002-4261, Jul. 2003.

Brophy, J. R., Ganapathi, G. B., Garner, C. E., Gates, J., Lo, J., Marcucci, M. G., and Nakazono, B., "Status of the Dawn Ion Propulsion System," AIAA Paper #2004-3433, Jul. 2004.

Chen, F. F., in *Plasma Diagnostic Techniques*, edited by R. H. Huddlestone and S. L. Leonard, Academic Press, New York, p. 113-200 (1965).

Cheney, K. B. and Pitkin, E. T., *J. Appl. Phys.*, **36** (11), 3542-3544 (1965).

Child, C. D., *Phys. Rev.*, **32**, 492-511 (1911).

Cumpson, P. J. and Seah, M. P., *Meas. Sci. Technol.*, **1**, 544-555 (1990).

Cullity, B. D., *Elements of X-ray Diffraction*, Addison-Wesley, Reading, 1959.

Cybulski, R. J., Shellhammer, D. M., Lovell, R. R., Domino, E. J., Kotnik, J. T., "Results from SERT I Ion Rocket Flight Test," NASA TN D-2718, March 1965.

Deltschew, R., Tartz, M., Plicht, V., Hartmann, E., Neumann, H., Leiter, H. J., and Esch, J., "Sputter Characteristics of Carbon-Carbon Compound Material," International Electric Propulsion Conference Paper #IEPC-01-118, Oct. 2001.

Ditrói, F. and Mahunka, I., *Nucl. Instr. Methods B*, **113**, 415-419 (1996).

Doerner, R. P., Whyte, D. G., and Goebel, D. M., *J. Appl. Phys.*, **93** (9), 5816-5823 (2003).

Doerner, R. P., Tynan, G. R., Oyerzabal, E., Taylor, K., Goebel, D. M., and Katz, I., "Plasma Surface Interaction Studies for Next-Generation Ion Thrusters," AIAA Paper #2004-4104, Jul. 2004.

Domonkos, M. T., "Evaluation of Low-Current Orificed Hollow Cathodes," University of Michigan, Ph.D. Thesis, Ann Arbor, MI, 1999.

Domonkos, M. T., Foster, J. E., and Patterson, M. J., "Investigation of Keeper Erosion in the NSTAR Ion Thruster," International Electric Propulsion Conference Paper #01-308, Oct. 2001.

Duchemin, O. B., and Polk, J. E., "Low Energy Sputtering Experiments for Ion Thruster Life Assessment: Preliminary Results," AIAA Paper #99-2858, Jun. 1999.

Duchemin, O. B., "An Investigation of Ion Engine Erosion by Low Energy Sputtering," California Institute of Technology, Ph.D. Thesis, Pasadena, CA, Feb. 2001.

Dushmann, S., *Rev. Mod. Phys.*, **2** (1), 382 (1930).

Eckstein, W., *Computer Simulations of Ion-Solid Interactions.*, Springer-Verlag, Berlin, 1991.

EerNisse, E. P., *J. Vac. Sci. and Technol.*, **12** (1), 564-568 (1975).

Foster, J. E., Haag, T., Kamhawi, H., Patterson, M., Malone, S., Elliot, F., Williams, G. J., Sovey, J. S., Carpenter, C., "The High Power Electric Propulsion (HiPep) Ion Thruster," AIAA Paper #2004-3812, Jul. 2004.

Frisbee, R. H., VanLandigham, E. E., and Brophy, J. R., "Status of NASA's Advanced Propulsion Technology Program," AIAA Paper #1996-2784.

Garner, C. E. and Brophy, J. R., "Fabrication and Testing of Carbon-Carbon Grids for Ion Optics," AIAA Paper #92-3149, Jul. 1992.

Gassiot, J. P., *Philos. Trans. Roy. Soc. (London)* **48**, 1 (1858).

Goebel, D. M., Martinez-Lavin, M., Bond, T. A., King, A. M., "Performance of XIPS Electric Propulsion in On-orbit Station Keeping of the Boeing 702 Spacecraft," AIAA Paper #2002-4348, Jul. 2002.

Goebel, D. M., Jameson, K. K., Watkins, R. M., Katz, I., and Mikellides, I., *J. Appl. Phys.* **98** (11), 113302 (2005).

Gold, H. and Rulis, R. J., Maruna, F. A., and Hawersaat, W. H., "Description and Operation of Spacecraft in SERT I Ion Thruster Flight Test," NASA TM X-52050, 1964.

Goodfellow, K. D., Ganapathi, G. B., and Stocky, J. F., "An Experimental and Theoretical Analysis of the Grid Clearing Capability of the NSTAR Ion Propulsion System," AIAA Paper #99-2858, Jun. 1999.

Grove, W. R., *Phios. Trans. Roy. Soc. (London)*, **142**, 86 (1853).

Grove, W. R., *Philos. Mag.* **5**, 203 (1853)

Hanna, J., Doerner, R. P., Tynan, G. R., Yu, J. H., Oyarzabal, E., and Taylor, K. J., "Carbon Film Deposition and Flaking Studies in Ion Thruster Environments," AIAA Paper #2005-3524, Jul. 2005.

Hayakawa, Y., Kitamura, S., Miyazaki, K., Yoshida, H., Akai, K., Yamamoto, Y., and Maeda, T., "5000-Hour Endurance Test of a 35-cm Xenon Ion Thruster," AIAA Paper #2001-3492, Jul. 2001.

Hayakawa, Y., Kitamura, S., and Miyazaki, K., "Endurance Test of C/C Grids for 14 cm Xenon Ion Thrusters," AIAA Paper #2002-3958, Jul. 2002.

Hayakawa, Y., Kitamura, S., Miyazaki, K., Yoshida, H., Akai, K., and Kajiwara, K., "Wear Test of a Hollow Cathode for 35 cm Xenon Ion Thrusters," AIAA Paper #2002-4100, Jul. 2002.

Hayakawa, Y., Yoshida, H., Kitamura, S., Kajiwara, K., and Okawa, Y., "Status of the 150-mN Ion Engine Research at JAXA," AIAA Paper #2004-3969, Jul. 2004.

Hecht, E. and Bohdansky, J., *J. Nucl. Mater.*, **122-123**, 1431 (1984).

Hedges, D. E. and Meserole, J. S., *J. Propulsion and Power*, **10** (2), 255-261 (1994).

Hsiao, R., *IBM J. Res. Dev.*, **43** (1), 89-102 (1999).

Inspektor, A., Carmi, U., Raveh, A., Khait, Y., and Avni, R., *J. Vac. Sci. Technol. A*, **4** (3), 375-378 (1986).

IAEA TECHDOC-924, "Thin Layer Activation Method and its Application in Industry," International Atomic Energy Agency Report, Vienna, Austria, Jan. 1997.

Jahn, R. G., *Physics of Electric Propulsion*, McGraw-Hill, New York, 1968.

Jameson, K. K., Goebel, D., and Watkins, R., "Hollow Cathode and Keeper Region Plasma Measurements," AIAA Paper #2005-3667, Jul. 2005.

Kaufman, H. R., "An Ion Rocket with an Electron Bombardment Ion Source," NASA TN D-585, 1959.

Kaufman, H. R., and Reader, P. D., in *Electrostatic Propulsion*, edited by D. B. Langmuir, E. Stuhlinger, and J. M. Sellen, Jr., Academic Press, New York, p. 3-20, 1961.

Kerslake, W. R. and Ignaczak, L. R., *J. of Propulsion and Power*, **30** (3), 258-290 (1993).

Killinger, R., Bassner, H., Müller, J., and Kukies, R., "RITA Ion Propulsion for ARTEMIS Lifetime Test Results," AIAA Paper #2000-3273, Jul. 2000.

Killinger, R., Bassner, H., Leiter, H., and Kukies, R., "RITA Ion Propulsion for ARTEMIS – Results Close to the Completion of the Life Test," AIAA Paper #2001-3490, Jul. 2001.

Killinger, R., Kukies, R., Surauer, M., Saccoccia, G., "Final Report on the ARTEMIS Salvage Mission Using Electric Propulsion," AIAA Paper #2003-4546, Jul. 2003.

Kingdon, K. H., and Langmuir, I., *Phys. Rev.*, **22**, 148 (1923).

Kolasinski, R. D., *J. of Propulsion and Power*, **20** (6), 992-999 (2004).

Kosako, T. and Nishimura, K., *Nucl. Instrum. Methods B*, **56-7**, 900-903 (1991).

Kuninaka, H., Satori, S., and Horiuchi, Y., "Continuous Operation Test of Microwave Discharge Ion Thruster System," AIAA Paper #95-3070, Jul. 1995.

Kustner, M., Eckstein, W., Dose, V., Roth, J., *Nucl. Instrum. Methods B*, **145**, 320-331 (1998).

Langmuir, I., *Phys. Rev.*, **2**, 450-486 (1913).

Laegreid, N. and Wehner, G. K., *J. Appl. Phys*., **32** (3), 365-369 (1961).

Lee, R., *J. Vac. Sci. Technol.*, **16** (2), 164-170 (1979).

Lindhard, J., Scharff, M., and Schiott, H. E., *Kgl. Danske Videnskab. Selskab, Mat.-Fys. Medd.* **33** (14), 1-42 (1963).

Lindhard, J., Nielsen, V., and Scharff, M., *Kgl. Danske Videnskab. Selskab, Mat.-Fys. Medd.* **36** (10), 1-32 (1968).

Lokas, E. L., *Mon. Not. R. Astron. Soc.* **296**, 491-501 (1998).

Longuet-Higgins, M. S., *J. Fluid Mech.*, 459 (1963).

Lu, CS, and Lewis, O., *J. Appl. Phys.*, **43** (11), 4385-4390 (1972).

Maloy, J. E., Poeschel, R. L., and Dulgeroff, C. R., "Characteristics of 30 cm Mercury Ion Thrusters," AIAA Paper #1981-715, Apr. 1981.

Marker, C. L, Clemons, L. A., Banks, B. A., Miller, S., Snyder, A., Hung, C., Karniotis, C. A., and Waters, D. L., "Transport of Sputtered Carbon during Ground-Based Life Testing of Ion Thrusters," AIAA Paper #2005-4413, Jul. 2005.

Marks, L. M. and Clark, K. E., vonJaskowsky, W., and Jahn, R. G., "MPD Thruster Erosion Measurement," AIAA Paper #1982-1884.

Matsunami, N., Yamamura, Y., Itikawa, Y., Itoh, N., Kazumata, Y., Miyagawa, S., Morita, K., Shimizu, R., and Tawara, H., *Atomic Data and Nuclear Data Tables*, **31**, 1-80 (1984).

Mikellides, I., Katz, I., Goebel, D., and Polk, J., "Theoretical Modeling of a Hollow Cathode Plasma for the Assessment of Insert and Keeper Lifetimes," AIAA Paper #2005-4234, Jul. 2005.

Molchanov, V. A. and Tel'kovskii, V. G., *Soviet Physics-Doklady*, **6** (2), (1961).

Mueller, J., Brophy, J. R., Brown D. K., and Garner, C. E., "Performance Characterization of 15 cm Carbon-Carbon Composite Grids," AIAA Paper #94-3118, Jun. 1994.

Mueller, J., Brophy, J. R., and Bown, D. K., "Endurance Testing and Fabrication of Advanced 15 cm and 30 cm Carbon-Carbon Composite Grids," AIAA Paper #95-2660, Jul. 1995.

Oechsner, H., *Z. Physik*, **261**, 37-58 (1973).

Oura, K., Lifshits, V. G., Saranin, A. A., Zotov, A. V., Katayama, M., *Surface Science: An Introduction*, Springer-Verlag, Berlin, 2003.

Patterson, M. J., Rawlin, V. K., Sovey, J. S., Kussmaul, M. J., and Parkes, J., "2.3 kW Ion Thruster Wear Test," AIAA Paper #1995-2516, Jul. 1995.

Patterson, M. J., Foster, J. E., Haag, T. W., Rawlin, V. K., Soulas, G. C., "NEXT: NASA's Evolutionary Xenon Thruster," AIAA Paper #2002-3832, Jul. 2002.

Pierson, H. O., *Handbook of Carbon, Graphite, Diamond, and Fullerenes*, Noyes Publications, Park Ridge, NJ (1993).

Polk, J. E., Patterson, M. J., Brophy, J. R., Rawlin, V. K., Sovey, J. S., Myers, R. M., Blandino, J. J., Goodfellow, K. D., and Garner, C. E., "A 1000 Hour Wear Test of the NASA NSTAR Ion Thruster," AIAA Paper #1996-2784, Jul. 1996.

Polk, J. E., "Mechanisms of Cathode Erosion in Plasma Thrusters," Princeton University, Ph.D. Thesis, Princeton, NJ, Nov. 1997.

Polk, J. E., Anderson, J. R., Brophy, J. R., Rawlin, V. K., Patterson, M. J., Sovey, J., and Hamley, J., "An Overview of the Results from an 8200 hour Wear Test of the NSTAR Ion Thruster," AIAA Paper #1999-2446, Jun. 1999.

Polk, J. E., Kakuda, R. Y., Anderson, J. R., Brophy, J. R., Rawlin, V. K., Patterson, M. J., Sovey, J., and Hamley, J., "Performance of the NSTAR Ion Propulsion System on the Deep Space One Mission," AIAA Paper #2001-16765, January 2001.

Polk, J. E., Goebel, D., Brophy, J. R., Beatty J., Monheiser, J., Giles, D., Hobson, D., Wilson, F., Christensen, J., De Pano, M., Hart, S., Ohlinger, W., Hill, D. N., Williams, J., Wilbur, P., Laufer, D. M., and Farnell, C., "An Overview of the Nuclear Electric Xenon Ion System (NEXIS) Program," AIAA Paper #2003-4713, July 2003.

Polk, J. E., Marrese, C., Thornber, B., Dang, L., Johnson, L., "Temperature Distributions in Hollow Cathode Emitters," AIAA Paper #2004-4116, Jul. 2004.

Pullins, S., Chiu, YH, Levandier, D. J., and Dressler, R. A., "Ion Dynamics in Hall Effect and Ion Thrusters: Xe^+ + Xe Symmetric Charge Transfer," AIAA Paper #2000-0603, Jan. 2000.

Rapp, D. and Francis, W. E., *J. Chem. Phys.* **37**, 2631 (1962).

Randolph, T. M. and Polk, J. E., "An Overview of the Nuclear Electric Xenon Ion System (NEXIS) Activity," AIAA Paper #2004-3450, Jul. 2004.

Rawlin, V. K. and Pawlik, E. V., *J. Spacecraft*, **5** (7), 814-820 (1968).

Robinson, M. T. and Torrens, I. M., *Phys. Rev. B*, **9** (12), 5008-5024 (1974).

Robinson, M. T., in *Sputtering by Particle Bombardment I: Physical Sputtering of Single Element Solids*, edited by R. Behrisch, Springer-Verlag, Berlin, p. 79-144 (1981).

Rol, P. K., Fluit, J. M., and Kistemaker, J., *Physica*, **26**, 1000-1008 (1960).

Rosenberg, D. and Wehner, G. K., *J. Appl. Phys.*, **33** (7), 1842-1845 (1962).

Roosendaal, H. E., in *Sputtering by Particle Bombardment I: Physical Sputtering of Single Element Solids*, edited by R. Behrisch, Springer-Verlag, Berlin, p. 219-256 (1981).

Roth, J., in *Sputtering by Particle Bombardment II: Sputtering of Alloys and Compounds, Electron and Neutron Sputtering, Surface Topography*, edited by R. Behrisch, Springer-Verlag, Berlin, p. 91-141.

Sakabe, S. and Izawa, Y., *Atomic Data and Nuclear Data Tables* **49**, 257 (1991).

Sanders, J. B., *Canadian Journal of Physics*, **46**, 455-465 (1968).

Sarver-Verhey, T. R. and Hamley, J. A., "Discharge Ignition Behavior of the Space Station Plasma Contactor," AIAA Paper #1994-3311, Jun. 1994.

Schilling, W. and Ullmaier, H. "Physics of Radiation Damage in Metals," *Materials Science and Technology: A Comprehensive Treatment*, Vol. 10 B, VCH Publishers, Inc., New York, 1994, p. 179-241.

Schonfeld, E., Kibbey, A. H., and W. Davis, Jr., *Nucl. Instr. Methods*, **45**, 1-21 (1966).

Seah, M. P., *Nucl. Instr. and Meth. in Phys. Res. B*, **229**, 348-358 (2005).

Sengupta, A., Brophy, J. R., and Goodfellow, K. D., "Status of the Extended Life Test of the Deep Space 1 Flight Spare Ion Engine after 30,352 Hours of Operation," AIAA Paper #2003-4558, Jul. 2003.

Sigmund, P., *Phys. Rev.*, **184** (2), 1969.

Smentkowski, V. S., *Progress in Surface Science*, **64**, 1-58 (2000).

Smith, J. N., Meyer Jr., C. H., and Layton, J. K., *Nucl. Technol.*, **29**, 318 (1976).

Snyder, J. S., Brophy, J. R., Goebel, D. M., and Beatty, J. S., "Development and Testing of Carbon-Based Ion Optics for 30 cm Ion Thrusters," AIAA Paper #2003-4716, Jul. 2003.

Stepanova, M., Drew, S. K., and Soshnikov, I. P., *Phys. Rev. B*, **66** (2002).

Stuart, R. V. and Wehner, G. K., *J. Appl. Phys.*, **33** (7), 2345-2352 (1962).

Tartz, M., Neumann, H., Fritsche, B., Leiter, H., J., and Esch, J., "Investigation of Sputter Behavior of Ion Thruster Grid Materials," AIAA Paper #2004-4114, 40th Joint Propulsion Conference, Huntsville, AL, July 11-14, 2004.

Tartz, M., Manova, D., Neumann, H., Leiter, H., Esch J., "Sputter Investigation of Ion Thruster Grid Materials," AIAA Paper #2005-4414, Jul. 2005.

"Thin Layer Activation Method and its Application in Industry," International Atomic Energy Agency, IAEA TECDOC-924, Vienna, Austria, Jan. 1997.

Tuinstra, F. and Koenig, J. L., "Raman Spectrum of Grapite," *The Journal of Chemical Physics*, **53** (3), 1126-1130 (1970).

Unik, J. P. and Rasmussen, J. O., *Phys. Rev.*, **115** (6), 1687-1692 (1959).

Veeco website, www.veeco.com (2006).

Wallace, G. "Calculation of Depth Profile for Thin Layer Activation," International Atomic Energy Agency, Client Report 62891H 11, Vienna, Austria, Mar. 1999.

Wehner, G., *J. Appl. Phys.*, **30** (11), 1762-1765 (1959).

Wehner, G. K., General Mills Report No. 2309, 1962 (unpublished).

Weijsenfeld, C. H., Hoogendoorn, A., and Koedam, M., *Physica*, **27**, 763-764 (1961).

Williams, J. D., Johnson, M. L., and Williams, D. D., "Differential Sputtering Behavior of Pyrolytic Graphite and Carbon-Carbon Composite under Xenon Bombardment," AIAA Paper #2004-3788, Jul. 2004.

Winterbon, K. B., Sigmund, P., and Sanders, J. B., *Matematisk-Fysiske Meddelelser Udgivet Af Det Kongelige Danske Videnskabernes Selskab*, **37** (14), 1-73 (1970).

Winters, H. F. and Horne, D., Phys. Rev. B, **10** (1), 55-63 (1974).

Wirz, R., Gale, M., Mueller, J., and Marrese, C., "Minature Ion Thrusters for Precision Formation Flying," AIAA Paper #2004-4115, Jul. 2004.

Yamamura, Y. and Tawara, H., "Energy Dependence of Ion-Induced Sputtering Yields from Monatomic Solids at Normal Incidence," *Atomic and Nuclear Data Tables*, **62** (2), 149-253 (1996).

Zhao, Y., Wang, G., Lu, T., Characterization of Amorphous and Crystalline Rough Surface: Principles and Applications, Academic Press, San Diego, 2001.

Ziegler, J. E., Biersack, J. P., and Littmark, U. *The Stopping and Range of Ions in Solids. Vol. 1*, Pergamon Press, 1985.